UNIVERSITY OF CALIFORNIA SAN DIEGO

Design of oscillatory movement for ground-based locomotion and synchronized movement in bioinspired robotics

A dissertation submitted in partial satisfaction of the
requirements for the degree
Doctor of Philosophy

in

Engineering Science (Mechanical Engineering)

by

Wei Zhou

Committee in charge:

Professor Nicholas G. Gravish, Chair
Professor Jorge Cortes
Professor Miroslav Krstic
Professor Jeremie Palacci
Professor David Saintillan

2022

The Dissertation of Wei Zhou is approved, and it is acceptable in quality and form for publication on microfilm and electronically.

University of California San Diego

2022

DEDICATION

To my parents, without whom I can't make it this far.

TABLE OF CONTENTS

LIST OF FIGURES

LIST OF TABLES

ACKNOWLEDGEMENTS

The journey of my academic pursuing is like wandering from the very tip of a remote trail to the shrine of knowledge, where I met with, talk to, and learnt from great minds. It resembles part of my life where I walked out of mountains, crossed over oceans, and saw the world of diversity at broader horizons. I attribute this to my supportive parents and family where is origin of all my stories. They have my back all the time. Their words are few but strong, paving a concrete stage which I can step on. Even if when I felt falling, I believed I would fall into their warm hug, where I could take a nap, recover and restart. With all their love I made it to this height of my life.

Five years at San Diego have become a memorable chapter of my life. I would like to thank my advisor, Prof. Nick Gravish, who not only provides all the guidance in academic research but also cares the well-being of group members. He grabs the big picture like a navigator holding his nautical chart. When I fight with thunderstorms of tons of experiments and equations, I can always see the light house he set up so I never get lost. During the hard time of pandemic, he managed to build a safe experimental environment for us. He set the equipment at home so I can control them remotely. Together with the experimental guardian, Sam, we eventually published our work on PRX. Through multiple paper drafts and many long nights, his guidance has proved to be invaluable. At the same time, I would like to thank all my committee members, your expertise and feedback perfected my thesis work.

Gravish lab members and alumni are the precious fortune rewarded to me during my stay. We work independently, we chat collaboratively, and we have fun together. Everyone shine their personality in everyday life, Glenna's meticulosity, Mingsong's dedication, Shivam's friendliness, James' curiosity, etc. These are just examples of their many shining parts within, which together decorate our lab a wonderful place to work in. I am also grateful being able to work with Zhuonan and Yudong. Their talent and creativity boosted our exploration in robot synchronization. People will leave and new students always come, but the tradition of harmonious atmosphere in the lab continues.

Lastly, thank you all my friends. For those trails we explored, those ice we skated, those snow we skied, those waves we surfed, I will memorize them all the time. You show up in my life at a point, keep me company for a while. When we separate, I will give a hug and say goodbye. But every meal we had, every boba tea we share, every song we sing, every game we played, joy and tears, they sediment in my brain, forming a gallery of friendship.

Thank you to all my funding sources and without them, it would have been impossible: The National Science Foundation and the Office of Naval Research. The following acknowledgments are to satisfy the requirements of the University of California San Diego.

Chapter 1, in part, is a reprint of the material as it appears in Hao, Z., Zhou, W. and Gravish, N., 2022. Proprioceptive feedback design for gait synchronization in collective undulatory robots. *Advanced Robotics*, pp.1-16. The dissertation author was the co-author of this paper.

Chapter 2, in full, is a reprint of the material as it appears in Zhou, W. and Gravish, N., 2020. Rapid two-anchor crawling from a milliscale prismatic-push–pull (3P) robot. *Bioinspiration & Biomimetics*, 15(6), p.065001. The dissertation author was the primary researcher and the first author of this paper.

Chapter 3, in full, is a reprint of the material as it appears in Zhou, W. and Gravish, N., 2020. Soft Microrobotic Transmissions Enable Rapid Ground-Based Locomotion. In *2020 IEEE/RSJ International Conference on Intelligent Robots and Systems (IROS)* (pp. 7874-7880). IEEE. The dissertation author was the primary researcher and the first author of this paper.

Chapter 4, in full, is a reprint of the material as it appears in Zhou, W., Peralta, J.D., Hao, Z. and Gravish, N., 2022. Lateral contact yields longitudinal cohesion in active undulatory systems. *Physical Review E*, 105(5), p.054604. The dissertation author was the primary researcher and the first author of this paper.

Chapter 5, in full, is a reprint of the material as it appears in Zhou, W., Hao, Z. and Gravish, N., 2021. Collective synchronization of undulatory movement through contact. *Physical Review X*, 11(3), p.031051. The dissertation author was the primary researcher and the first author of this paper.

VITA

2011–2015 B.S. in Mechanical Engineering and Automation, Beihang University, Beijing, China

2015–2017 M.S. in Engineering Science (Mechanical Engineering), University of Michigan, Ann Arbor

2017–2022 Ph.D. in Engineering Science (Mechanical Engineering), University of California San Diego

PUBLICATIONS

Zhou, W., Peralta, J.D., Hao, Z. and Gravish, N., 2022. Lateral contact yields longitudinal cohesion in active undulatory systems. *Physical Review E*, 105(5), p.054604.

Hao, Z., Zhou, W. and Gravish, N., 2022. Proprioceptive feedback design for gait synchronization in collective undulatory robots. *Advanced Robotics*, pp.1-16.

Zhou, W., Hao, Z. and Gravish, N., 2021. Collective synchronization of undulatory movement through contact. *Physical Review X*, 11(3), p.031051.

Zhou, W. and Gravish, N., 2020. Rapid two-anchor crawling from a milliscale prismatic-push–pull (3P) robot. *Bioinspiration & Biomimetics*, 15(6), p.065001.

Zhou, W. and Gravish, N., 2020. Soft Microrobotic Transmissions Enable Rapid Ground-Based Locomotion. In *2020 IEEE/RSJ International Conference on Intelligent Robots and Systems (IROS)* (pp. 7874-7880). IEEE.

ABSTRACT OF THE DISSERTATION

Design of oscillatory movement for ground-based locomotion and synchronized movement in bioinspired robotics

by

Wei Zhou

Doctor of Philosophy in Engineering Science (Mechanical Engineering)

University of California San Diego, 2022

Professor Nicholas G. Gravish, Chair

Animals in nature move through the rhythmic oscillation of their appendages and bodies. Similar oscillatory motion is a hallmark of bioinspired robots, which seek to embed biological principles into the design, sensing, and control of robots. While there is a robust theory of nonlinear oscillatory systems, there still exist fundamental gaps in knowledge when considering robotic locomotion. For example, ground-based robots make intermittent contact with the ground to propel themselves forward or to turn, and such "making and breaking" of contact between the oscillatory actuation source and the environment can lead to novel locomotion challenges. Additionally, when multiple robots are moving together the coordination of rhythmic gaits (such

as through synchronization) may lead to beneficial group movement. However, the methods to design such synchronized locomotion are not altogether straightforward especially when considering potential communication limitations between robots. This dissertation addresses specific problems in oscillatory locomotion of bioinspired robots. In the first study the author developed a inch-worm inspired robot that can push and pull against the ground with simple "feet" to propel itself. The author studied how basic feedforward oscillatory actuation of the "feet" leads to non-trivial locomotion dynamics through foot slipping and stochastic foot-ground contact mechanics. In follow up work the author demonstrated enhanced capabilities of this robot such as turning, that was achieved through incorporation of soft materials in the design process. In the third study the author studied the collective behavior of simple three-link "swimming" robots that are controlled through feedforward oscillatory actuation. Oscillatory phase differences between neighboring robots lead to intermittent collisions that drive the group into a stable spatial configuration by lateral and longitudinal movement. We derive conditions for group spacing and density based on phase variation, examine the effective interaction potential between neighboring robots, and identify a compatibility condition for robots to safely swim in close proximity without collisions. In the last study the author enables the oscillatory motion of robot's in a collective to be generated through nonlinear, limit-cycle dynamics. The author finds that intermittent contact between robots leads to overall group synchronization of oscillatory swimming gaits which reduces contact forces between robots and enables high density configurations. A phase oscillator model of this process is developed and the author derives the theoretical conditions for group synchronization, observing good agreement between experiments and the theoretical model. This work enables the author to demonstrate in experiment the swimming synchronization of four three-link robots that do not communicate with each other, but instead leverage the nonlinear dynamics of the nonlinear oscillator control system. Ultimately, the work the author presents in this thesis leads to new understanding of how oscillatory motion is influenced by intermittent, nonlinear, interactions with the environment and between robots.

Chapter 1

Introduction

1.1 Motivation

Bioinspired robotics is an important area in robotics research [1] which seeks to incorporate principles of biology into robot design. The most common examples of bioinspired robots are ones which emulate the shape, morphology, and form of animals such as bat, bird, dog, and snake like robots. However, bioinspiration can be incorporated at many different levels beyond just superficial features. For example, bioinspired sensing has enabled new advances in robot vision [2], tactile sensing [3], and actuation [4]. A fundamental function of many living systems is movement, either through locomotion through the world of movement in place. In all but the smallest of organisms locomotion and movement in nature occurs through the generation of oscillatory movement (often called rhythmic movement). In this thesis I present a series of studies to examine elements of bioinspired locomotion through the generation, study, and design of oscillatory dynamics.

1.2 Biological origins of rhythmic motion in individuals and collective motion in groups

Movement in biology and robotics arises from coordinated oscillation and undulation of their appendages and bodies. The rhythmic motion is a common natural phenomena at all scales. It can be described as a motion of whole or part of the body moving in a cyclic

and repetitive pattern. The universally observed locomotion strategies to move are most cited examples, such as walking and running on legs, lateral undulations of the body while slithering and swimming, longitudinal body oscillations during crawling, flapping wings during flying, and beating cilia and flagella of unicellular or multicellular organism. The rhythmic motions in biology can be broadly categorized as being generated through one of two methods: 1) central pattern generators (CPG) which provide common rhythmic signals across appendages and provide direct coordination of motion phasing, and 2) local "reflexive" oscillators that are not coupled through the neural system but can be coupled through body and environmental mechanics. Both modalities incorporate environmental and proprioceptive feedback however the timescales over which external perturbations impact rhythmic signal generation in CPGs and "reflexive" oscillators may be very different. Many abstractions of these circuits exist [5, 6, 7], and one common model is the phase oscillator, which oscillates at a constant frequency ω and can be augmented with sensory feedback.

In locomotion studies across aquatic and terrestrial locomotion there have been observations of the important role CPGs play. Early classic experiments determined spinal cord can generate intrinsic rhythmic movements [8]. The advance in evidences revealed that the basic motor patterns underlying rhythmic limb movements during locomotion are generated by neuronal networks located within the spinal cord [9].

In smaller scale organisms such as the worm *C. elegans*, it has been shown that a combination of CPG and local "reflex" oscillations drive swimming motion. Biomechanical and neural experiments have demonstrated that the generation of undulatory body motion in *C. elegans* is largely through local proprioceptive reflex responses along the body that sense the local body bending and generate a bending actuation in response [10, 11]. Thus, the body bending wave propagation occurs as a "reflex chain" in which the wave propagation doesn't involve communication between oscillators and instead responds only to the bending state of the local body region. Experiments have demonstrated this local oscillator principle by isolating body regions and showing that a propagating wave is halted at a body region where bending is

inhibited [10].

Coordinated motion happens not only in individual organisms but also in groups. Collective motion of groups is a commonly observed phenomena in nature at a wide variety of scales. Researchers have studied the collective behaviors in bacterial colonies [12, 13], cells [14, 15], insects [16, 17, 18], fish schools [19, 20], bird flocks [21, 22, 23], and human crowds [24, 25]. These systems always consist of many similar units that move through self-propulsion and interact with neighbors through mechanical forces often mediated through hydrodynamic or contact forces [12]. In groups of larger animals such as birds and fish the collective movements are generated through visual sensory cues [22, 23] and hydrodynamic interactions between the individuals [26, 27, 28, 29]. However, smaller scale systems such as swimming bacteria, sperm, and worms, that often swim in higher group densities may experience repulsive contact forces in addition to fluid interactions [30, 31, 32]. The long-range communication and short-range interaction resemble two categories of control philosophy in robotics. Centralized approaches to the planning and control of collective motion require long-range communication and perception capabilities among robots, so that a central planning system can plan the motion of the group. Alternatively, decentralized control approaches rely on motion planning algorithms that run independently on each robot based on local information exchange between robots.

In collective motion, an individual unit's action is dominated by the influence of the others, and the system can transit from disorder to order under certain conditions. The synchronization phenomena in large groups of interacting units are attractive research areas in physical, biological, and social systems. Individual units of many of these biological systems can achieve synchronized motion with their neighbors through physical interactions, which are often through a fluid. Recent studies have demonstrated that fluid force acting between pairs of flagella [33, 34, 35], arrays of cilia [36, 37, 38], and even flapping wings [26, 27, 39] can lead to phase and frequency synchronization of oscillatory body movements. Meanwhile, other studies demonstrated that short-range steric inter-filament interactions and filament roughness are sufficient – even in the absence of inter-filament hydrodynamic interactions – to generate a rich variety of collective

spatiotemporal oscillatory, traveling and static patterns [40]. However, many animal and robot groups operate in close proximity where movements may result in collisions, resulting in collective jamming [40, 41, 42]. We hypothesize that mobile robot groups may benefit from synchronized motion (gaits) and thus it is and important to understand the fundamental principles of the formation of synchronization in groups.

1.3 Nonlinear oscillators and synchronization

Rhythmic motions are ubiquitous in living organisms. The mathematical framework for designing and analyzing oscillatory behavior of dynamical systems, such as that of a locomoting animal, is well established in the field of nonlinear dynamics. In particular examples such as the generation of oscillatory outputs from CPGs [6], the synchronization of coordinated body movement, and the adaptation of body move to accommodate new environments (from swimming to walking for instance [43]) relies on the study of nonlinear oscillators. An oscillator is an autonomous dynamical system which exhibits a stable limit cycle attractor [44, 45]. A stable limit cycle is a closed trajectory in the phase-space of the dynamical system in which a surrounding region of initial conditions is attracted onto the limit cycle. The closed trajectory of the limit cycle implies that the system's state variables will be periodic, i.e. the system in steady state will oscillate.

Nonlinear oscillators have been extensively used in the robotics field for generating stable periodic motion trajectories of joints and bodies [44, 46, 47, 48, 49]. Limit cycles are advantageous because: (a) the systems can produce the periodic oscillations spontaneously without time dependent forcing, (b) the oscillation amplitude is robust and resistant against transient perturbation with asymptotic return to the limit cycle, and (c) the oscillation phase is marginally stable enabling phase perturbations to persist. It is this last point which allows for phase synchronization between oscillators. Limit cycle control of walking, swimming, and hopping robots have demonstrated the robustness of these control methods in addition to novel

adaptive behaviors which can adjust to changing loads, environmental forces, and behaviors [50, 51, 52, 53].

In seminal work from Buchli, Righetti, and Ijspeert, these authors introduced a principled approach to designing dynamical systems that generate limit cycle behavior for robot control [44]. The core of this method is to work from a phase-radius coordinate system (PRCS) approach for designing limit cycle behavior. For a second-order dynamical system the phase-radius coordinate system effectively converts from the phase-space (which are the equivalent Cartesian coordinates of the phase space) to a polar coordinate form. Thus, with the appropriate rescaling of phase along the limit cycle (see [44] for details) a PRCS limit cycle can be written as

$$\dot{\phi} = \omega \tag{1.1}$$

$$\dot{\mathbf{r}} = \mathbf{F}(\mathbf{r}) \tag{1.2}$$

where ϕ is the evolution of phase along the limit cycle trajectory and $\mathbf{r}$ is the radial distance from the origin to the instantaneous system state (which can be high-dimensional). The phase of an oscillator has a strict definition that it must be a quantity that increases at constant rate. The PRCS concept is advantageous because the desired limit cycle behavior of the system is the starting point for feedback design, and the PRCS system can eventually be recast into the desired phase-space coordinates as necessary. Similarly, other dynamical systems can be converted into PRCS for analysis of limit-cycle behavior.

When multiple limit cycle oscillators are coupled, the neutral stability of the phase variable can lead to synchronization phenomena [54]. Phase synchronization occurs when oscillators with a common frequency align their phases in often an in-phase, or anti-phase, arrangement. If oscillators have different natural frequencies, in some instances coupling can drive the group to a common oscillatory frequency. The canonical model for such synchronizing systems is the Kuramoto model of synchronization [55] where the phase variables of oscillators are directly coupled. In the appropriate regimes of coupling strength and connectivity this system

will display a wide range of phase and frequency synchronization behavior. The Kuramoto system has been extensively studied and there are many reviews of the system phenomenology [45, 56].

1.4 Generating rhythmic motion in robotics

A motor actuated joint system is a basic component in robotics. We summarize in this section different methods to generate periodic motions in motor joints (see Fig. 1.1). There are different types of motors. A servo motor usually takes a reference angle θ_r as an input and actuates the motor to the reference angle using its internal PID control loop. A DC motor is a open-loop system which takes current I as an input and generates motor torque $\tau = KI$, where K is the motor constant.

In our applications, we utilized different methods to actuate periodic motions in robotic joints. The simplest way is setting a time-dependent sinusoidal reference signals:

$$\theta_r = A\sin(\omega t + \phi_0) \tag{1.3}$$

This joint system has a constant linearly increasing phase variable $\phi(t) = \omega t + \phi_0$ that can't not be shifted even after perturbation.

Another method is using intrinsic nonlinear oscillator to generate autonomous periodic oscillation. One of the simplest examples of a PRCS limit cycle system is the Hopf oscillator which is described by the equations

$$\dot{\phi} = \omega \tag{1.4}$$

$$\dot{r} = \beta r(1 - r^2) \tag{1.5}$$

with state variables ϕ and r. This system exhibits a circular limit cycle in phase space with radius $r = 1$, and frequency ω. Perturbations to the phase of this system will persist, which

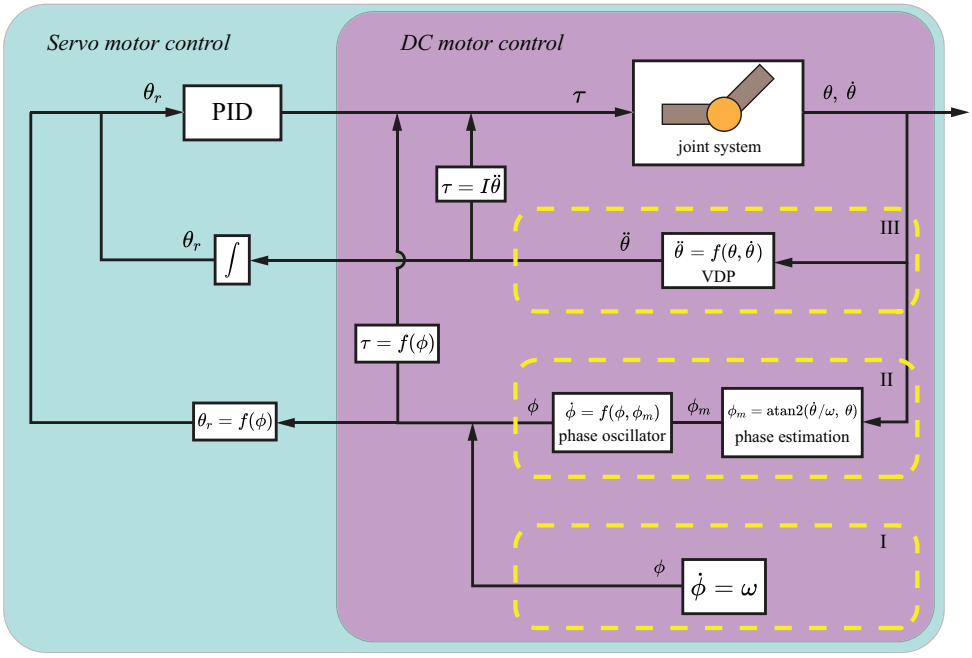

Figure 1.1. Different actuation methods of robot joints. I. Time-dependent sinusoidal oscillation. II. Intrinsic nonlinear oscillator with proprioceptive feedback. III. Direct nonlinear oscillator.

gives the ability to adjust its phase during interaction with other robot joints or environment. Proprioceptive feedback can be augmented to the phase dynamics to enhance the phase adaptive ability.

$$\dot{\phi} = \omega + \gamma\, g(\phi_m, \phi) \tag{1.6}$$

where $g(\phi_m, \phi)$ is the proprioceptive feedback function. Critically, the proprioception feedback function only takes into account each oscillator's individual intrinsic controller phase ϕ and the instantaneous measured phase through proprioception ϕ_m. The measured phase can be computed through a function of the state variables, a common example of this is $\phi_m = \text{atan2}(\dot{\theta}, \theta)$ where atan2 is the arctangent evaluated over the four quadrants of the phase plane. In this method, we

still need to map the phase of the oscillator back to the desired states of the robot joints.

$$\theta = r\ \cos(\phi) \tag{1.7}$$

$$\dot{\theta} = r\ \sin(\phi) \tag{1.8}$$

Critically, oscillatory motion that is generated through evolution of an explicit oscillator equation ($\dot{\phi} = f(\phi, \mathbf{x}, \mathbf{p})$ where $\mathbf{x}$ and $\mathbf{p}$ are state vectors and parameters respectively) requires a mapping to and from the mechanical phase space of the robot to the oscillator dynamics and back.

An alternative approach to generating oscillatory dynamics is to explicitly evaluate a non-linear oscillator equation directly using the state variables of the mechanical system (for example position and velocity of a robot joint). In these oscillators the second order dynamics of the joint, when actuated with appropriate torque, can generate rhythmic movement that doesn't require mapping to and from an explicit oscillator system. Many examples of limit cycle oscillators exist in dynamical systems and one of the most canonical examples is that of the Van der Pol oscillator

$$\ddot{x} + x + \varepsilon(x^2 - 1)\dot{x} = 0 \tag{1.9}$$

This is an example of a second-order nonlinear oscillator for which positive values of ε yield periodic steady-state behavior of the phase-space variables x and $\dot{x}$. In the last method, we take advantage of Van der Pol oscillator of being a second order system, which means we can directly plug in the states of the robot joints and acquire the torque needed for autonomous oscillation.

$$\ddot{\theta} = -\theta - \varepsilon(\theta^2 - 1)\dot{\theta} \tag{1.10}$$

$$\tau = I\ddot{\theta} \tag{1.11}$$

In this method, phase of the joint oscillation is directly the phase of the nonlinear oscillator. Perturbation to the states of the joints is immediately mirrored to the phase of the nonlinear

oscillator. The phase adaptive rate is significant faster than the method through proprioceptive feedback.

1.5 Outline of the dissertation

In chapter 2, the author present a milliscale push-pull robot which is capable of operating across a wide range of actuation frequencies thus enabling us to expand our understanding of two-anchor locomotion beyond the low-speed regime. A milliscale robot was designed and fabricated which uses anisotropic friction at two oscillating contact points to propel itself forward in a push-pull fashion. In experiments, the oscillation frequency, f, was varied over a wide range (10-250 Hz) and observe a non-linear relationship between robot speed over this full frequency range. The speed-frequency relationship at low actuation frequencies is consistent with previously described two-anchor models and experiments in biology and robotics, however the higher frequency behavior is inconsistent with two-anchor frictional behavior. Both deterministic two-anchor model and probabilistic foot slipping two-anchor model were built to understand the locomotion behavior of our system.

In chapter 3, the author present the design, fabrication, testing, and control of a 0.4 g milliscale robot employing a soft polymer flexure transmission for rapid ground movement. The robot was constructed through a combination of two methods: smart-composite-manufacturing (SCM) process to fabricate the actuators and robot chassis, and silicone elastomer molding and casting to fabricate a soft flexure transmission. The flexure transmission was actuated using two customized piezoelectric (PZT) actuators that attach to the transmission inputs. Through high-frequency oscillations, the actuators are capable of exciting vibrational resonance modes of the transmission which result in motion amplification on the transmission output. Directional spines on the transmission output generate traction force with the ground and drive the robot forward. By varying the excitation frequency of the soft transmission we can control locomotion speed, and when the transmission is oscillated at its resonance frequency we achieve high speeds

with a peak speed of 439 mm/s (22 body lengths/s). By exciting traveling waves through the soft transmission, we were able to control the steering direction. Overall this chapter demonstrates the feasibility of generating resonance behavior in millimeter scale soft robotic structures to achieve high-speed controllable locomotion.

In chapter 4, the author studied the role of contact interactions between model undulatory swimmers: three-link robots in experiment and multilink swimmers in simulation. The undulatory gait of each swimmer is generated through a time-dependent sinusoidal-like waveform which has a fixed phase offset, ϕ. By varying the phase relationship between neighboring swimmers we seek to study how contact forces and planar configurations are governed by the phase difference between neighboring swimmers. We find that undulatory actuation in close proximity drives neighboring swimmers into planar equilibrium configurations that depend on the actuation phase difference. We propose a model for stable planar configurations of nearest-neighbor undulatory swimmers which we call the gait compatibility condition, which is the set of planar and phase configurations in which no collisions occur. Robotic experiments with two, three, and four swimmers exhibit good agreement with the compatibility model. To study the contact forces and the time-averaged equilibrium between undulatory systems we perform simulations. To probe the interaction potential between undulatory swimmers we apply a small force to each swimmer longitudinally to separate them from the compatible configuration and we measure their steady-state displacement. These studies reveal that undulatory swimmers in close proximity exhibit attractive longitudinal interaction forces that drive the swimmers from incompatible to compatible configurations. This system of undulatory swimmers provides new insight into active-matter systems which move through body undulation. In addition to the importance of velocity and orientation coherence in active-matter swarms, we demonstrate that undulatory phase coherence is also important for generating stable, cohesive group configurations.

In chapter 5, the author demonstrate that contact interactions between undulating robots yield novel phase dynamics such as synchronized motions. We consider undulatory systems in which rhythmic motion emerges from time-independent oscillators that sense and respond

to an undulatory bending angle and speed. In pair experiments, we demonstrate that robot joints will synchronize to in-phase and antiphase oscillations through collisions, and a phase-oscillator model describes the stability of these modes. To understand how contact interactions influence the phase dynamics of larger groups, we perform simulations and experiments of simple three-link undulatory robots that interact only through contact. Collectives synchronize their movements through contact as predicted by the theory, and when the robots can adjust their position in response to contact, we no longer observe antiphase synchronization. Lastly we demonstrate that synchronization dramatically reduces the interaction forces within confined groups of undulatory robots, indicating significant energetic and safety benefits from group synchronization. The theory and experiments in this study illustrate how contact interactions in undulatory active matter can lead to novel collective motion and synchronization.

1.6 Acknowledgement

Chapter 1, in part, is a reprint of the material as it appears in Hao, Z., Zhou, W. and Gravish, N., 2022. Proprioceptive feedback design for gait synchronization in collective undulatory robots. *Advanced Robotics*, pp.1-16. The dissertation author was the co-author of this paper.

Chapter 2

Rapid two-anchor crawling from a millis-cale prismatic-push-pull (3P) robot

Many crawling organisms such as caterpillars and worms use a method of movement in which two or more anchor points alternately push and pull the body forward at a constant frequency. In this chapter we present a milliscale push-pull robot which is capable of operating across a wide range of actuation frequencies thus enabling us to expand our understanding of two-anchor locomotion beyond the low-speed regime. We designed and fabricated a milliscale robot which uses anisotropic friction at two oscillating contact points to propel itself forward in a push-pull fashion. In experiments we varied the oscillation frequency, f, over a wide range (10-250 Hz) and observe a non-linear relationship between robot speed over this full frequency range. At low frequency ($f < 100$ Hz) forward speed increased linearly with frequency. However, at an intermediate push-pull frequency ($f > 100$ Hz) speed was relatively constant with increasing frequency. Lastly, at higher frequency ($f > 170$ Hz) the linear speed-frequency relationship returned. The speed-frequency relationship at low actuation frequencies is consistent with previously described two-anchor models and experiments in biology and robotics, however the higher frequency behavior is inconsistent with two-anchor frictional behavior. To understand the locomotion behavior of our system we first develop a deterministic two-anchor model in which contact forces are determined exactly from static or dynamic friction. Our experiments deviate from the model predictions, and through 3D kinematics measurements we confirm that ground

contact is intermittent in robot locomotion at higher frequencies. By including probabilistic foot slipping behavior in the two-anchor friction model we are able to describe the three-regimes of robot locomotion.

2.1 Introduction

Terrestrial organisms use a multitude of locomotion strategies to move such as walking and running on legs, lateral undulations of the body while slithering, and longitudinal body oscillations during crawling [57]. Ground-based bioinspired robots employ many of the same principles—legs, lateral undulations, and longitudinal undulations. The actuation and control of bioinspired robots in many cases have been informed, and even improved by observations of their biological counterparts.

For example the spring-mass dynamics of legged locomotion have informed robot mechanism and control design [58, 59], the flapping and fixed wing aerodynamics of flight have improved aerial robots [60, 61, 62], and slithering strategies of snakes have enabled snake-like robots to traverse challenging terrain [63, 64]. However, when robots possess actuation, sensory, or control capabilities that supersede the capabilities of the biological system movement behaviors can be pushed to regimes not observed in nature [65]. Robots that are capable of extremal locomotion behavior, pushing far beyond the observed regimes of their biological counterparts, can enable us to test the generality of locomotion models across a wide range.

Crawling locomotion is broadly defined as movement across a surface in which forward progression is enabled by body movements rather than limb movements [57]. A diverse array of animals demonstrate crawling locomotion including insect larvae [66], worms [67], clams [68, 69], and snakes [70]. Similarly, many bioinspired crawling robots have been built and studied across a wide array of mechanical designs including soft-bodied, origami, and rigid crawling robots [71, 72, 73, 74, 75]. Crawling locomotion is typically slow compared to legged locomotion because crawling requires reconfiguration and movement of large body segments

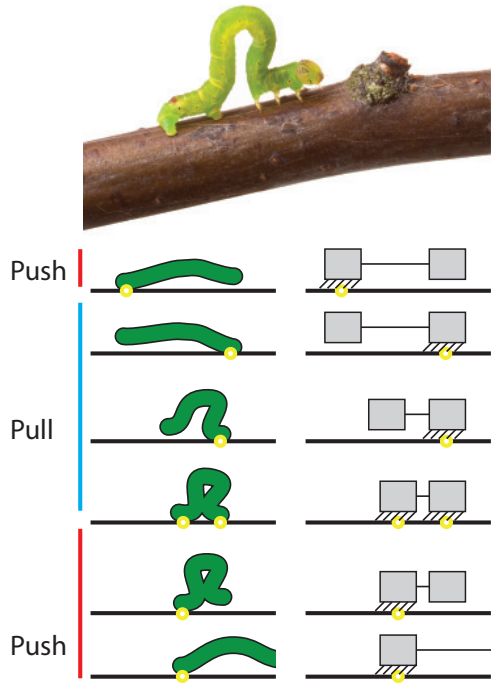

Figure 2.1. An inchworm uses a push-pull strategy of movement (top). Alternating contact points allow the body to be pushed or pulled forward (Bottom left). A simple representation of inchworm crawling is a linear motion of two contact elements that alternate contact with the ground through anisotropic friction (Bottom right). (Top image reproduced with permission from depositphotos. (c) fotofermer (Vadim Dreznol)')

(Fig. 2.1).

A common model used to describe the crawling dynamics of animals and robots is that of a two-anchor system in which two contact points successively push, and then pull the body forward in a repeating pattern (Fig. 2.1) [76, 77, 78, 79]. The two points can independently anchor to the ground to support both body-weight and the required friction force for push-pull advancement. Successful crawling requires some forms of symmetry breaking within the push-pull cycle so that thrust forces can exceed frictional resistance. For example, many animals and robots will lift the body during the push or pull phase thus reducing body friction during advancement [80, 81, 82]. Theoretical models of two-anchor locomotion have explored symmetry breaking methods such as time asymmetry (rapid extension, slow contraction) [77], and alternating the magnitude of push and pull friction forces through mass-swapping [79], or

directional and velocity dependent forces [83].

Anisotropic frictional contacts with the ground is another method employed by animals and robots so that symmetric push and pull sliding movements can generate forward motion through asymmetric friction [84, 85, 86, 87, 88]. Anisotropic friction is one of the keys to snake locomotion during longitudinal gaits [89]. A simple mechanism to generate frictional anisotropy is through angled contact points with the ground, such as has been used in the class of vibration based robots known as bristle-bots [90, 91]. Moreover, vibration based robots can also take advantage of dynamic resonance properties of their actuators, and when coupled with anisotropic friction this can further enhance locomotion capabilities [92, 93]. Thus, forward propulsion in two-anchor robot and animal systems can emerge from contact mechanics, body actuation dynamics, or combinations of both.

Many forms of bio-inspired crawling robots have been developed. The most prevalent bio-inspired crawling robots are inspired from soft-bodied crawling animals such as worms and larvae. These soft-bodied robots are often constructed from soft elastomers that are cast or 3D printed [80, 94, 95, 96, 97], and they are actuated through pneumatic [94, 97, 98, 99], smart actuators such as shape memory alloys [82, 100, 101, 102], or dielectric elastomers [103, 104]. While soft bodies enable a wide range of body flexibility for crawling locomotion [105], actuation speed is a fundamental challenge in soft robotics [106]. Thus, many of the bio-inspired crawling robots move relatively slowly. Recent developments in small, lightweight, laminate robot fabrication [107] coupled with high-bandwidth piezoelectric (PZT) actuation [108] have enabled new ground-based mobile robots capable of extremely high speeds relative to their body size [65, 109]. The design and incorporation of flexure hinges that emulate revolute joints in laminate robots is relatively standardized [110], however generation of linear actuation motions within laminate robotics has been less explored and typically requires exceptional design considerations such as custom actuators [111] or new transmission mechanisms [112, 113].

In this study we present the design and evaluation of a small-scale laminate robot that is actuated by a novel prismatic mechanism and capable of high-speed ground locomotion

(relative to body size). We present this study in three sections. In the first section we describe the design and fabrication of the milliscale push-pull robot that uses two pairs of anisotropic bristles attached to a prismatic transmission. In the second section we describe the locomotion capabilities of this robot across a range of actuation parameters. In the last section of this study we present two models to describe the robot locomotion. We first present the deterministic push-pull model originally developed for quasi-static crawling behavior. We compare this model to our observations and conclude that it fails to capture the complexity of the robot speed-actuation performance. We next introduce a stochastic push-pull model, which captures the observed foot-slippage that occurs at higher frequencies and which is modeled as a stochastic phenomenon. Lastly, we describe the relationship between models and experiments and discuss opportunities for high-speed crawling based robotics.

2.2 Robot design

2.2.1 Overview

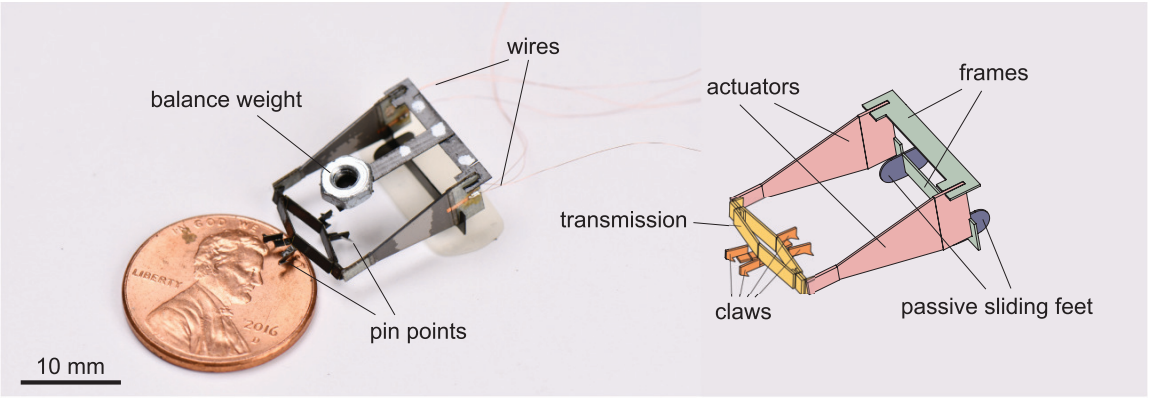

Figure 2.2. The 3*P* Robot shown next to a United States penny for scale (Left). The robot is composed of three main components: the transmission system, the actuators, and the robot frame (Right).

In this section we describe the design and fabrication of a milliscale robot that uses a prismatic transmission for push-pull locomotion. We call this robot 3P for simplicity due to the prismatic push-pull actuation. The 3P robot consists of a carbon-fiber chassis, two actuators,

and a prismatic transmission, as shown in Fig. 2.2. The torso of the robot consists of two PZT actuators symmetrically assembled along the central longitudinal axis. The actuators connect to a prismatic transmission which transforms the lateral oscillations of the actuators into forward oscillations of the robot feet that approximate a linear motion along the fore-aft direction. Two pairs of flexible feet-like structures have bidirectional claws that engage with the ground substrate providing anisotropic friction. A balance weight and a skid plate allow the robot to remain stable on the ground with and without actuation. The robot weighs approximately 500 mg in total, which includes a 200 mg balance weight to adjust the center of mass. In the following sections we describe the robot design and fabrication in depth.

2.2.2 Actuation

The robot uses two bimorph PZT actuators to provide oscillatory inputs to the transmission. Piezoelectric actuators are chosen for three main reasons: (1) their fabrication process is relatively standardized and thus custom shapes can be created in the lab [108], (2) they provide high energy density (peak blocked force $\times$ peak free displacement) [114], and (3) can operate over a wide range of frequencies. Other means of actuating crawling robots such as shape memory alloy [71, 82, 100, 101, 102, 115], pneumatic actuators [72, 94, 97, 98, 99] and liquid crystal elastomers [75] suffer from time delays associated with heating and cooling and thus are not capable of high frequency actuation. Alternatively, other millimeter scale robots have used rotational vibratory motors for actuation [90, 91]. However, off the shelf vibratory motors are not able to independently change actuation amplitude, phase, and frequency.

Each PZT actuator is 15 mm in total length and the PZT plates have a trapezoidal shape with length, 10 mm, and bases of 1.5 mm and 6 mm on the narrow and wide ends, respectively. The actuators are custom fabricated using a diode-pumped solid-state (DPSS) laser, the details of the fabrication process have been thoroughly described elsewhere [108, 116]. The PZT plates are bonded to a central carbon fiber layer which acts to provide a conductive connection to the plates. The central carbon fiber layer also gives the actuator a relatively large bending stiffness

and thus the PZT plates must generate force to overcome this intrinsic stiffness. While in many applications PZT actuators are matched to the system stiffness to achieve a resonance actuation phenomenon with a preferred frequency [60], in the design of 3P the actuators are oversized such that the output amplitude of the actuator and transmission system is constant over the frequency range of interest (See appendix A). Actuators of these size have a typical maximum output displacement of ± 250 μm.

The actuators are driven by a high-voltage PZT amplifier (PiezoDrive TD250) and each actuator requires a ground, bias, and signal voltage for actuation [117]. We connect the ground and bias signals together between the two actuators and thus the robot requires a total of four wires for actuation. The bias voltage is held at $V_B = 200$ V and the signal voltage is oscillated given by the function $V(t) = A\sin(2\pi ft) + \frac{V_B}{2}$ where the A is in the range of $A \in [0, \frac{V_B}{2}]$. Generation of the actuation signals are performed in Labview and a low-voltage analog output signals are provided to the amplifier to control the high-voltage signals through a National Instruments DAQ.

2.2.3 Transmission kinematics

Our robot is designed to perform an oscillatory crawling motion, to achieve this we designed a parallelogram based transmission inspired from [118], to provide a linear push and pull motion (Fig. 2.3a). The design of mechanical transmissions for milliscale robots often requires the use of flexure hinges as opposed to true rotary joints [110]. Flexure-based compliant mechanisms are much easier to fabricate for milliscale systems, and they provide reliable motion that approximates true pin joints, although they can suffer from fatigue if appropriate materials are not chosen [119]. While numerous studies have been conducted to design, model, test, and analyze flexure based mechanisms [110, 120, 121, 122], in our treatment of the transmission kinematics we use a simplified symmetric four-bar linkage where we assume the flexure hinges are ideal pin joints (Fig. 2.3b).

We actuate the transmission with symmetric inputs from the left and right actuators. We assume that the actuators provide a horizontal input displacement to the left and right side of

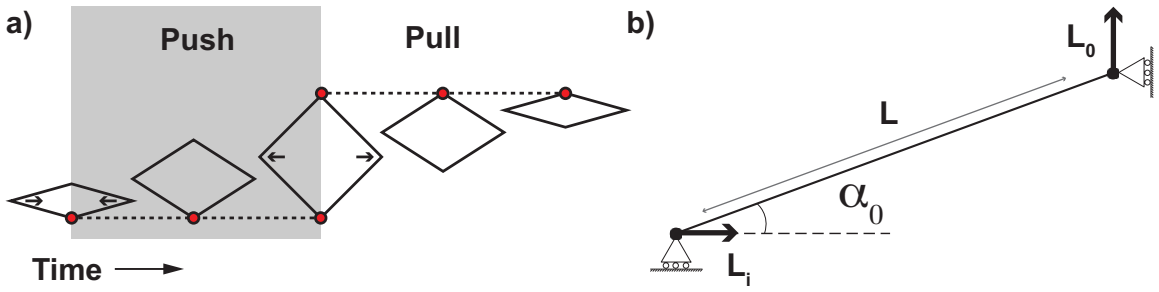

Figure 2.3. Push-pull locomotion and transmission kinematics. a) Top-down view of the transmission movement. Over one oscillation cycle of the actuators the anisotropic feet engage the surface in a push and then a pull motion (red dots indicate foot engagement). b) We consider the upper left quarter of the symmetric transmission to model the kinematics.

the transmission, and we assume the output displacement is in the fore-aft direction (Fig. 2.3a). Due to the symmetry of the transmission and input displacements we can simplify the modeling of the transmission kinematics by focusing on just one quarter of the parallelogram (Fig. 2.3b). An input displacement, L_i, in the horizontal direction generates an output displacement, L_o, in the vertical direction and drives the link, of length L, from an initial angle α_0 to α. The position relationship of the input and output points (in their horizontal and vertical directions respectively) can be written as:

$$L\cos(\alpha_0) - L_i = L\cos(\alpha) \tag{2.1}$$

$$L\sin(\alpha_0) + L_o = L\sin(\alpha) \tag{2.2}$$

We can eliminate the variable α in equations 2.1 and 2.2 and solve for the output displacement L_o, retaining only the positive root

$$L_o = \sqrt{L^2\sin^2(\alpha_0) + 2LL_i\cos(\alpha_0) - L_i^2} - L\sin(\alpha_0) \tag{2.3}$$

To keep the width of our robot approximately 1 cm we chose a link length of L = 5 mm. The actuators we have chosen for our robot have a peak output displacement of ± 250 μm which

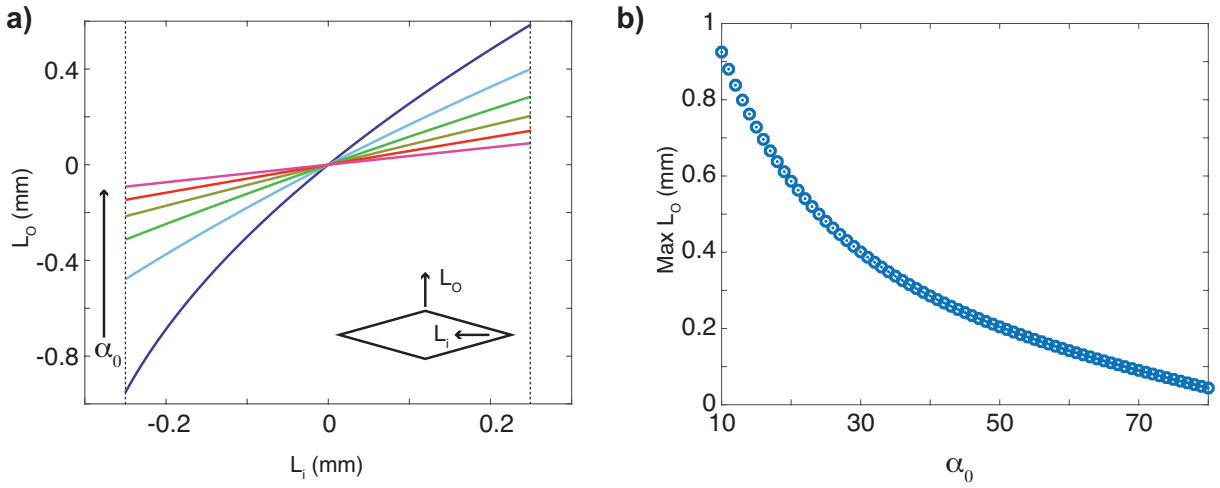

Figure 2.4. Transmission input and output displacement kinematics. The relationship between the input, L_i and output displacement, L_o, of the transmission for different initial angle configurations (Left; α_0 = [10, 20, 30, 40, 50] with arrow showing direction of increase). The maximum output displacement for an input of L_i = 250 μm as a function of α_0 (Right).

places a constraint on the geometry of our transmission. For a fixed amplitude input, increasing the default parallelogram angle (α_0) results in a decrease of the transmission amplitude (Fig. 2.4). For low α_0 the transmission is moderately nonlinear while as α_0 increases the transmission becomes more linear.

We selected an α_0 of 10° for our transmission based in part on the kinematics and additional practical requirements of the robot. A low α_0 is favorable for our design because it provides a large amplification of displacement while requiring only modest bend angles of the flexure hinges. The flexure joints are approximated as pin joints for the purposes of kinematic analysis, but in reality they provide a torsional resistance to bending roughly consistent with a torsional spring. Thus large flexure bend angles result in large internal torques that the actuators must overcome and may reduce the force output of the transmission. Lastly, a shallow transmission angle also enables easier fabrication because there is less internal elastic resistance in the transmission while it is being bent and assembled.

2.2.4 Transmission fabrication

The smart-composite manufacturing (SCM) method [123, 124] was used to build our robotic system. Our transmission was designed using a single laminate consisting of 25 layers as a single monolithic structure to reduce the number of folds which significant influence the assembly accuracy (Fig. 2.5). In the appendix A we provide details of the laminate layers and geometry. Briefly, the SCM process involves multiple steps of laser cutting individual layers of structural (carbon fiber), flexure (Kapton), and adhesive (DuPont Pyralux) layers. These layers are bonded together in a thermal press and after multiple cut-and-cure steps the final transmission is laser cut from the surrounding multi-layer laminate.

Manual folding and gluing is required to complete the feet assembly and to attach the claws. The folding joints in Fig. 2.5a are folded 90° to form the foot structures shown in Fig. 2.5b. The tips of four insect pins (#00, diameter = 0.27 mm) were removed and used as angled claws providing anisotropic ground friction. The claws were adhered to the transmission feet at approximately 45° with respect to horizontal plane [91]. Previous research has found that pins placed at an angle can increase the anisotropic friction coefficients between sliding and stance phase. Setting the pin angle to approximately 45° results in the claws engaging the highest amount of asperities as possible [74, 125]. To accommodate the uneven surface, we designed

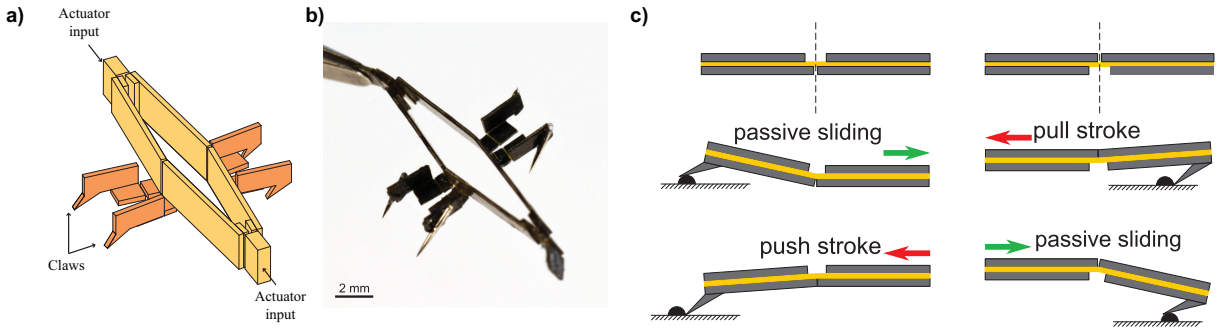

Figure 2.5. Transmission design and fabrication. a) Isometric schematic of transmission showing actuator inputs on the left and right, and the pairs of push-pull claws. b) Photo of completed linear transmission with claws. c) Conceptual push-pull operation with passive flexures to enable sliding and locking of claws.

passive joints with an asymmetric joint stopper to allow the pin to accommodate different contact angles (Fig. 2.5c). This enhanced the engagement of the claws with ground during the thrust stroke while reducing friction during the passive return stroke.

2.3 Robot locomotion

We performed several experiments to identify the performance and behaviors of the sub-components of our robot (claws, transmission, actuators) in addition to studying the robot locomotion performance. First we measured the transmission kinematics and compared to theory. Next we measured the anisotropic friction performance of the bi-directional claws and body. Lastly we studied the forward motion of the robot under self-actuation in an unconstrained and a linearly constrained experimental configuration.

2.3.1 Transmission kinematics experiment and model comparison

To study the transmission kinematics under prescribed input displacement we assembled a benchtop testing station. The linear transmission and two bimorph piezoeletric (PZT) actuators were assembled together onto an acrylic testing base (Fig. 2.6a). A single high speed camera (Phantom VEO410) was used to capture the motion of the transmission and viewed the transmission perpendicular to the input and output motions. The actuators were calibrated such that the two actuator tips provided identical displacement inputs to the left and right side of the transmission, Fig. 2.6b (left). We tracked the motion of the transmission input and output using the DLTdv5 package in Matlab [126]. The input motion was prescribed to be sinusoidal, and the output motion of the transmission was observed to be an asymmetric periodic function (Fig. 2.6b).

We compared the experimental tip displacement to analytical results from the model using the same geometric dimensions from the design. The experimental output amplitude was smaller than that from the model prediction (Eqn. 2.3). It is likely that the output transmission kinematics are over predicted by the model because the rotational flexures are modeled as ideal

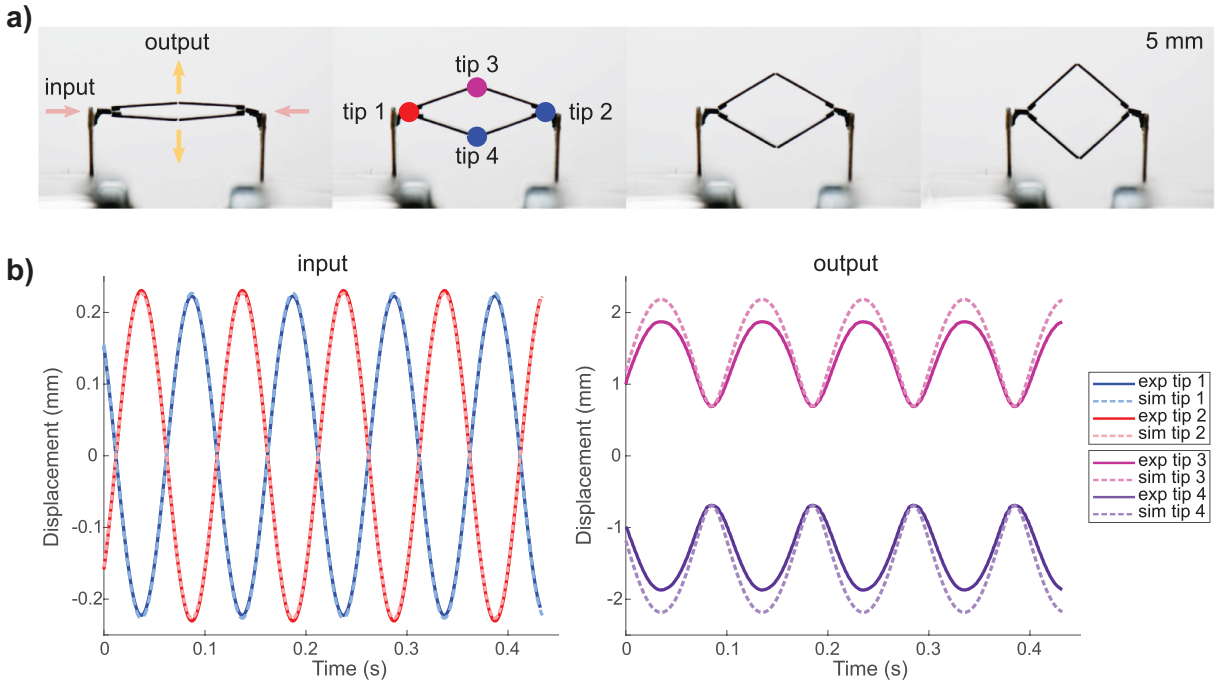

Figure 2.6. Transmission test results. a) Linear transmission on testing stage. b) Comparison of input and output motion of the linear transmission in experiments and simulation.

pin joints, when in reality they can compress and bend with non-zero radius of curvature. Similar disparities between flexure and ideal joint modeling has been previously demonstrated [120]. To improve our model of the kinematics we adjusted the effective transmission length L using a least-squares fitting routine. We found that an effective transmission length of $0.6L$ provided good agreement between experiment and the model. These experiments demonstrated that the transmission was capable of smooth and highly repeatable motion over a wide-range of input displacements and frequencies. Experiments up to frequencies of 250 Hz did not result in significant amplitude change (see appendix for frequency sweep) indicating that dynamic effects of the transmission can be ignored in future analysis.

2.3.2 Anisotropic friction from angled claws and body

The robot claws slide across the substrate in the forward and backwards direction along the direction of movement (Fig. 2.5). When the claws are sliding away from the robot body (in the forward direction) the friction ideally should be low, and when the claw is sliding back

toward the robot body (in the backwards direction) the friction should be high.

To determine the peak backwards sliding force that the angled claws can provide for thrust we assembled a friction testing experiment and we performed two separate measurements. In the first experiment the robot was attached to a force sensor by a thin wire (FUTEK LSB200-FSH02663; 500 mN max rating). The force sensor was mounted on a motor controlled displacement stage (Thorlabs MT S50) which displaced the force sensor and robot at a constant speed of 2.3 mm/s in a direction that engaged the angled claws against the substrate. The robot was placed on a substrate of card stock paper (the same used for locomotion experiments). The robot was not actuated and we measured the sliding force of the claws against the card stock substrate, which resulted in a claw propulsion force measurement of 21.1 ± 3.4 mN. In a second experiment we held the force sensor fixed and we allowed the robot to pull itself forward against the force sensor. In these measurements we observed a range of peak propulsion forces from the claws with an average propulsion of 47 ± 18 mN average peak force. The observed forces in the second set of experiments were larger likely because the actuation of the foot (at 80 Hz) enabled the claw to secure optimal footholds at a faster rate than when the robot was passively dragged. From these force measurements we estimate that the coefficient of friction for each claw in the propulsion direction is $\mu_+ = 9.6$. It is not unexpected for angled claw-like objects interacting with rough surfaces to have a friction coefficient substantially greater than unity [127].

To verify the force asymmetry from the claws we also determined the resisting force acting against the forward motion of the robot. To measure the stopping force against the robot we measured the dynamics of the robot coming to rest from a constant initial velocity, v. We used a high-speed camera to record the stopping of the robot while passively sliding and coming to rest. We computed the resistive force coefficient acting against the robot by fitting the position versus time with a constant resisting force μmg. We measured a resistive force friction coefficient of $\mu_- = 0.33$ corresponding to a resistive force of 1.62 mN acting against the forward motion of the robot. These experiments provided quantitative measurements of the force asymmetry from the angled claws and demonstrate that this robot has a force ratio of approximately 40 times in

propulsive force compared to resistive force.

2.3.3 Robot locomotion performance

We investigated the locomotion performance of the robot on card stock paper across a range of actuation frequencies. Two high-speed cameras with frame rate set to 20 times the driving frequency were used to capture the motion of the robot from side and top view, which enabled 3D reconstruction of the robot motion profiles. We conducted two sets of experiment: (1) the robot was confined move along a straight line by two bounding walls, and (2) the robot was able to move freely over the surface. We provide further details of the experimental setup in the appendix A.

In figure 2.7 we show several examples of the position and velocity of the robot for four driving frequencies when the robot was unconfined. The robot position was tracked using the DLTdv5 package, and the velocity was estimated using Kalman filters based on the tracked position data. At low driving frequencies, for example 30 Hz, the velocity of the robot has large velocity fluctuations at the same frequency as the actuation (30 Hz). The robot body motion exhibits behavior that is reminiscent of a stop-start type of locomotion, which is also consistent with a previously described model of two-anchor locomotion in which the body is accelerated from rest at the beginning of the half-cycle and then comes to rest at the end of the half-cycle [57]. However, the stochastic nature of the body velocity indicates that the robot body does not come to rest exactly at the end of every half-cycle and suggests a possible importance of stochastic foot-ground interactions in the robot locomotion.

At higher driving frequency, for example 50 Hz, the velocity of the robot continued to display high-frequency fluctuations at the driving frequency. However, as actuation frequency increased we observed that the robot did not always come to rest at the end of the actuation cycle indicating that the robot had begun to slide forward near the end of a half-cycle. This suggests that at higher frequencies the locomotion behavior starts to violate the quasi-static assumption which requires that forward motion only occurs while the robot is actively pulling against the

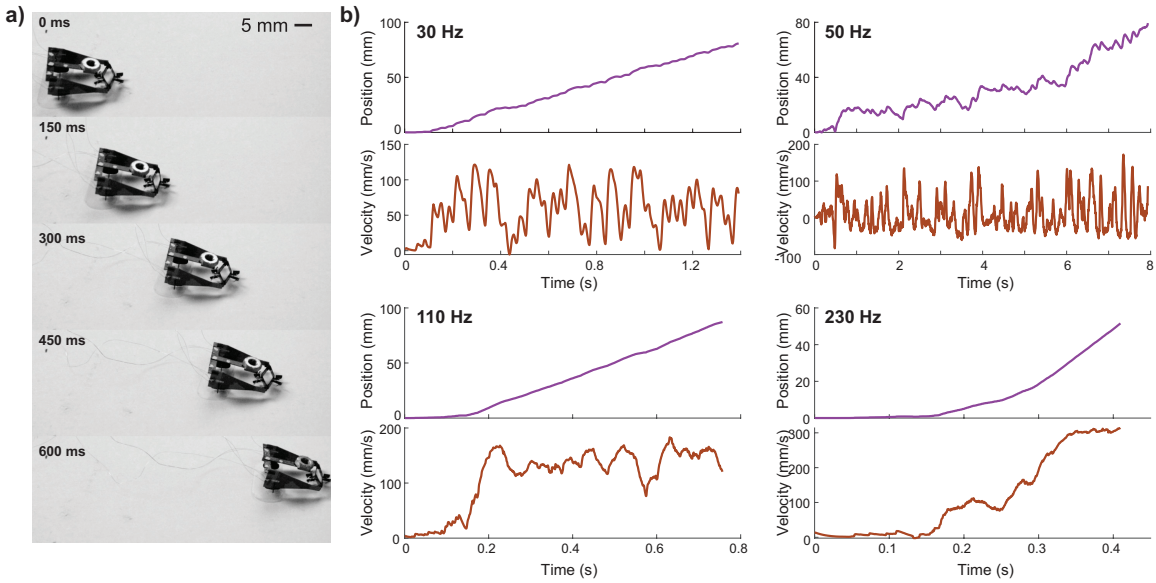

Figure 2.7. 3*P* Robot locomotion examples. a) Example of 3P robot moving from left to right at 90 Hz driving frequency. b) Four examples of position and velocity versus time for the 3P robot moving at different driving frequencies.

ground.

At frequencies above 110 Hz the instantaneous velocity of the robot was relatively smooth and greater than zero, indicating the presence of a substantial gliding type of motion propelled by the sequential acceleration and deceleration from the oscillatory claw movements. The relatively smooth velocity fluctuations at these high frequencies compared to lower frequency (approximately below 110 Hz) may be the result of foot slippage during the forward acceleration phase of the half-cycle. For the body to move in a no-slip manner the friction force must be larger than the required inertial acceleration, which for a purely sinusoidal foot motion would be $mA\omega^2$.

The overall kinematic relationship between actuation frequency and average speed is shown shown in Fig. 2.8. In both the free-run and the tunnel-run experiments we observed a similar trend in the speed-frequency relationship. We observed an approximately linear increase in average velocity with driving frequency from 10 Hz to 100 Hz. The average velocity reached a plateau from frequencies 100 Hz to 170 Hz, and then increased again at frequencies higher

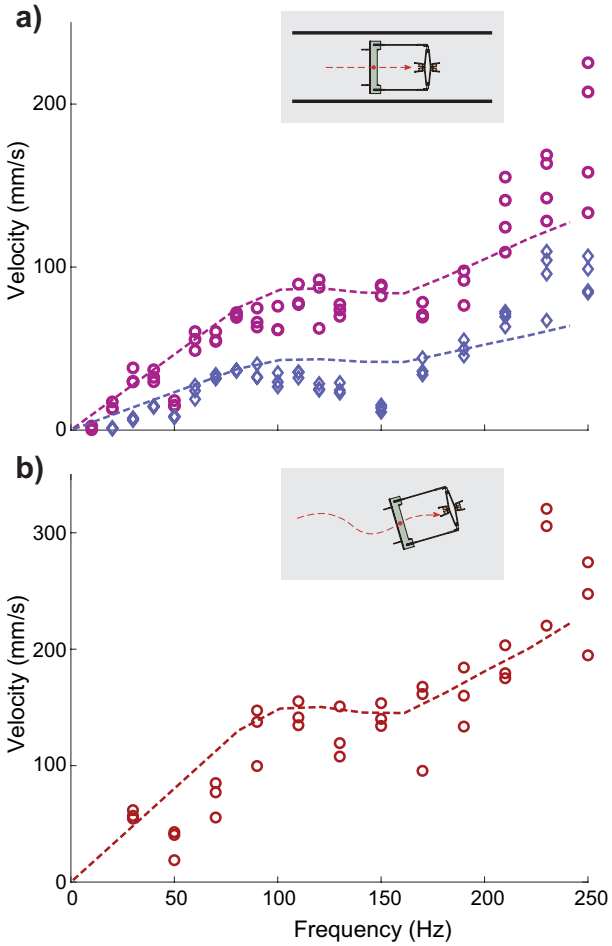

Figure 2.8. Average velocity of 3*P* Robot across different driving frequencies. a) 3P experiments performed in tunnel to enforce linear motion. Purple circles indicate experiments where the robot were driven at full amplitude. Blue diamonds indicate experiments where the robot were driven at half amplitude. Dashed lines are results from model developed in section 4. (b) 3P robot experiments without walls. Full amplitude experiments are shown in red circles.

than 170 Hz. In the free-run and tunnel-run experiments we observed a sharp decrease in speed at 50 Hz, which we correlated with a body resonance mode in which large vertical vibration could be observed in the high-speed videos. In the tunnel-run experiments we performed testing at two actuator amplitudes (Fig. 2.8a) and we observe a speed decrease for the lower amplitude experiments with a similar trend in the non-linear speed-frequency relationship.

The velocity trends are similar between the robot experiments in the constrained tunnel and on the unconstrained substrate. The primary difference between these experiments that the

average velocity of the robot was higher in the unconstrained substrate experiments compared to the tunnel experiments. In the tunnel experiments, the robot was constrained to move in a straight direction and thus collisions between the robot and the walls likely result in an average decrease in the robot speed. The vertical oscillation of the robot which is characterised by the standard deviation of vertical displacement increases linearly with driving frequency.

To determine the relative motion of the claws with respect to the ground we tracked the position of the robot claws across all frequencies in the free-run experiments. We specifically seek to determine the occurrence of claw slipping, which can occur in the forward direction (expected because of the low coefficient of forward friction) and potentially in the backward direction if the actuators exceed the friction force the claws can support during propulsion. In previous models of two-anchor crawling foot slipping was not considered and thus the average speed would be expected to increase linearly with increased oscillation frequency [57]. However, Coulomb friction is present in nearly all robots foot-ground interactions and thus understanding the prevalence claw slipping is important [128, 129, 130]. For our analysis we assume a claw can be in one of three possible states: (1) approximately stationary with respect to the ground when the magnitude of the claw velocity is below a velocity threshold of 35 mm/s, (2) slipping forwards away from the body with positive claw-ground velocity along the direction of motion either through forward body gliding, or during the second half of the actuation cycle in which the claw is being reset for the thrust phase, (3) slipping backwards toward the body with negative claw-ground velocity, which only occurs when the claw is slipping during the power stroke of the thrust.

Claw tracking reveals that there is a strong frequency dependence to the claw-ground interaction (Fig. 2.9). At low actuation frequency the claw slips during the propulsion phase of the actuation approximately 20% of the time ((Fig. 2.9b) while the claw remains in approximate stationary contact approximately 30% of the time. As the actuation frequency is increased the probability to observe the claw slipping during the propulsion phase (backward slip) increased. The relative ratios of forward slip, backward slip, and approximately stationary are well fit by

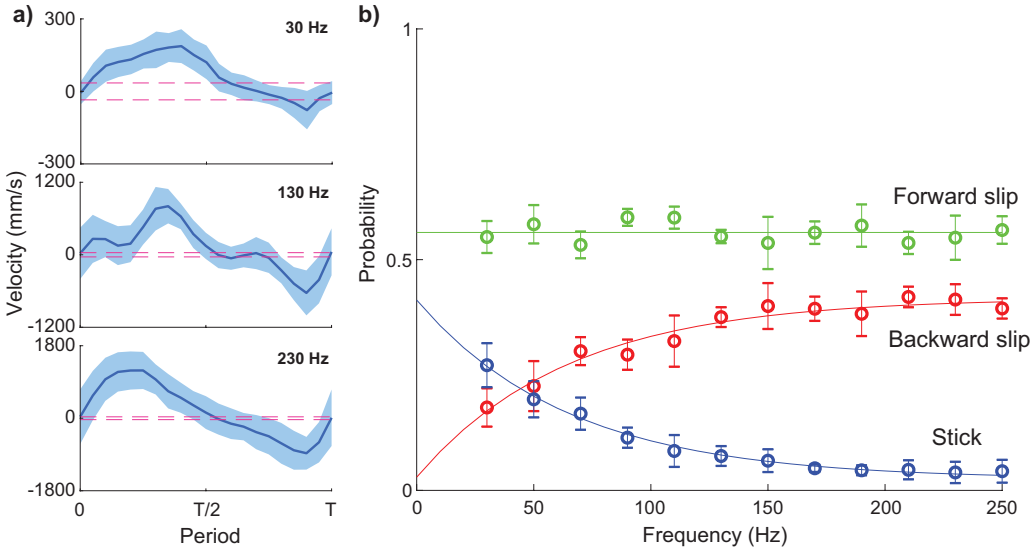

Figure 2.9. Robot foot tracking results. (a) Foot velocity in one period at low (30 Hz), intermediate (130 Hz), and high (230 Hz) frequencies. Red dash lines represent the threshold of whether the foot is assumed to be stationary with the ground (sticking) or not. (b) Ratio of foot status in one period across different frequencies.

three functions that cumulatively are constrained to sum to probability 1 for each frequency. The forward slip probability is constant across frequency, given by $P_{forward} = 0.559$. However, the backward slip and approximate sticking probabilities are fit by saturating exponential curves, $P_{stick} = 0.388 * \exp(-0.015 * f) + 0.024$ and $P_{backward} = -0.388 * \exp(-0.015 * x) + 0.417$. The frequency dependence of the claw slipping behavior is likely correlated with the increased robot vibration that we observe as frequency increases. If the robot is excited by a high-frequency actuator it can cause body vibrations that can dislodge the engaged claw and likely result in the increased slipping probability we observe.

2.4 Dynamics of push-pull locomotion

The nonlinear speed versus frequency behavior of the robot motion is surprising given previous studies of two-anchor crawling locomotion [57]. The simplest approach to modeling two-anchor locomotion assumes that no-slipping occurs and thus the average robot speed should be a linear function of the actuation frequency. However, friction dynamics of vibration based

locomotion are extremely important such as in anisotropic friction vibration based robots [90, 91] as well as stick-slip isotropic friction robots [93, 131]. To understand the relationship between speed and frequency for our robot we now will develop a mathematical model of two-anchor locomotion that considers both forward and backward slipping of the foot.

The organization of this section is as follows. We first introduce the notation for a deterministic two-anchor model in which the claw-ground interaction is determined solely by anisotropic Coulomb friction. We present the results of this model using parameters informed from our experiments and observe that this model lacks the ability to model the mid-frequency plateau we observe in speed. Next, we introduce a stochastic claw-ground slipping probability into our model to account for the frequency dependent claw-ground interaction. The inclusion of this increased probability to slip at increased frequency generates a speed-frequency that captures the non-linear plateau we observe in our data. Previous models of two-anchor locomotion have been developed and extensively analyzed in previous works [77, 79], however our approach differs in two fundamental ways: (1) instead of controlling the actuation force between the two-anchors we impose time-dependent kinematics and solve for body movement, and (2) we incorporate probabilistic slip events inspired from our observations of frequent stochastic foot slipping.

We developed a simple model for the push-pull locomotion of our robot (Fig. 2.10a). In this model, we assume the robot with mass m is driven by sinusoidal push-pull motion of two claws and thus we neglect any potential dynamics that could be present in the actuation system. This decision is supported by the relatively small change in transmission amplitude versus frequency (See appendix A). We impose time-dependent kinematics of the position of the two claws measured with respect to the body

$$l_1(t) = A\cos(\omega t) \tag{2.4}$$

$$l_2(t) = -A\cos(\omega t) \tag{2.5}$$

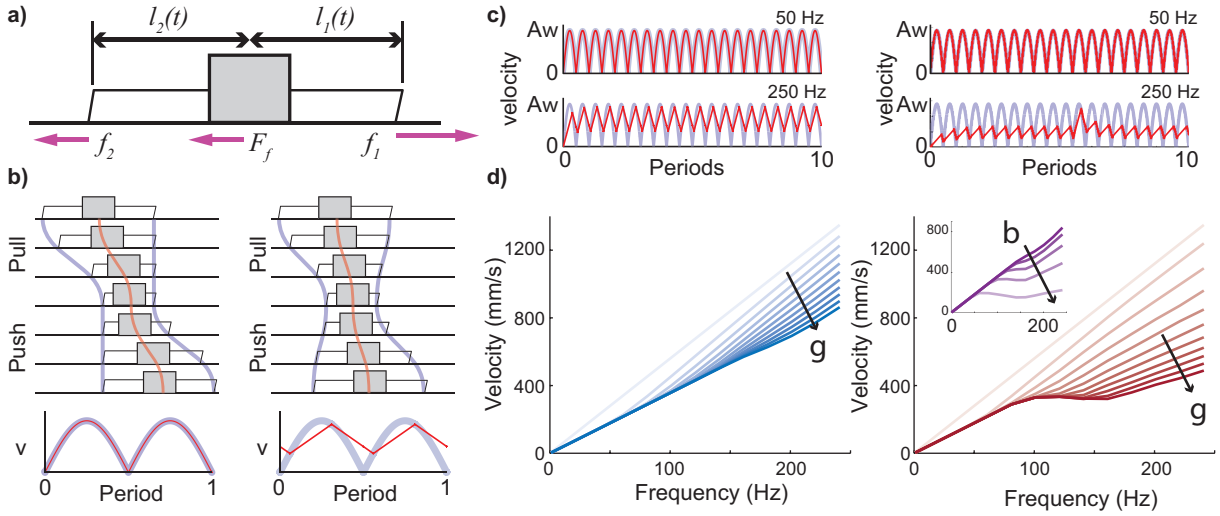

Figure 2.10. Model of push-pull locomotion dynamics. a) Sketch of push-pull model. b) Examples of low (left) and high (right) frequency dynamics in a deterministic model. Blue lines represent reference velocities of robot body with no-slip claw engagement. Red solid lines represent robot body velocities in the simulation. c) Velocity examples of the deterministic (left) and the stochastic model (right) at low (50 Hz) and high (250 Hz) frequencies with $\gamma = 1.0$. Blue lines represent reference velocities of robot body with no-slip claw engagement. Red solid lines represent robot body velocities in the simulation. Time is scaled to period of oscillation, and velocity is scaled to $A\omega$. d) Velocity prediction of the deterministic (left) and the stochastic (right) model with force ratio γ increasing as designated by arrow (from 0 to 1). In stochastic simulations $\beta = 0.3$. Inset on right plot illustrates variation as β is changed from 0.9 to 0.1 ($\gamma = 1.0$).

where A is the amplitude of claw oscillation and $\omega = 2\pi f$, where f is the actuation frequency.

As the two claws move with respect to the body they generate ground reaction forces f_1, f_2 (Fig. 2.5a). A positive ground reaction force indicates a thrust force propelling the robot in the forward direction, a negative ground reaction force is a braking force acting against forward motion. We assume that the claw forces interact only through anisotropic friction with a force range

$$F^- \leq f_i \leq F^+, \; i = 1,2 \tag{2.6}$$

where F^+ and F^- represent the maximum thrust force ($F^+ > 0$) and the maximum braking force ($F^- \leq 0$) of the claws.

During the pull stroke, the leading claw retracts toward the body and provides a positive force, while the trailing claw retracts toward the leading foot and slides passively on the ground generating a negative force $f_2 = F^-$. At the beginning of the push stroke the claws are near each other, the claws push away from each other and the trailing claw provides a positive force while the leading claw extends away from the body and slides passively on the ground generating resisting force $f_1 = F^-$. The push-pull motion is illustrated in Fig. 2.10b. Throughout the push and pull motions the robot chassis passively slides on ground, generating a friction force:

$$F_f = \text{sign}(\dot{x}_b)\mu mg \tag{2.7}$$

where $\dot{x}_b$ is the velocity of the robot, μ is the coefficient of friction of the robot chassis, and g is gravity.

When a claw's velocity with respect to the ground is zero, then the foot is stationary and we call the foot anchored. The equation of motion of the robot when a propelling foot is anchored is given by the following:

$$m\ddot{x}_b = f_i + F^- + F_f \tag{2.8}$$

where $\ddot{x}_b$ is the acceleration of the robot and, i=1 during the pull stroke and i=2 during the push stroke. The propelling foot undergoes a backward slip if the velocity of the foot is negative, which leads to a foot-ground force of:

$$f_i = F^+,\ i = 1 \text{ at pull stroke};\ i = 2 \text{ at push stroke} \tag{2.9}$$

and thus an equation of motion of:

$$m\ddot{x}_b = F^+ + F^- + F_f \tag{2.10}$$

Lastly, the propelling foot slips forward when the velocity of the foot is positive. In this case the foot-ground force is

$$f_i = F^-,\ i = 1 \text{ at pull stroke};\ i = 2 \text{ at push stroke} \tag{2.11}$$

thus

$$m\ddot{x}_b = F^- + F^- + F_f \tag{2.12}$$

From the analysis above, we can simplify the ground-reqction forces from the multiple contact points to a maximum total thrust force and a maximum total resisting force that occur during the different phases of motion as:

$$F^+_{max} = F^+ + F^- + F_f \tag{2.13}$$

$$F^-_{max} = F^- + F^- + F_f \tag{2.14}$$

$$\tag{2.15}$$

From this observation of a maximum and minimum force range of the robot we defined a ratio of the force asymmetry between F^+_{max} and F^-_{max} as:

$$\gamma = \frac{\|F^-_{max}\|}{\|F^+_{max}\|} \tag{2.16}$$

Large γ corresponds to a highly anisotropic friction force, while when $\gamma = 1$ the friction force from the claws are isotropic with no distinction between F^+ and F^-.

At each push and pull stroke, the claws are trying to propel the motion of robot body in a no-slip manner such that the body acceleration would be exactly equal to the acceleration of the

transmission

$$a = A(2\pi f)^2 \cos\left(\text{mod}(2\pi f t, \pi)\right) \tag{2.17}$$

If the required force to propel the body, $f_{eff} = ma$, is lower than the possible maximum frictional force of the engaged claw, $F_{max}^{-} \leq f_{eff} \leq F_{max}^{+}$, then the motion of the robot is completely described by the motion of the transmission (Fig. 2.10b, left column) and the foot does not slip. Otherwise the required force exceeds the force limits of claws and the robot body and claws will slip on the ground (Fig. 2.10b, right column).

We simulated the dynamic model by setting $F_{max}^{+} = A(2\pi f)^2$ with specific $f = 150$ Hz to represent the maximum total propelling force. We set $A = 0.89$ mm according to the tracking data of the transmission output amplitude in the robot locomotion experiments. The relationship between the average velocity and the actuation frequency is shown in Fig. 2.10c left column. The robot velocity increased linearly when $\gamma = 0$ there is no resisting force against the robot, which meant that the steady state of robot velocity was fully determined by the maximum velocity of the robot transmission $v_{max} = A(2\pi f)$. When γ is nonzero, the robot velocity as a function of frequency diverged from the top-speed ($\gamma = 0$) curve and resulted in lower speeds at the same actuation frequency compared to the $\gamma = 0$ case. Critically, when $\gamma > 0$ the robot undergoes a combination of sticking and slipping as it moves, determined by the force relationship between the resisting (F_{max}^{-}) and the propulsive (F_{max}^{+}) forces. At low frequency actuation the force limit F_{max}^{-} and F_{max}^{+} are large enough such that the robot does not slip in the forward (glide) or backwards (back-slip) direction and the velocity follows an exact positive half sin wave. However γ is increased, the robot experiences higher resisting force and thus the robot to does not glide at higher frequencies which results in the lowered average speed curves versus frequency (Fig. 2.10c). When $\gamma = 0$ the robot builds up speed by gliding faster and faster until reaching the terminal velocity determined by the maximum transmission speed.

The predicted velocity trend lines of the deterministic model do exhibit a slight nonlinear

trend as a function of frequency. However, the extent of the velocity plateau did not match the observed experiments over a wide exploration of simulation parameters. Furthermore, our investigation of the claw slipping dynamics revealed that the robot feet were constantly slipping in the backwards direction during the propulsion phase even at low frequencies (Fig. 2.9). We included the effect of frequency-dependent claw slipping into the deterministic model described above by stochastically modulating the peak force that a claw can provide against the ground. The probability fit curves associated with the fit functions in Fig. 2.9 were used to determine the peak claw force of a sticking event.

During the beginning of each propulsion stroke we randomly assigned the claw to either stick, or slip dependent on the frequency of actuation and the measured probability of sticking or slipping. If the claw was set to interact with with ground through sticking, we set $F^+ = F_{high}$, while if the claw was set to slip backwards, we set $F^- = F_{low}$. This resulted in a range of maximum propelling forces based on the status of claws:

$$F^+_{max,high} = F_{high} + F^- + F_f \tag{2.18}$$

$$F^+_{max,low} = F_{low} + F^- + F_f \tag{2.19}$$

To parameterize the force difference between slipping and sticking forces during the propulsion phase we defined the ratio of $F^+ = F_{high}$ and $F^- = F_{low}$ as:

$$\beta = \frac{F^+_{max,low}}{F^+_{max,high}} \tag{2.20}$$

Examination of the simulation behavior illustrates that inclusion of the frequency-dependent stochastic effect of claw slipping during the propulsion phase was able to reproduce the linear-plateau-linear speed-frequency relationship that we observed in experiment (Fig. 2.10). The magnitude of β determines the relative disparity between the propulsion force while sticking and while slipping. When $\beta = 1$ the slipping and sticking propulsion forces are the same, and

when $\beta < 1$ then the slipping force is less than the sticking force (the most physically realistic case). We found that by inclusion of this stochastic slipping behavior the simple model captured the velocity behavior observed in experiment from low frequency to high frequency.

2.5 Discussion and outlook

We have presented the design of a millimeter-scale ground robot that operates using an inchworm inspired push-pull actuation strategy. This robot is able to operate at frequencies substantially higher than its biological counterparts or other previously developed worm-like robots. This robot shows substantially different speed-frequency results when compared to the theoretical predictions for deterministic push-pull locomotion. In particular the speeds we observed were well below what would be observed from a deterministic push-pull model suggesting potential complications to the modeling of claw-ground interaction. This discrepancy led us to the observation that the anisotropic claws exhibited substantial slipping, and that the fraction of time in which the claw was approximately stationary with respect to the ground diminished with increasing actuation frequency. By measuring the frequency dependent probability for the claw-ground states and including this into the model of push-pull locomotion we were able to capture the speed-frequency behavior of this robot.

Slipping is a common phenomena in legged locomotion. Sometimes slipping can be detrimental and result in falls or loss of thrust. However, slipping can also be beneficial as it allows a claw to potentially slip to a stronger foothold. In simplified models of legged locomotion we typically assume that the shear strength of a frictional foot-contact is determined by the normal force and coefficient of friction at that foothold. However, as our experiments highlight the shear resistance of frictional contacts can be variable and highly dependent on the claw and ground geometry [127]. In our experiments the friction variability is likely due to the heterogeneous structure of natural substrates such as the card-stock we use for our experiments. The strength of a frictional contact will encompass a range of possible values determined by the

means of contact formation (how hard or gently the contact is formed for example), as well as the substrate heterogeneity.

Despite the significant foot slipping our robot exhibited it still was capable of relatively fast locomotion, with a maximum velocity of 434 mm/s (24 body lengths/s). The rapid speed is observed at the highest actuation frequency tested (250 Hz) and the speed-frequency trend is suggestive that higher speeds may be achievable at higher frequencies. Comparison of locomotion speed is complicated by the observation that smaller animals and robots tend to move faster on a relative scale (body lengths/s) but slower on an absolute scale. Compared to similar sized robots 3P is at the upper end of reported ground speeds for mobile robots that do not use wheels (see [132] for a comprehensive review of body size normalized robot speeds). Thus, through improvements in slip-resistance and actuation we may be able to achieve even higher speeds.

The high-frequency actuation of this robot enabled us to study a bio-inspired locomotion model well beyond the biologically relevant actuation regime. Actuating a robot with a worm-inspired locomotion strategy revealed that when foot slip is incorporated into a push-pull model we observe a nonlinear relationship between speed and frequency. This is an example of a broader class of experiments at the interface of biology and robotics which seek to use bio-inspired robots to study principles of movement. For example, recent experiments with a milliscale legged robot that is capable of actuation frequencies well outside the biological regime revealed a rich palette of locomotion modes not observed in animals [65]. Experiments that seek to elucidate general principles of locomotion will benefit from experimental platforms that encompass the range of natural locomotion but also enable us to look at the extremes to determine how well our models hold.

2.6 Acknowledgement

We thank members of the Gravish lab for helpful discussion and comments. Funding support was provided by the mechanical & aerospace engineering department at UC San Diego.

Chapter 2, in full, is a reprint of the material as it appears in Zhou, W. and Gravish, N., 2020. Rapid two-anchor crawling from a milliscale prismatic-push–pull (3P) robot. *Bioinspiration & Biomimetics*, 15(6), p.065001. The dissertation author was the primary researcher and the first author of this paper.

Chapter 3

Soft microrobotic transmissions enable rapid ground-based locomotion

In this chapter we present the design, fabrication, testing, and control of a 0.4 g milliscale robot employing a soft polymer flexure transmission for rapid ground movement. The robot was constructed through a combination of two methods: smart-composite-manufacturing (SCM) process to fabricate the actuators and robot chassis, and silicone elastomer molding and casting to fabricate a soft flexure transmission. We actuate the flexure transmission using two customized piezoelectric (PZT) actuators that attach to the transmission inputs. Through high-frequency oscillations, the actuators are capable of exciting vibrational resonance modes of the transmission which result in motion amplification on the transmission output. Directional spines on the transmission output generate traction force with the ground and drive the robot forward. By varying the excitation frequency of the soft transmission we can control locomotion speed, and when the transmission is oscillated at its resonance frequency we achieve high speeds with a peak speed of 439 mm/s (22 body lengths/s). By exciting traveling waves through the soft transmission, we were able to control the steering direction. Overall this chapter demonstrates the feasibility of generating resonance behavior in millimeter scale soft robotic structures to achieve high-speed controllable locomotion.

3.1 Introduction

Millimeter scale robots (millirobots) have potential applications in the near future for autonomous navigation and inspection in hard to reach environments [133]. Millirobots can fit within narrow channels and confined spaces such as pipes, between walls, and within the crevasses of rubble. Furthermore, millirobots also have the potential for large quantity production and thus could be fabricated and deployed rapidly at the site of use [134].

Motivated by these applications, researchers have built numerous milliscale robots in prior work [75, 135, 136, 137, 138, 139, 140]. As the scale of robots decreases such that components or even the whole robot are one to several millimeters, standard parts, such as bolts-and-nuts, gears, and rotary elements such as bearing, are no longer commercially available or feasible for design. Novel methods have been developed to build robots at small scales over the years. 3D printing technology has been used to build small-scale robots from the 6 g 3DFlex robot [141] to a 1 mg legged microrobot [142]. The smart-composite-method [123, 124] has been used to build a 1.7 g hexapod HAMR^3 [137], a 3 cm flapping-wing MAV [143], and many more examples. Similar origami approaches that utilize substantial material folding [144, 145] have also been developed for miniature robots. Advances in smart materials have also enabled development of millimeter scale soft-bodied robots [146].

Different ground locomotion methods have been adopted by millirobots in previous work to adapt to various environments. Wheeled locomotion [135] is fast and efficient, however, friction at the rotational joint becomes problematic as the dimension of a robot decreases. Legged robots [136, 137] with multiple degree of freedom (DOF) limbs possess the advantage of traversing rough terrain, while it also adds complexity to the robot fabrication. Vibration driven bristle-bots [147, 148, 132] generate forward movement through angled spines. Crawling motion inspired by caterpillar terrestrial locomotion is also used in ground robots [75], which can be modeled as a two-anchor system in which two contact points successively push, and then pull the body forward in a repeating pattern. Our robot utilized this push-pull motion to propel

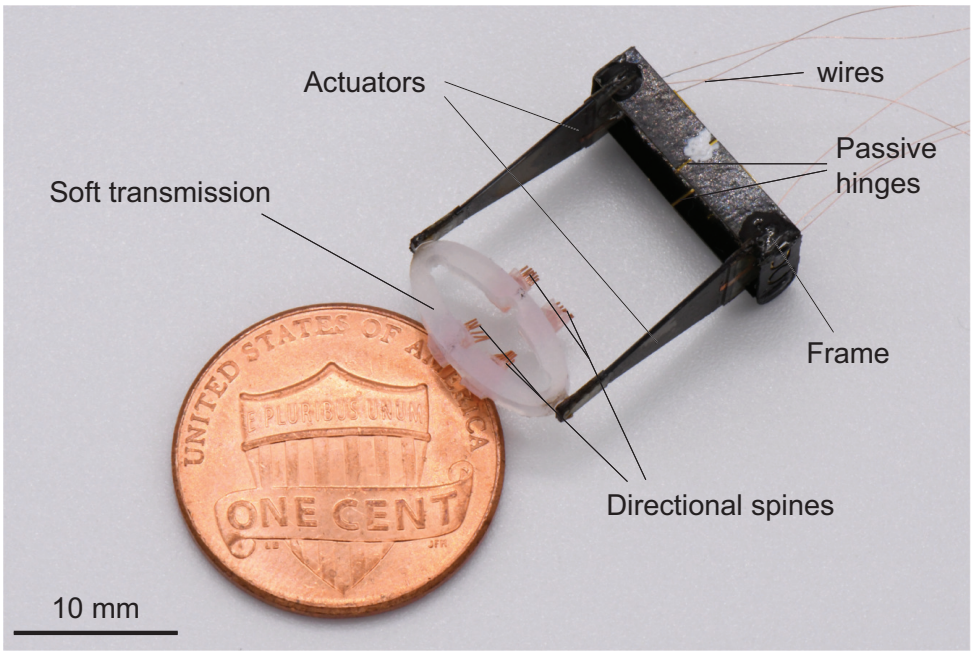

Figure 3.1. Millirobot with soft transmission. Two piezoelectric actuators are connected at their base to a rigid carbon-fiber chassis. Passive hinges along the mid-line of the chassis allow the robot to flex. The tips of the actuators are connected to a silicone soft robotic transmission. Pairs of directional spines are attached to the output of the transmission.

itself forward.

Robots fabricated by rigid materials can provide precise and predictable motion. However, the link-joint structure of rigid robots, even at the millimeter scale, can limit or even inhibit novel dynamics that may be useful for locomotion purposes. Furthermore, generating complex articulated motion with rigid robots requires multiple actuated DOF, which can be an extreme challenge in micro robots with limited power and actuation capabilities. Lastly, microrobots with their ability to explore confined spaces may further benefit from adopting soft robotic components to enable abilities such as squeezing, stretching, growing, and morphing [149].

As an initial step towards bringing soft robotics components to millirobots we seek to develop and study the locomotion capabilities of a vibrationally actuated soft transmission. Many examples of soft robots and soft robotic components are fabricated from flexible, elastic polymers such as silicone rubber. Silicone is an easily castable polymer that is capable of large extension, is highly elastic, and is extremely resilient to a variety of adverse environmental

conditions. For the purposes of locomotion the elastic properties of a soft robotic transmission may enable optimal vibrational behaviors such as resonance for rapid locomotion. Furthermore, a soft robotic transmission would be capable of a continuum of deformations, and thus actuation could be programmed to generate complex vibrational wave forms through the transmission to enable robot steering.

In this chapter we explore the capabilities of using a soft robotic transmission for generation of high-speed ground locomotion. We describe the design, fabrication, testing, and steering control of a milliscale robot 20 mm in body length, that uses two pairs of spines attached to an ellipse-shaped compliant soft robotic transmission. We present design parameters for the soft transmission and measure its dynamic properties in experiments. Open-loop locomotion experiments display fast relative speed capabilities of up to 22 body lengths/s. Steering control is achieved by PZT actuator phase modulation.

3.2 Soft transmission design

PZT actuators have been widely used in micro robots because of their high power density, fast response, steady performance, and high bandwidth [114, 117]. However, due to the stiff materials they are composed of most PZT actuators have a limited deflection range and to achieve larger deflection is often at the sacrifice of force output. Thus, integration of PZT actuators into milliscale robots has spawned the development of novel displacement amplifying mechanisms.

3.2.1 Ellipse shape soft transmission

We chose an elliptical shaped soft robotic flexure as our base shape for our millirobot transmission. The aspect ratio of the ellipse was chosen such that small amplitude deflection inputs on the lateral sides of the transmission result in larger output deflections. We integrated variable size cutouts into the ellipse transmission at the lateral and vertical quadrants. These cutouts enabled more focused displacements at these regions and the control of the wall thickness, t, at these cutouts enabled transmission stiffness control, Fig. 3.2a. Based on previous work

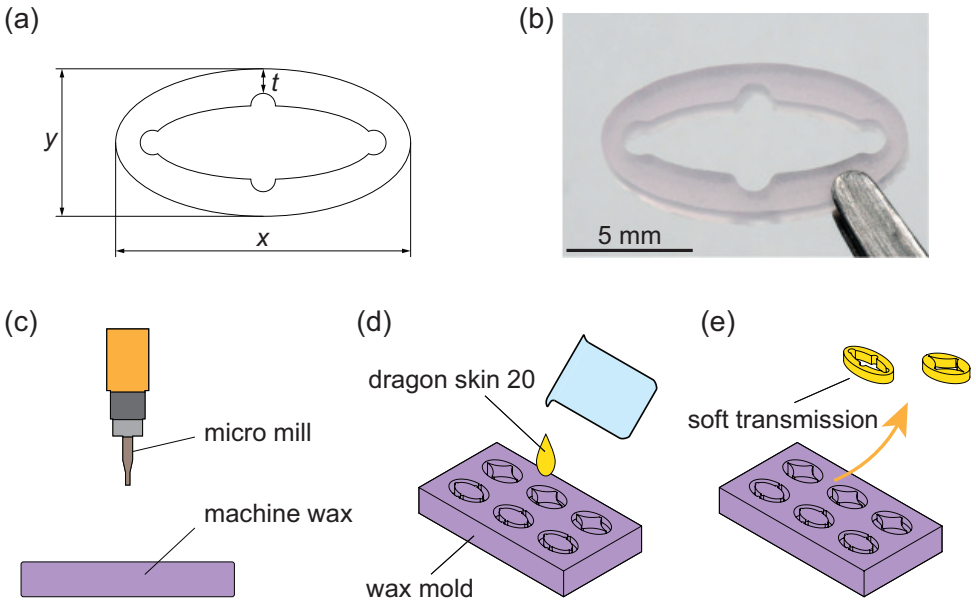

Figure 3.2. Soft transmission design and fabrication. (a) Transmission dimensions. (b) Silicon rubber soft transmission. (c) Building mold using micro mill. (d) Casting with *Dragon Skin 20*. (e) Remove parts from mold.

of modeling flexure-based mechanism [120, 150], the transmission dimensions of $x = 12$ mm, $y = 6$ mm can provide an amplifying ratio of approximately $n = 2$, as shown in Fig. 3.2a. Although displacement amplification can result in a decrease of output force, our PZT actuators can still provide sufficient driving force to the robot. A variety of shapes of soft transmissions (for example diamond shaped, bridge shaped, as shown in Fig. 3.2e) were tested which turned out to be equivalent to the elliptical shaped ones with different wall thickness, t. Thus we focused on analyzing the influence of wall thickness on dynamic properties of the soft transmissions. However, an opportunity we seek to explore in this soft transmission is how deviations from link-flexure based rigid transmissions can be exploited for locomotion capabilities.

3.2.2 Soft transmission molding and casting

To fabricate the soft transmission we needed to be able to precisely generate negative molds for them. The size of the transmissions prohibit 3D printing and instead we found machining with a desktop mill to be an economical option. We fabricated molds from machine

wax using a commercial micro mill (Othermill). We used an end mill of size $1/64$ inch in diameter which enabled us to build soft transmissions with flexure thickness t ranging from 0.5 mm to 1.0 mm. The machining process took approximately one hour and we generated five molds for each transmission shape profile.

We used a commercially available silicone polymer, Dragon Skin 20, to cast the transmissions. We mixed Dragon Skin 20 part A and part B at ratio 1 : 1 for 10 minutes and then poured into the mold. The silicone rubber was set to rest and cure at room temperature for 4 hours. We manually removed the transmissions after curing completion Fig. 3.2b. After removal from the mold transmissions were ready to be integrated into the robot.

3.2.3 Soft transmission static stiffness

We used a finite element method (FEM) analysis to analyze the static stiffness of the silicone rubber soft transmissions. We developed a 3D model of the transmission in SolidWorks and then used built-in FEM analysis to generate a prediction of stiffness change with transmission geometry. We observed that stress concentrations occurred at the cutouts of the soft flexure, where its thickness is small, as would be expected. For the the thin walled transmission (0.5 mm), the cutouts enabled the transmission to act somewhat like a series of four revolute joints and links at the thin flexure. However, the larger thickness walls behaved more like a continuum elastic structure with more homogeneous stress and strain distribution throughout the transmission. The continuum motion of the transmission body enables shape control and contributes to steering capabilities that wouldn't be possible with a rigid joint-link transmission.

3.2.4 Soft transmission dynamic proprieties

As a first determination of the the applicability of a soft transmission for ground locomotion we measured the resonant oscillations of each transmission design. Experiments were conducted to test the dynamic proprieties of a series of soft transmission with different flexure thicknesses. We mounted each transmission between two symmetric bimorph PZT actuators

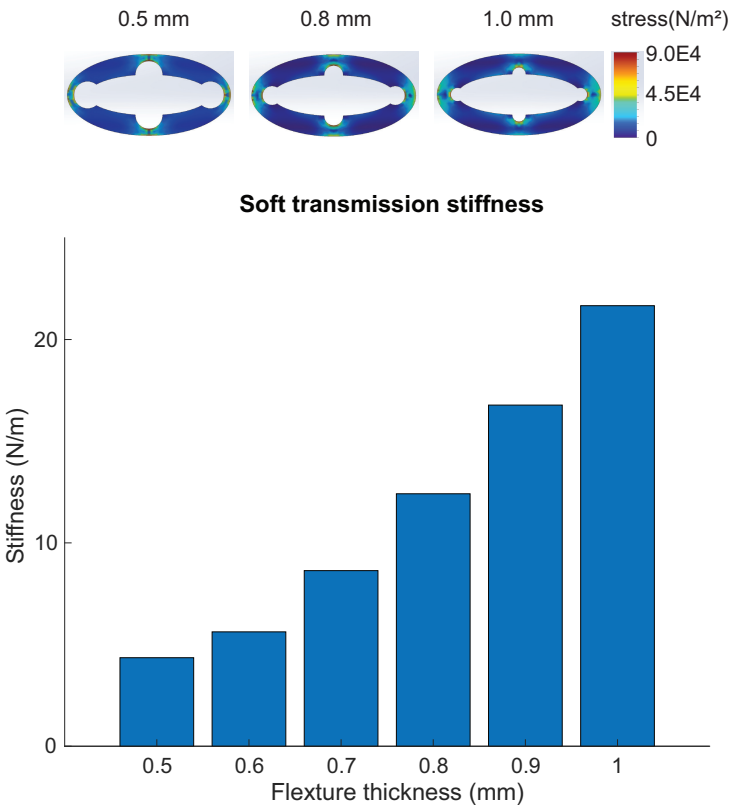

Figure 3.3. Finite-element-analysis of the soft transmission results in an increasing stiffness with increasing wall thickness. Above plot shows snapshots of stress during typical deformation.

with a fixed base. The actuators were driven by a sinusoidal voltage signal from 10 Hz to 260 Hz to test the dynamic response of the soft transmission system and find out the optimal operating frequency. Experiments with individual actuators have resolved their resonant frequency to be above 1 kHz when not attached to a load. A high-speed camera was set up with a variable frame rate equal to 20 times the driving signal frequency to capture the vibrational motion of the soft transmissions as shown in Fig. 3.4a. We then tracked the input motion Δx of the two PZT actuators and the output motion Δy of the soft transmissions by analyzing videos in MATLAB, as shown in Fig. 3.4b. Δx and Δy are the change of distance of two actuating tips and two output tips. The ratio of output amplitude to input amplitude reflects the transmission ratio of the amplitude.

We built 3 batches of each soft transmission design with different flexure thicknesses and tested their dynamic properties individually. Figure 3.4c shows the frequency response of all soft

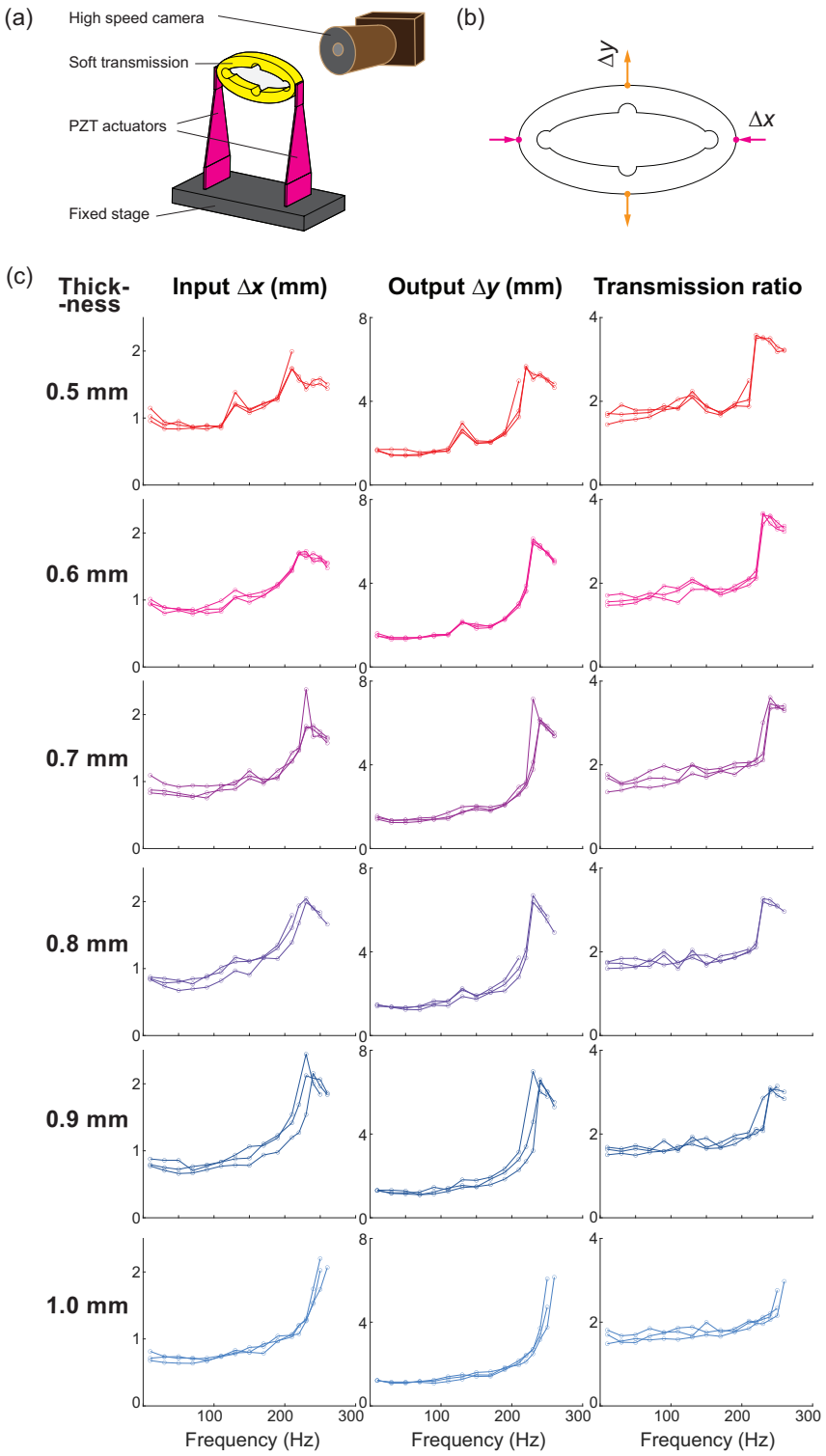

Figure 3.4. Dynamic properties of soft transmission. (a) Experiment setup. (b) Tracking input Δx and output Δy. (c) Frequency response of soft transmissions with different flexure thickness.

transmissions with each trial overlaid. The dynamic behavior of soft transmissions from different batches have quite consistent performances. The standard deviation of the soft transmission input and output are 0.06 mm and 0.15 mm respectively. It suggests that wide-scale production of milliscale soft robot components may be achieved through this process. The silicone rubber soft transmissions act as mass-spring systems, and we observe that all transmission-actuator combinations exhibit a resonance mode between 200 Hz to 260 Hz depending on their flexure thickness. Predictions of the resonance frequency is complicated by the stiffness of the actuators (which are in series with the transmission), and the varying transmission mass with varied geometry. However, general trends may be observed such as the smaller flexure thicknesses result in soft transmissions with lower effective stiffness, and a lower resonance frequency. The transmission ratios at low driving frequency are approximately 2, which matches the prediction from our transmission design. However, the ratios have a significant jump at the system resonance frequency because the input and output amplitudes are larger and the working range of transmissions has shifted. The large amplitude oscillations at resonance are an ideal actuation target to potentially achieve high-speed ground based movement.

3.3 Robot design

3.3.1 Robot fabrication

The chassis of the robot is fabricated through the smart-composite-manufacturing (SCM) process. The SCM process consists of laser cutting layers of structural, flexural, and adhesive sheets, and then bonding them together. A final release cut removes the articulated component with joints and links from the supporting scaffold. Furthermore, this same process can be used to cut and fabricate piezoelectric actuators. Carbon fiber layers were used to build the structure of the frame, while two passive Kapton hinges were created on the robot frame along the central axis to couple the flexible bending of the soft transmission.

Two bimorph PZT actuators were used for actuation on our robot. The actuators are

15 mm in total length, where the PZT plate is an isosceles trapezoid whose height is 10 mm and two bases are 1.5 mm and 6 mm respectively. The two PZT actuators were assembled symmetrically across the central axis of a carbon fiber SCM fabricated frame. The actuators were rigidly attached to the frame with epoxy, and power wires were soldered to the base of the actuators. The soft transmission with wall thickness, $t = 0.8$ mm, was attached to the actuator tips using super glue carefully applied to the transmission edges. To enable ground traction, we attached directional spines to the output of the transmission. The directional spines were made by an array of copper wires of diameter 0.1 mm whose front ends were sealed in silicon rubber while rear ends were bent to 45° with respect to ground. The dimension of the robot is 15 mm $\times$ 20 mm and the weight is 0.4 g. The robot with a reference object is presented in Fig.3.1.

3.3.2 Robot locomotion

We conducted experiments to investigate the robot locomotion performance on sandpaper of 1 micron grid size. The robot was driven by two PZT actuators at frequency from 10 Hz to 250 Hz, while its locomotion was captured by a high speed camera from above, as shown is Fig. 3.5a.

For open-loop trials the two actuators were provided with two identical sinusoidal signals at same amplitude and 0° phase difference. The robot trajectories of locomotion in the $x-y$ plane were recorded and shown in Fig. 3.5b. With no amplitude or phase difference of the actuator control signals, the robot trajectories in the lateral direction demonstrate a random pattern which was caused by the initial conditions of the robot, unpredicted ground reaction of the spines, drag of the wires, and other side effects. However, across 39 trials we recorded the lateral (y) deviation of the robot when it reached a forward distance of $x = 50$ mm. The mean value of the robot lateral variation is approximately 0, as shown in Fig. 3.5c, which suggests the robot has no steering preference in open-loop. However, the wide range in lateral deviation does indicate the need for active feedback control of robot trajectory in future implementations.

Robot average velocities at different frequencies are shown in Fig. 3.5d. The sharp

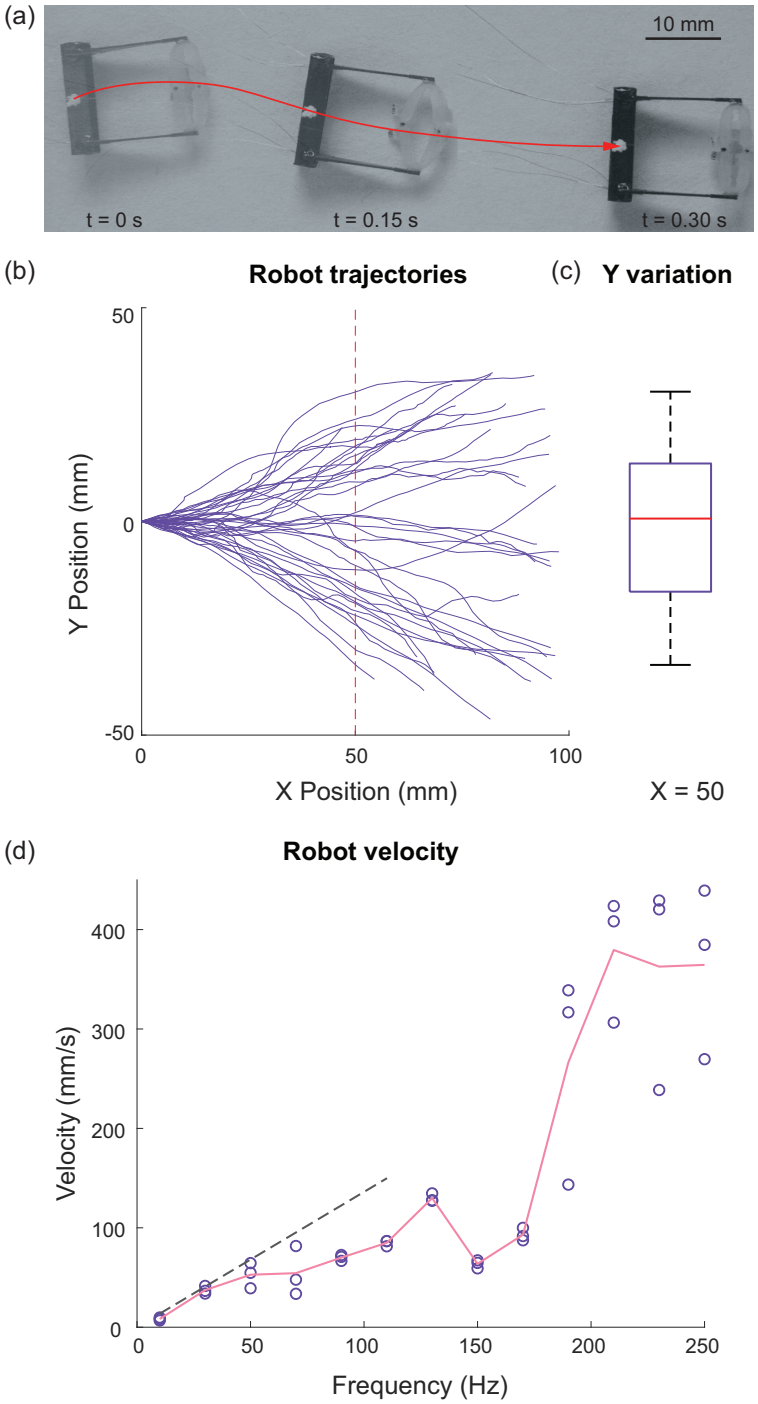

Figure 3.5. Robot locomotion experiments. (a) Example of robot operating at 250 Hz. (b) Trajectories of robot open-loop operation. (c) Robot y variation at $x = 50$ mm. (d) Robot speed at different driving frequency. Circles are experiment trials. Red solid line is average velocity trend line. Gray dashed line is model trend line at low frequency.

increase in speed that occurs as the frequency approaches 200 Hz matches closely the observed dynamic response of the soft transmission. This indicates that despite ground contact and sliding, the dynamic response of the robot appears consistent with that of the transmission-actuator combination. If the robot is not slipping, the speed should be proportional to the fore-aft amplitude of the transmission at the spines, multiplied by the stride frequency. The stride length, which can be also treated as the transmission output Δy, is relatively constant and low at lower driving frequency. Therefore, the increase of speed at low frequency is largely a result of the increase in driving frequency. We took the average of transmission output Δy from 10 Hz to 110 Hz as the robot stride length at lower frequency, and drew the predicted model trend line in Fig. 3.5d. The experiment data matches the model trend line pretty well. Robot velocity starts diverging from the trend line with the increase of frequency because slipping is more severe at higher frequency. The peak of the robot velocity at 130 Hz was caused by a secondary resonance mode of the soft transmission which can also be found in the frequency response. However, the robot reaches its maximum speed when it's operating around the dynamic resonance frequency of the transmission. Our recorded maximum average speed is 439 mm/s, equivalently 22 body lengths/s.

3.3.3 Travelling wave in soft transmission

Robot turning behavior is a phenomenon that may utilize the soft behavior of the transmission. The soft transmission made from silicone rubber has the ability to generate complex shape change under different driving signals, which contributes to the turning of the robot. Using high-speed visualization and tracking we measured this shape change to observe the soft transmission shape change dynamics.

As shown is Fig. 3.6a, we describe the instantaneous shape of the transmission by the radius $\mathrm{R}(\theta)$ at given angle θ. $\mathrm{R}(\theta)$ is the radial distance from the center of the ellipsoid transmission to the contour of the transmission with an angle θ. When driving signals are applied on left and right sides of the transmission, the transmission will deform, causing shape change of

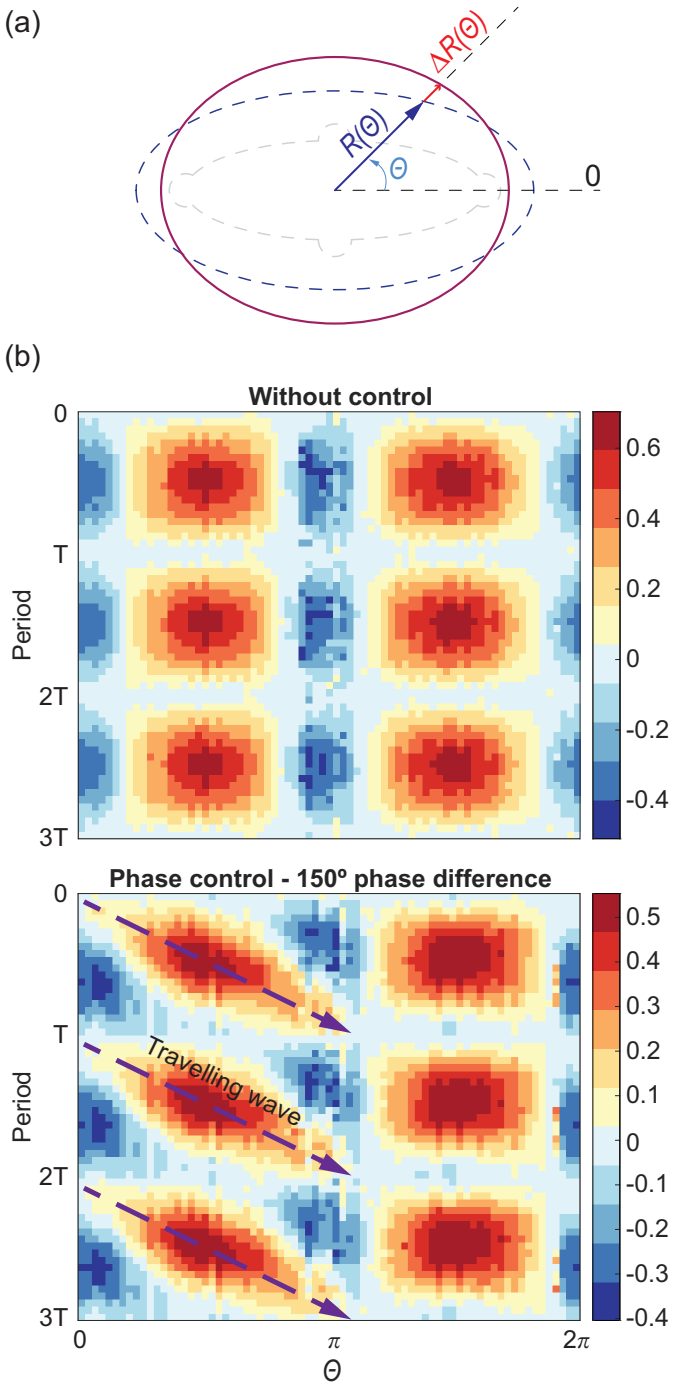

Figure 3.6. Vibrational behavior of the soft transmission in straight and turning modes. a) Diagram of the deformation measurement. b) Space-time visualizations of transmission deformation with time on y-axis and angular position on x-axis. (Top) Without phase control the oscillations of the transmission are symmetric and periodic. (Bottom) With a phase difference between actuators we see the excitation of traveling waves that move from low to high θ.

the transmission contour. We tracked the axis length change $\Delta R(\theta)$ of the transmission over time when it was driven by different signals. Heat maps were generated to depict the transmission contour shape change, with color reflecting the value of $\Delta R(\theta)$. The x axis of the heat maps are θ ranging from $0 - 2\pi$; y axis is time over 3 driving cycles.

Piezoelectric actuation with simultaneous drive method [117] was used on the PZT actuators where tip displacement of an actuator is a linear map of the driving signal applied. When steering control was not engaged, i.e., two identical sinusoidal signals were applied to the PZT actuators, the transmission moved symmetrically along the central vertical axis (where $\theta = \pi/2$). Thus, $\Delta R(\theta)$ was also symmetric all the time, Fig. 3.6b.

When we changed the phase difference of the two sinusoidal signals, the shape change of the soft transmission became more complex. The right actuator was set to have a 150° phase lead ahead of the left one. A significant wave propagation was observed on the upper half rim of the transmission, while extra glue between the transmission and actuators at lower half rim likely limited the wave propagation motion. The wave motion is observed in Fig. 3.6b as the slope. This wave motion of the soft transmission is key to the robot steering in phase control.

3.3.4 Robot steering

The open-loop results indicate that the robot will tend to deviate from a straight path if left uncontrolled. Thus as a first step to implementing robot control we here investigate potential actuation methods that enable robot turning. From the observation of travelling waves in the soft transmission, we propose a robot steering strategy through phase control.

In phase control, we use phase differences between the left and right actuator to excite a traveling wave from left to right, or right to left. We achieved controlled turning by changing the phase difference of the two sinusoidal driving signals. The robot will turn left when the left actuator has phase lead over the right one, while it will turn right when the right actuator has phase lead over the left one. Since the turning control is symmetric, we tested only right turn behavior in this experiment. We each conducted 5 runs with varied phase difference from 90° to

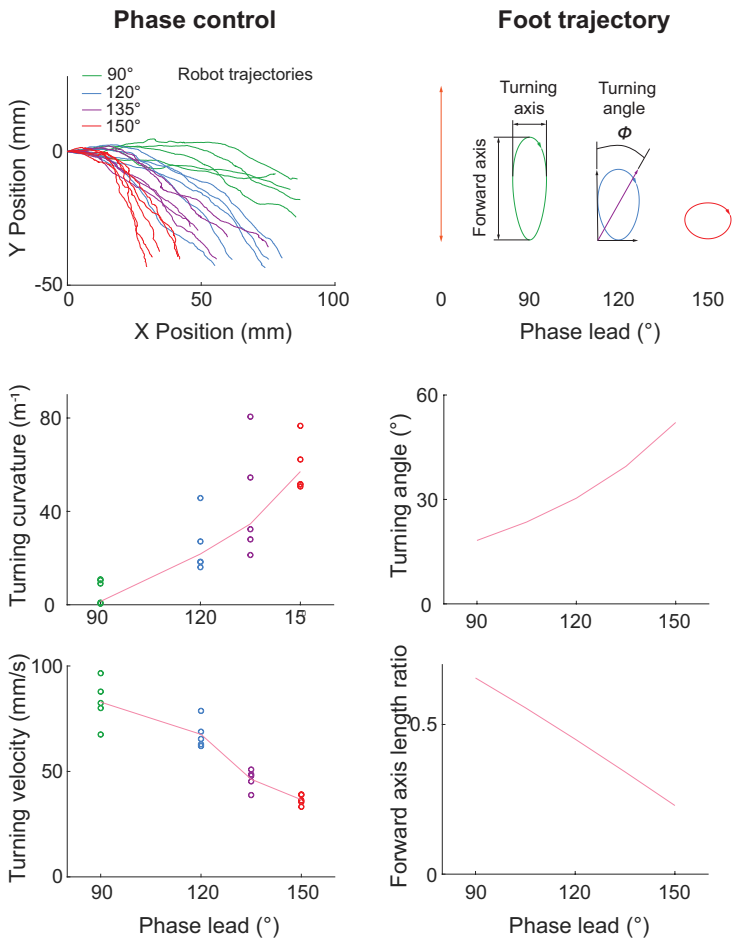

Figure 3.7. Robot turning experiments. Left column: robot turning by phase control. Right column: robot foot trajectory predicted by kinematic model.

150°. Robot trajectories are shown in Fig. 3.7(top, left), based on which we estimated the turning curvature (mid, left) and speed (bottom, left) for each run. The turning curvature increases with the phase lead while speed decrease with phase lead.

A simple flexure-linkage model of the transmission provided an estimate of the foot trajectories at different actuator phase lead/lag. When the phase difference is 0, the two actuators move symmetrically, driving the feet forward and backward on a straight line. When phase difference is introduced, feet trajectories become ellipse like, Fig. 3.7(top, right). We define the ellipse axis aligned with the robot body as the forward axis while the ellipse axis on the perpendicular direction as the turning axis. We also define the angle between the forward axis

and the diagonal formed by the forward axis and the turning axis as the turning angle Φ.

The turning angle increases with the increasing phase difference between left and right actuator control signals. The turning angle likely contributes to the the turning ability of the robot. Comparison between robot turning curvature and the turning angle prediction in Fig. 3.7 shows good qualitative agreement between turning prediction and experiment. As the actuator phase difference increases from 0, the forward amplitude of the transmission motion decreases. We normalized the forward axis lengths at different phase difference to the maximum amplitude, at phase difference of 0. We find that the fore-aft displacement of the transmission decreases linearly as shown in Fig. 3.7(bottom, right). The decrease in amplitude reduces the effective stride length of the robot, and thus this is likely the cause of the lower the speed during turning.

3.4 Conclusion

By combining smart-composite-manufacturing fabrication processes used for rigid robots, with a micro-machining and casting method employed for soft robotics, we have attempted to integrate soft robotic components into millimeter scale robots. Through dynamic characterization we identify that the soft transmissions achieve resonant behavior around 200 Hz oscillation frequencies. By driving these frequencies when the robot is in contact with the ground we were able to achieve remarkably high-speed ground locomotion for a millimeter scale robot; capable of moving at 439 mm/s which is equivalent to 22 body lengths/s, at resonance frequency. This work has focused on the design and control of the soft transmission system to enable rapid locomotion at resonant frequency and future work will explore integration of more soft robotic structures into the robot design ultimately aiming towards soft millimeter scale robots capable of high-speed movement.

3.5 Acknowledgment

We acknowledge funding support from the Mechanical & Aerospace Engineering Department. We thank Professor Michael Tolley for use of his micro-machining mill.

Chapter 3, in full, is a reprint of the material as it appears in Zhou, W. and Gravish, N., 2020. Soft Microrobotic Transmissions Enable Rapid Ground-Based Locomotion. In *2020 IEEE/RSJ International Conference on Intelligent Robots and Systems (IROS)* (pp. 7874-7880). IEEE. The dissertation author was the primary researcher and the first author of this paper.

Chapter 4

Lateral contact yields longitudinal cohesion in active undulatory systems

Many animals and robots move using undulatory motion of their bodies. When the bodies are in close proximity undulatory motion can lead to novel collective behavior such as gait synchronization, spatial reconfiguration, and clustering. Here we study the role of contact interactions between model undulatory swimmers: three-link robots in experiment and multilink swimmers in simulation. The undulatory gait of each swimmer is generated through a time-dependent sinusoidal-like waveform which has a fixed phase offset, ϕ. By varying the phase relationship between neighboring swimmers we seek to study how contact forces and planar configurations are governed by the phase difference between neighboring swimmers. We find that undulatory actuation in close proximity drives neighboring swimmers into planar equilibrium configurations that depend on the actuation phase difference. We propose a model for stable planar configurations of nearest-neighbor undulatory swimmers which we call the gait compatibility condition, which is the set of planar and phase configurations in which no collisions occur. Robotic experiments with two, three, and four swimmers exhibit good agreement with the compatibility model. To study the contact forces and the time-averaged equilibrium between undulatory systems we perform simulations. To probe the interaction potential between undulatory swimmers we apply a small force to each swimmer longitudinally to separate them from the compatible configuration and we measure their steady-state displacement. These studies

reveal that undulatory swimmers in close proximity exhibit attractive longitudinal interaction forces that drive the swimmers from incompatible to compatible configurations. This system of undulatory swimmers provides new insight into active-matter systems which move through body undulation. In addition to the importance of velocity and orientation coherence in active-matter swarms, we demonstrate that undulatory phase coherence is also important for generating stable, cohesive group configurations.

4.1 Introduction

The field of active matter has been inspired by the collective behavior of biological systems [151]. The principles of these systems are that individuals move through self-propulsion and that interactions occur through mechanical forces often mediated through hydrodynamic or contact forces [152]. Animal groups across scales from bacteria [12, 153], insects [154, 16], fish [19, 20], and birds [155, 156] exhibit coordinated movement patterns such as group flocking and swarming. In groups of larger animals such as birds and fish the collective movements are generated through visual sensory cues [22, 23] and hydrodynamic interactions between the individuals [26, 27, 28, 29]. However, smaller scale systems such as swimming bacteria, sperm, and worms, that often swim in higher group densities may experience repulsive contact forces in addition to fluid interactions [30, 31, 32]. The role of contact interactions has been extensively studied in simple models of active matter systems such as self-propelled rods and particles [157, 158, 159, 160]. However, when locomotion is governed by an undulatory motion the interactions between these self-propelled systems may be influenced by phase differences in undulatory gait. In this work we study how the relationship between spatial configuration and undulatory gait parameters influence the collective behavior of active undulatory systems.

Before introducing active undulatory systems we briefly review the physical phenomena of active-matter and in particular of self-propelled particles. A self-propelled particle is an agent that possesses an internal energy reservoir which can produce propulsion (see Ref. [161] for an

extensive review). Groups of these particles can then interact through hydrodynamic, short- and long-range potential, or contact forces and display collective behavior such as flocking, swarming, and incoherent motion. Interactions through contact have been extensively studied in these systems and often lead to positional and velocity alignment [159, 162, 163]. In most examinations of the collective physics of self-propelled particles the agents themselves are propelled through constant, time-invariant propulsion. Steering forces may vary with the environment [164, 42, 165] or the other agents' positions (as in the classic Vicsek model [166]), but still typically the propulsion is slowly modulated or constant. Furthermore, the "body" shape of these particles are typically simple spheres, rods, or ellipsoids, that have no articulating components (i.e. are a single rigid body). This simplification while useful for analysis and simulation is a drastic reduction of the complexity seen in living systems that often locomote through articulated body and appendage motion.

In this work we define an active undulatory system as consisting of individuals that move through body (or discrete joint) bending in which bending is propagated along the length of the body. Undulatory locomotion is a common method of movement in biological systems across scales from sperm [167] to snakes [89, 168, 169]. Undulatory body bending can be three-dimensional with out-of-plane body movement such as snake sidewinding [63], however, in this work we consider planar undulatory movement. A representative undulatory gait is a simple traveling wave of body bending, $y(x,t) = A\sin(\frac{2\pi x}{\lambda} + \omega t + \phi)$ that propagates from head to tail. The undulatory movement occurs through movement in the lateral direction, y, that propagates at wavespeed $\lambda\omega$ and with wavelength λ and frequency ω. However, when considering the undulatory motion of more than one individual, an additional phase parameter ϕ becomes necessary to describe the relative phases between the two systems. When swimmers have identical phases they will be in synchrony, however, when phases differ the traveling wave propagation will spatiotemporally differ which might result in forceful interactions between individuals.

The simplest system that can exhibit undulatory, traveling-wave motion is the "three-

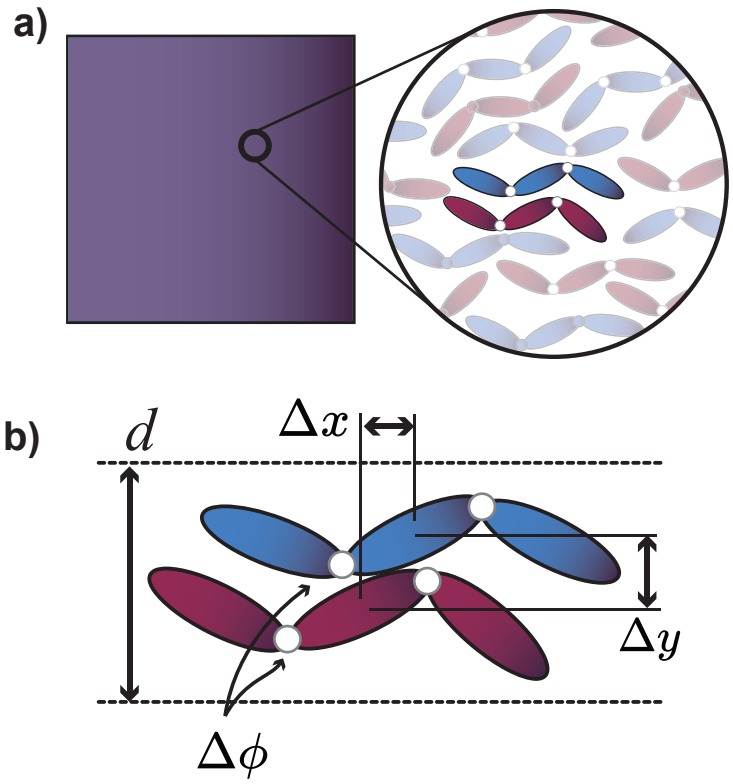

Figure 4.1. Motivation and overview of gait compatibility among undulatory swimmers. a) Large groups of swimmers experience contact interactions. b) Contact interactions among pairs of undulatory swimmers confined to a lateral distance d require planar $(\Delta x, \Delta y)$ reconfiguration when there is a gait phase difference $\Delta\phi$.

link swimmer" (Fig. 4.1). This system consists of three rigid links separated by two actively controlled joints. The three-link swimmer was first introduced by Purcell in his study of low Reynolds number locomotion [170] and later analyzed in Becker et. al. in which the full dynamical equations were introduced [171]. In the many years since its introduction the three-link swimmer has been studied extensively as a model of undulatory locomotion on frictional surfaces [172, 173], granular material [174], and within fluids [175, 176]. Undulatory locomotion in a three-link swimmer is generated through oscillatory motion of the two joints, whose angles $[\beta_1, \beta_2]$ define a "shape-space" of the system [177]. A gait is defined as a closed trajectory through this shape-space over a period of time T such that $\beta_i(t) = \beta_i(t+T)$.

Active undulatory systems have been studied in the context of agent-environment in-

teractions such as collision with environmental features. Undulatory robots interacting with posts display scattering phenomena that highlight the importance of *active collisions* between active systems and the environment [178]. These authors define active collisions as mechanical contact in which propulsive forces within the robot or animal create persistent contacts with environmental features. These active collisions yield relationships between the incoming and outgoing trajectory, dependent upon the undulatory phase and collision position. Similarly microscale swimming bacteria that locomote through reciprocal flagellar movement interact with patterned and flat walls through predictable scattering [179]. The contact interactions between flagella and the wall redirect the swimmers and the gait-phase at contact governs this scattering behavior. At a larger scale swimming nematodes (*C. elegans*) make repeated body contact with obstacles when swimming through wet granular material [180] and arrays of fixed pillars [181]. The influence of these obstructions causes the animals to change gait and to generate slower forward velocity. This previous work highlights how undulatory movement is influenced and affected by interactions with the external environment. In particular the importance of gait phase at collision suggests that the phase differences *between* two undulatory swimmers will play an important role in the collective physics of these systems.

This work is inspired by recent observations of collective undulatory swimming in nematodes [182], vinegar worms [183, 184], and sperm. These undulatory swimmers often form clusters of high-density swimmers [30, 185], and the close proximity between individuals can generate forceful interactions through hydrodynamics and contact. Hydrodynamic interactions between microscale undulatory swimmers have been well studied (see Ref. [31] for an extensive review). Interactions through a fluid can lead to long and short-range forces that drive spatial clustering [32, 186] and synchronization phenomena [187, 188, 33, 189, 190]. When organisms increase in size the role of hydrodynamic interactions is diminished, yet individuals may still interact through contact. Recent experiments with vinegar worms [183, 184] and nematodes [182] demonstrate that contact interactions can generate synchronization of the undulatory gait. More broadly, contact interactions between undulatory systems can generate coherent and

incoherent movement dependent on density, gait, and actuation parameters [40, 191, 192].

In the following work we study the planar dynamics of undulatory swimmers in close proximity to determine the role of gait phase difference. In experiments we study the relative planar positioning of robot "swimmers" in which the individual swimmers do not "swim" but instead rest on a frictional surface. In simulations we studied swimmer groups that did swim through viscous forces acting on them. In both robot experiments and numerical simulation we find that as the phase difference between swimmers increases there is an increasing interaction "force" along the longitudinal direction that pushes swimmers to a stable planar configuration. This stable configuration is determined by the planar arrangement and phase difference and is called the compatibility condition for undulatory motion. In the subsequent work we demonstrate that compatibility governs the packing arrangements of undulatory swimmers, and when swimmers are pushed out of compatibility their contact interactions attempt to drive them back to compatibility. Ultimately this work highlights the importance of contact interactions and critically gait phase on the collective behavior of active undulatory systems.

This chapter is organized through a series of robophysical experiments and numerical simulation. In Sec. 4.2 we provide details for the robot experiments and numerical simulation. The first observations are made with pairs of undulatory robots in Sec. 4.3.1 where we demonstrate that phase differences between undulatory robots lead to longitudinal repositioning of the robots. The details of the phase and spatial dynamics depend on actuation waveform which is studied in experiment and simulation. From these experiments we develop a model in Sec. 4.3.2 of spatial configurations that depend on gait which we call *gait compatibility*. The gait compatibility model is based on an assumption of a smooth, sinusoidal body shape that differs from the three-link robots studied in experiment and simulation and thus we next study the role of body shape on compatibility (Sec. 4.3.3). We next study groups of three and four robots to observe spatial dynamics in these collectives (Sec. 4.3.4). The robot group experiments and the compatibility model suggest a packing density limitation with groups of swimmers at different phases which is investigated in Sec. 4.3.5. Lastly, in numerical simulation we observe

the basins of attraction of compatible configurations (Sec. 4.3.6) and we measure the "potential energy" of these stable configurations (Sec. 4.3.7). This combination of robot experiments and numerical simulation reveal that undulatory phase differences have a significant influence on spatial configurations within undulatory active systems.

4.2 Methods

We performed robot experiments and numerical simulations to model the collective behavior of undulatory "swimmers" that have rigid links coupled through rotational joints. We studied the behavior of two and up to ten robots through experiment and simulation (Fig. 4.2).

4.2.1 Robotics experiments

The robot experiment set-up was designed to observe the collision interactions between two to four swimmers. Each swimmer in an experiment was comprised of a three-link robot (Fig. 4.2). Each robot had a three-dimensional (3D) printed body connected with two Dynamixel AX-12A servo motors (Fig. 4.2a) with a total length, $L = 51$ cm. All servo motors were programmed to oscillate with a sine function of constant amplitude and constant frequency (0.5 Hz). The servo motors were commanded to follow an angular trajectory that was controlled with a proportional controller and a maximum torque of 1.5 Nm. To produce an undulatory motion,

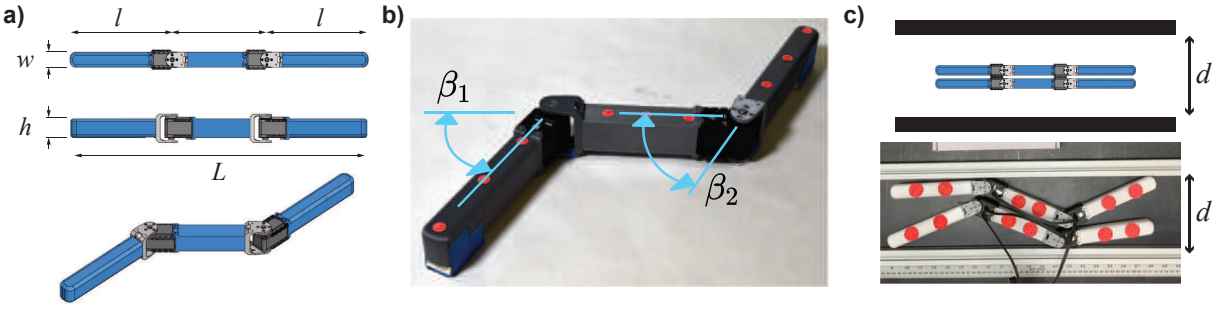

Figure 4.2. Overview of three-link robots. a) Geometry of the three-link system. Links are length, $l = 17$ cm, height, $h = 5$ cm, and width, $w = 2.5$ cm. b) The joint angles, β_1 and β_2 are controlled through position-commanded servos. c) We studied groups of robots in a narrow channel of variable width d.

we generated a traveling wave along the length of the body with angular position of the i^{th} joint on the j^{th} robot as

$$\beta_i^j = \beta_0 \sin\left(\frac{2\pi\xi i}{N} - 2\pi f t + \phi_j\right) \tag{4.1}$$

where $i = \{1,2\}$ denotes the joint number and $N = 3$ for the three links of the robot (Fig. 4.2b). $j = \{1,2,3,...\}$ denotes different robots. The ratio $\xi = \frac{L}{\lambda}$ is the number of wavelengths along the body. In our experiments we varied $\xi = [0, \frac{3}{4}, 1, \frac{3}{2}]$. The angular amplitude, β_0, was held constant at $\beta_0 = 45^\circ$ in experiment and $\beta_0 = 40^\circ$ in simulation. We conducted a set of sensitivity analyses of the actuation parameters such as motor angular amplitude β_0, motor controller proportional gain K_P, and swimmer body length L, in simulation. The results were consistent across a large variation of these parameter values. The phase offset ϕ_j is constant for each robot, but could differ between robots, and represents the overall actuation phase of the robot. Thus the phase difference between robots is represented by $\Delta\phi = \phi_a - \phi_b$.

The goal of this chapter is to study the spatial dynamics of undulatory swimmer groups as they swim in the same direction (Fig. 4.1a). We emulated the effect of being within a group by confining the robots to a narrow channel so that they are forced to interact with each other. When the confining wall is not in place the robots will push each other away until they no longer contact and interact. The confined environment was created using a fixed channel measuring (slightly more than) one meter long and 13 cm wide (Fig. 4.2c). The robots rested on a frictional surface and were confined laterally by two rigid walls whose separation distance, d, was varied depending on the number of robots in the experiment. When robot pairs or groups are in the channel they are able to move laterally (Δy) and longitudinally (Δx) with respect to each other through contact. Δx and Δy were measured as the planar distance between the middle of the central links between each robot. Because of the constraint of the narrow channel, the rotation of robots was ignored. Each experiment consisted of placing the robots laterally in contact ($\Delta y = 1.5$ cm) and at the same longitudinal position ($\Delta x = 0$). Video recording of the robot

movements was captured from an overhead view. A meter stick was aligned along the channel's length to measure the robot locations measured at each robot's center. At the start of each experiment, the two robots were set to their elongated shape, with joint angles $\beta_i^j = 0$.

Through video tracking we measured the center position of all robots in the experiment. We compute the center-to-center spacing between nearest neighbors to determine the lateral and longitudinal spatial shifts that occur during undulatory movement. The motors were commanded to generate an undulatory gait for 15 oscillations (30 seconds). In robot pairs this process was repeated for the varying phase shift in the two robot experiments, $\Delta\phi$, at values $[-1,\ -0.75,\ -0.5,\ -0.25,\ 0,\ 0.25,\ 0.5,\ 0.75,\ 1]\pi$. Phase shift in three robot experiments was set at values $[-1,\ -0.5,\ 0,\ 0.5,\ 1]\pi$. For the four robot tests the phase shifts were selected at random. We additionally performed this measurement for varying wavelengths.

The robots did not have wheels or any other frictional anisotropy and thus they do not "locomote" along a particular direction but rather undergo continuous traveling wave oscillation while approximately remaining in the same spatial location. While the robots do not swim in experiment, our focus in this chapter is the influence of contact interactions on the relative spatial positioning between undulatory swimmers. In simulations we implemented viscous drag forces on the swimmers to make them swim forward emulating being in a low Reynolds number environment. We found good agreement between the experiment and simulation. Thus, despite the robots not swimming through a fluid we believe their contact interactions are commensurate with those of the swimming systems that inspired this work.

4.2.2 Simulation details

We performed simulations of undulatory swimmer groups to compare with experiment and to extend analysis of this system beyond what is experimentally feasible. The system was studied in the Project Chrono multibody physics simulation environment [193]. In simulation the swimmers interacted through contact normal forces. Contact interactions in Chrono are modeled using a discrete element method (DEM) framework. Chrono handles two forms of

DEM, one in which only "rigid" interactions occur which are handled through complementarity conditions that enforce nonpenetration between bodies (DEM-C). The second method, DEM-P, models "soft" interactions and uses a penalty based method modeling contacts as overlapping elastic bodies with elastic interactions. In our simulations we use the DEM-C method to handle contacts. The DEM-C and DEM-P methods have been compared in Pazouki et. al. [194] in addition to validation comparisons. Details of the DEM-C method in Chrono are described in the appendix B and can be found in Pazouki et. al. [194], Heyn et. al. [195], and Tasora et. al. [193]. In Chrono the swimmer links are modeled by rectangular collision shapes for collision detection. We set the tangential friction to zero and normal coefficient of restitution to zero in the simulations.

Viscous drag forces were applied to swimmer links to emulate the swimmers moving in a low Reynolds number environment [196]. The drag forces applied to the moving swimmer links are provided in the appendix. We modeled the position controlled servos in simulation through torque actuation of the joints under a proportional position control (P gain = 0.15 Nm/rad) with torque saturation to model the maximum torque capabilities of the motors. The torque saturation in simulation was set to the same saturation of the experiment motors, 1.5 Nm. The motors were commanded to follow the trajectories defined in Equation 4.1. We primarily studied groups of 3-link swimmers consistent with experiment. However, we did perform simulations with five-link, seven-link, and nine-link swimmers to understand how link number influenced spatial dynamics.

4.3 Results and discussion

4.3.1 Spatial reconfiguration between robot pairs

We begin our investigation by studying pairs of robots in experiment and simulation. We set the channel width to $d = 13$ cm to constrain the robots laterally and we perform experiments with a phase difference between the two robots of $\Delta\phi = \phi_1 - \phi_2$ over the range of $\Delta\phi \in [-\pi, \pi]$.

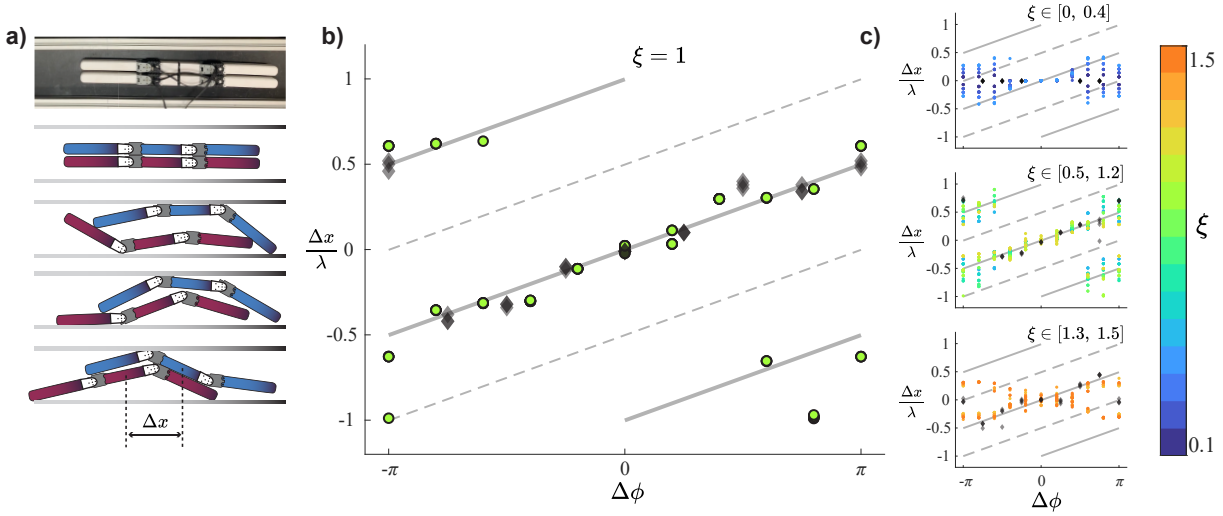

Figure 4.3. Gait compatibility in undulatory swimmer pairs. a) Image of two undulatory robot swimmers in experiment and illustration of longitudinal motion from contact interactions. Illustrations are traced from experiment images. b) Steady-state longitudinal separation versus phase difference between robot pairs with $\xi = 1$. Black diamonds are experimental results; green dots are simulation results. Solid lines are compatibility predictions from equation 4.2. c) The right column shows the simulation results with different ξ at three ranges. Experiment results with $\xi = [0, \frac{3}{4}, \frac{3}{2}]$ are included accordingly. The solid lines are the compatibility prediction.

We observe that robots with nonzero $\Delta\phi$ experience a longitudinal displacement, Δx, driven by the contact interactions (Fig. 4.3a and b). The longitudinal separation, Δx, was measured by averaging the position difference of the robot centers in the last five periods where the robots have reached a steady-state value for longitudinal spacing.

In the $\xi = 1$ experiments a phase difference between the two robots resulted in a change in the steady-state longitudinal separation with an approximately linear relationship (Fig. 4.3b). The slope of the $\frac{\Delta x}{\lambda}$ versus $\Delta\phi$ relationship was the same over different number of traveling waves along the body between $\xi = [\frac{3}{4}, 1, \frac{3}{2}]$ (Fig. 4.3b and c). However, when ξ was relatively large or small we observed that deviation from this linear relationship (Fig. 4.3c, top and bottom panels). Numerical simulations of two swimmers in a viscous fluid with identical geometries agreed well with the experiment.

4.3.2 A gait compatibility model for undulatory collectives

We hypothesize that undualatory swimmers actuated through a sinusoidal traveling wave adjust their planar positioning to minimize contact interactions. We now derive a geometric relationship between phase and planar configuration based on the assumption of minimizing contact. We assume that the undulating motion of the three-link swimmer is represented by a sinusoidal traveling wave of amplitude, A and wavelength, λ, and that there is no lateral separation between the swimmers ($\Delta y = 0$; we will relax this assumption later). In the continuum limit the lateral position of each swimmer is thus described by,

$$y_1(x,t) = A\sin\left(2\pi\frac{x}{\lambda} + \omega t\right)$$
$$y_2(x,t) = A\sin\left(2\pi\frac{(x-\Delta x)}{\lambda} + \omega t + \Delta\phi\right)$$

We propose that an equilibrium configuration of undulatory swimmers occurs when the two sinusoidal curves make tangential contact (i.e. they are just close enough to touch but do not intersect) which is shown in Fig. 4.4a). For the case of no lateral separation this imposes the single constraint, $y_1(x,t) = y_2(x,t)$, which can be satisfied by a relative longitudinal displacement between the two swimmers by an amount

$$\Delta x = \frac{\lambda}{2\pi}\Delta\phi \tag{4.2}$$

We call this condition the compatibility condition for undulatory swimmers, inspired by recent experiments on swimming worms which introduced the term gait compatibility [182].

We plot the gait compatibility prediction along with the experiment and simulation measurements in Figure 4.3b and c for the swimmer pairs. We find good agreement with the model prediction when the number of wavelengths along the body, ξ, is close to 1. However, as discussed in the previous section the observations from experiment and simulation differ for large and small ξ. The gait compatibility model suggests that oscillatory swimmers with

traveling wave actuation can swim in close proximity by adjustments to their longitudinal position according to their phase difference. When ξ is small but non-zero the swimmer length is substantially smaller than the commanded wavelength. In this case deviations from compatibility can occur because the contact location predicted from sinusoidal curves is outside the range of the finite body length of the swimmers. Thus, in theory they would interact but in actuality with small ξ the interaction may not occur. Alternatively, when ξ is large there are multiple wavelengths along the swimmer. Using a finite number of links to represent multiple wavelengths will cause aliasing problems as ξ increases which can cause poor sinusoidal curve tracking and thus deviation from the compatibility condition. This suggests the importance of traveling wave actuation which acts to couple the lateral contact with longitudinal reconfiguration. In effect the traveling wave actuation can force neighboring swimmers along the longitudinal axis and drive them into appropriate compatible states determined by phase and planar spacing. We chose $\xi = 1$ in rest of the simulations demonstrated in this work.

In deriving Equation 4.2 we did not consider the influence of a lateral separation distance, Δy, on the allowable phase and longitudinal offsets in which compatibility is achieved. However, in larger groups contact interactions may lead to density fluctuations [197]. These density fluctuations may increase the range of compatible $\Delta\phi$. Here we now derive the full compatibility relationship that governs the allowable lateral, longitudinal, and phase offsets for two compatible sinusoidal gaits.

We again assume two swimmers oscillating as spatial sinusoidal waves and we now include the longitudinal (Δx), phase ($\Delta\phi$), and lateral (Δy) offsets

$$y_1(x,t) = A\sin\left(2\pi\frac{x}{\lambda} + \omega t\right) \tag{4.3}$$

$$y_2(x,t) = A\sin\left(2\pi\frac{(x-\Delta x)}{\lambda} + \omega t + \Delta\phi\right) + \Delta y \tag{4.4}$$

We assume that $\Delta y > 0$ and thus swimmers that are in compatibility satisfy the equation $y_1(x,t) \leq y_2(x,t)$ (Fig. 4.4a). However, the boundaries of the compatible states occur when two sinusoidal

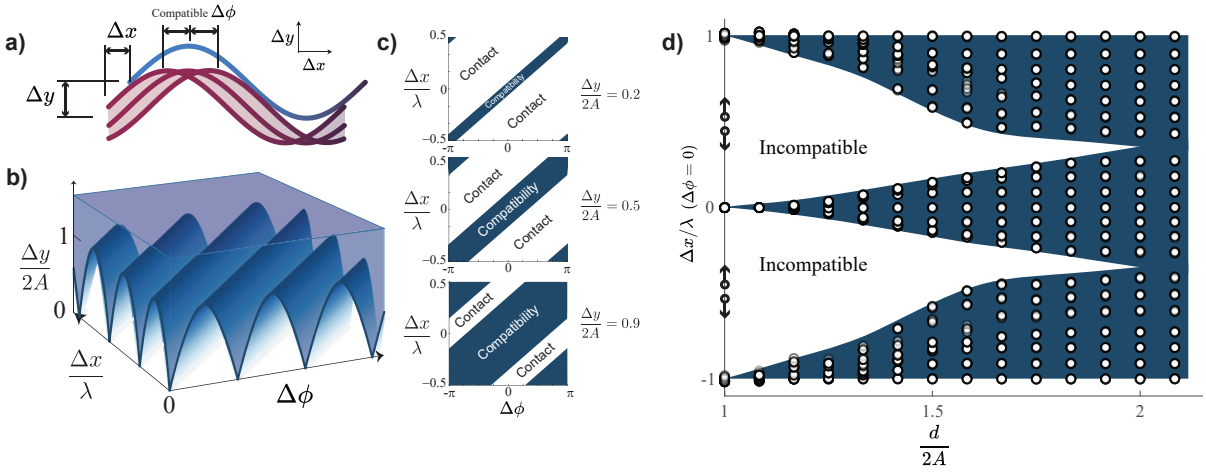

Figure 4.4. Contact compatibility criteria. a) An overview of the phase-range ($\Delta\phi$) for compatible sinusoidal curves that are separated by a Δx and Δy displacement. b) The three-dimensional representation of the compatibility criteria represented by equation 4.5. The shaded region above the solid blue curves are allowable configurations of gait compatibility. As the lateral separation distance increases (vertical axis, $\frac{\Delta y}{2A}$) the range of compatible phases increases. c) We show cross sections of the compatibility condition at three different lateral separations: $\frac{\Delta y}{2A} = [0.2, 0.5, 0.9]$ from top to bottom. When $\frac{\Delta y}{2A} > 1$ any combination of $\Delta\phi$ and Δx will be in compatibility. d) Dots indicate the steady-state longitudinal separation between two three-link swimmers in simulation with $\Delta\phi = 0$ as a function of wall width. The shaded area is drawn to guide the eye and represents the growing compatibility region as lateral spacing is allowed to increase.

curves make tangential contact, which imposes the following two constraints, $y_1(x^*,t) = y_2(x^*,t)$, and $y_1'(x^*,t) = y_2'(x^*,t)$ where prime denotes derivative with respect to x, and x^* is the contact location. Solving this equation for the allowable phase offsets between neighboring swimmers yields the following inequality relationship

$$|\Delta\phi - \frac{2\pi}{\lambda}\Delta x| \leq 2\left|\arcsin\left(\frac{\Delta y}{2A}\right)\right| \tag{4.5}$$

When $\Delta y = 0$ this yields the previous equality in Eqn. 4.2 between Δx and $\Delta\phi$. However, as Δy increases there is a growing range of allowable phase offsets in which two undulatory swimmers can be in gait compatibility and not make contact (Fig. 4.4a).

We show samples of the compatibility condition for varying ranges of lateral separation in Fig. 4.4b,c which highlights the growing region of compatible phase and longitudinal separation

as lateral distance increases. The gait compatibility described here is somewhat similar to the hydrodynamic synchronization of infinite two-dimensional undulating sheets studied by Elfring and Lauga [198]. In that work, the two sheets could freely displace longitudinally through fluid force interactions and the authors demonstrated that the sheets always converged to a relative in-phase or antiphase configuration depending on waveform. However, there is a critical difference between this work and the case of systems that interact through hydrodynamic forces. When two swimmers are within gait compatibility, they do not contact each other and thus are entirely decoupled. Small perturbations to their position or phase, as long as they are not pushed out of compatibility (and thus into contact), will persist, indicating that the compatibility state is a neutrally stable configuration. The interaction through contact means that there is a discontinuity at the boundary between states where the swimmers can interact, and states where they cannot interact.

To observe how the compatibility states change when the swimmer separation distance is increased we performed simulations for $\Delta\phi = 0$ with initial conditions ranging from $\frac{\Delta x}{\lambda} \in [-1, 1]$. We observed the final longitudinal separation distance as a function of the initial conditions and confinement. We normalize the confinement wall distance, d, by the peak-to-peak oscillatory amplitude of the undulatory body wave such that when $\frac{d}{2A} > 2$ swimmers through initial contact can push each other away and out of compatibility without the wall confinement to bring them back into contact. In theory, confinement distances $\frac{d}{2A} < 1$ are not possible because the undulatory gait is obstructed. Increasing the confinement wall distance increased the range of final longitudinal spacing observed between two swimmers (Fig. 4.4d). The central compatibility state broadened indicating that swimmers could compatibly move within a range of longitudinal separations without contact. This is in accord with the predictions from the compatibility model (Eqn. 4.5) in which non-zero lateral separations ($\Delta y > 0$) allow for a range of solutions to the compatibility conditions. In practice there will always be lateral spacing in active assemblies and this highlights a novel aspect of contact-mediated interactions because once in the compatible state the swimmers no longer can interact until pushed back out of compatibility.

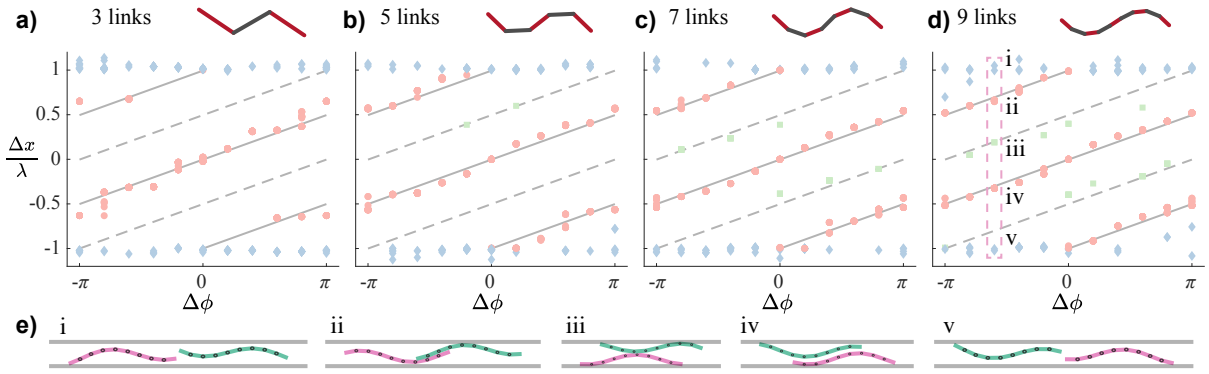

Figure 4.5. Gait compatibility simulations of two swimmers with 3, 5, 7, or 9 links from left to right (a-d). As the link number increases the longitudinal separation versus phase difference (red circles) show good agreement with the compatibility prediction (solid-lines). e) Bottom figures i-v show example configurations of two 9-link swimmers. Red circles represent swimmer pairs that reached the compatibility condition (ii, iv); blue diamonds represent swimmer pairs that separate longitudinally with each other (i, v), green squares represent swimmer pairs that are jammed with each other(iii).

4.3.3 Increasing link number yields better agreement with compatibility model

In both experiment and simulation we noticed that the relative equilibrium of the longitudinal spacing, Δx formed discrete clusters along the compatibility prediction line while the prediction from a sinusoidal model is a linear phase-displacement relationship. We hypothesized that this model error was the result of the poor approximation of a sinusoidal shape by the three-link system. To determine how link number influenced compatibility we studied five-, seven-, and nine-link swimmer pairs in simulation and we found that increasing the linkage number produced an increasingly linear compatibility relationship with increasing link number (Fig. 4.5). The root mean square (rms) error of the simulation compatibility separation and the prediction (Eqn. 4.2) decreased with increasing link number (rms error from compatibility condition $= [0.084, 0.063, 0.044, 0.039]$ for the $[3, 5, 7, 9]$ link swimmers, respectively). The decreasing error with increasing link number is a result of the discretized body-shape in the three-link swimmers. The compatibility model assumes a perfectly sinusoidal body shape, however, with only three-links the body undulation is not quite sinusoidal. However, as we add

more links this assumption becomes better so does the gait compatibility model.

4.3.4 Experiments with three and four robot pairs

To examine how larger groups of undulatory swimmers arrange spatially we performed experiments with groups of three and four robots (Fig. 4.6a). We widened the channel to $d = 19$ & 22 cm for three and four robot experiments and set $\xi = 1$. The robots are initialized with $\Delta x = 0$ and all joint angles set to zero. We begin undulatory actuation for the robots and we monitor the lateral and longitudinal displacement from an overhead camera (Fig. 4.6a). We observed the same overall behavior in robot groups as in robot pairs: phase differences between neighboring robots resulted in longitudinal repositioning until the group reached an overall steady-state spatial configuration. Examining the nearest neighbor $\Delta x_{i,i+1}$ versus $\Delta\phi_{i,i+1}$ we observe reasonably good agreement with the compatibility predictions (Fig. 4.6b). However, in both the three and four robot groups we do observe relationships of $\frac{\Delta x}{\lambda}$ vs $\Delta\phi$ that lie in between the compatibility states (dashed line in Fig. 4.6b). Visual inspection of these experiments suggests that these data points represent configurations that are effectively "stuck" in between the two compatible configurations. In states lying along the dashed line it requires an equidistant longitudinal shift in either the positive or negative to reach compatibility and thus this the interactions that drive the robots to compatibility may conflict along this line and cause them to remain stuck. These dynamics will be explored further in Section 4.3.6.

The variation in the longitudinal position was larger in the group experiments compared with the robot pair experiments suggesting potential collective effects present in the three and four robot experiments that were not captured in the pair experiments. The principal influence of this variance from the compatibility prediction is the larger lateral spacing afforded to the larger robot groups. As the swimmers push each other they may arrange into high and low density configurations leaving lateral space for some robots, which thus increases the range of compatible phases allowable (Eqn. 4.5). We will explore how density influences phase variance in the next section.

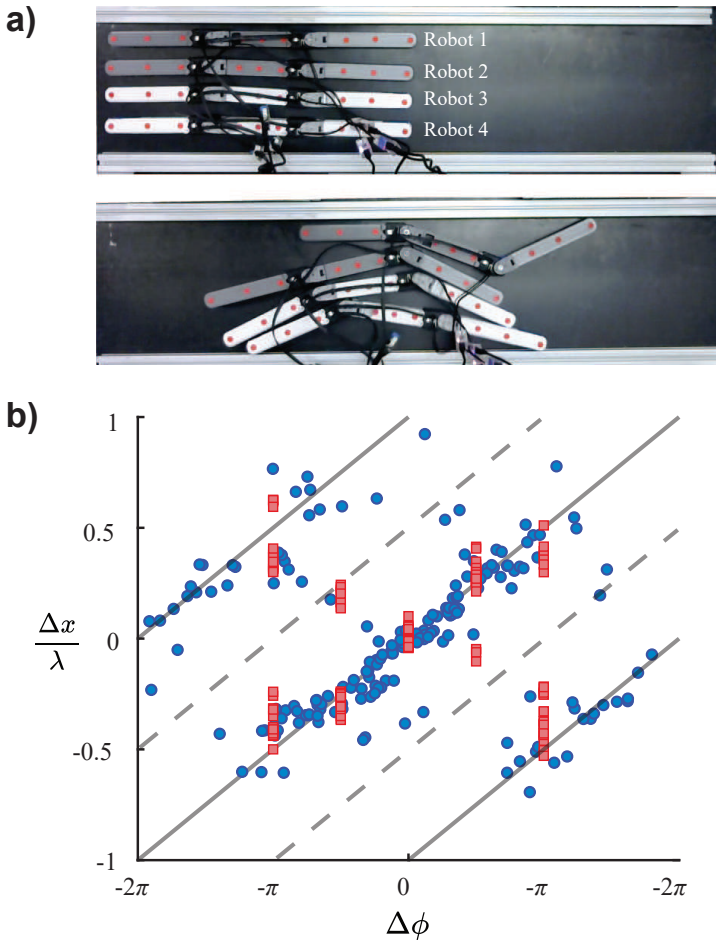

Figure 4.6. Gait compatibility in larger robot groups. a) Image of a four robot experiment at the beginning (top) and in the middle of the experiment (bottom). b) Steady-state longitudinal separation versus phase difference groups experiments with three (red squares) and four robots (blue circles). Solid lines are compatibility predictions from equation 4.2.

4.3.5 Gait compatibility influences spatial packing

Contact interactions among the collective undulatory swimmers drive them into compatible configurations. However, the range of available compatible configurations increases as the lateral spacing increases and thus we expect that the group density will influence the allowable phase and spatial variance in groups. To address this question we studied the packing configurations of large groups of three-link swimmers in simulation to determine the relationship between group phase variance and packing density. We used a short channel to confine the swimmers longitudinally by a distance of $1.1L$ constraining the ability to longitudinally reconfigure. We

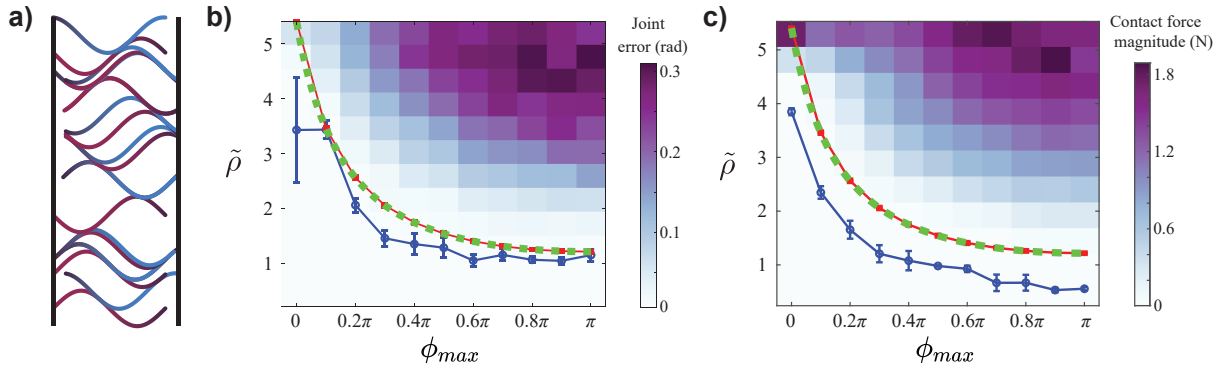

Figure 4.7. Lateral density is influenced by phase variance in undulatory groups. a) A representation of a group of undulatory swimmers separated laterally (the vertical direction) in tangent contact with phase variation. b) A heatmap of time averaged absolute value of joint error induced through collisions within a swimmer group for varying normalized lateral density, $\tilde{\rho}$ (y-axis) and the range of phase variation (x-axis). Blue circles indicate the measured joint error threshold below which contact typically does not occur in the group from simulations. Error bars represent the standard deviation of the mean taken over five-periods. c) A heatmap of time averaged magnitude of contact forces induced through collisions within a swimmer group. Blue circles indicate the baseline contact force threshold between a swimmer and the wall. Error bars represent the standard deviation of the mean taken over five-periods. In both b) and c): The red curve is a Monte-Carlo estimate based off of the compatibility equation. The dashed green curve is the calculation from the math model Eqn. 4.10.

initialized 50 three-link swimmers within a channel of fixed lateral width (Fig. 4.7a) and we measured the spatial positioning, and the deflection of the rotational joints from their commanded trajectory (joint error). The swimmers were all oriented along the direction of the channel length so that they only interacted through lateral collisions and their orientations were approximately the same. We varied the lateral confinement distance and the range of gait phases to observe how spatial and phase variance influences the packing and contact interactions between groups of undulatory swimmers.

We characterized contact interactions between swimmers by monitoring both the joint error, and the contact forces. The joint error is linearly proportional to the joint torque in the joint control system, and thus this is a metric of contact interactions between swimmers. Since joint error varies from positive to negative through an oscillation cycle we take the absolute value of all joint errors and time average over five periods. When the swimmers are not in contact the

joint error is approximately zero (viscous drag causes the error to never reach zero). However, when the lateral density is increased the swimmers begin contacting each other and causing the joints to deviate from their assigned motion. We examine the influence of phase-range and lateral density on the packing behavior of the swimmers (Fig. 4.7b). For a fixed density, increasing the phase-range resulted in an increase in the overall joint error of the swimmers in the group indicating collisions and non-compatible space-phase relationships. Similarly, for a fixed phase-range increasing the density caused an increase in joint error.

We characterized the compatibility threshold in simulations by determining for each phase-range and density combination whether the mean joint-error was above that of an individual swimmer (threshold of 0.01 rad.). The compatibility threshold from simulations is shown in blue circles in Figure 4.7b, where error bars are the result of 5 replicate simulations. As the lateral density or the phase-range increases the mean joint error increased. The threshold curve from direct simulations appears to follow an inverse relationship between lateral density and phase-range.

In addition to measuring joint error we also measured the average contact forces between swimmers in numerical simulations. We averaged the contact forces across all swimmers over five periods of oscillation to determine how large the contact interactions are. Similar to the joint error (Fig. 4.7b) we observe that as density and phase variation increase so does the average contact force between swimmers (Fig. 4.7c).

To investigate the relationship between gait phase variance and the lateral packing density we now model the swimmers as single-period sinusoidal curves (i.e. $\xi = 1$). We first analyzed this system through a Monte-Carlo (MC) approach to estimate the phase-density threshold curve. The MC method consisted of the following steps: 1) Draw 3000 random samples phases, ϕ_i, from a uniform distribution between 0 and ϕ_{max}. 2) Set the first sinusoid at $y_1(x) = \sin(x + \phi_1)$. 3) Determine the required Δy_2 so that y_1 and sinusoid $y_2(x) = \sin(x + \phi_2) + \Delta y_2$ make tangent contact (i.e. are as closely spaced in y-direction as possible without overlap). Δy_2 is the neutral lateral position of sinusoid y_2. 4) Repeat the previous step for all remaining swimmers with

phases from the 3000 randomly drawn list. 5) The total lateral space occupied by the group is Δy_{3000}. The lateral packing density is given as, $\tilde{\rho} = \frac{N}{\Delta y_{3000}}$. We repeated the whole process above 100 times to estimate the $\rho(\phi_{max})$ curve reported in Figs. 4.7 b and c. For example, Fig. 4.7a provides a snapshot of a group of sinusoidal swimmers whose phases were randomly selected between $[0,\ \phi_{max}]$ and are in perfect tangent contact. In Figs. 4.7b and c we plot the MC estimate of $\tilde{\rho}$ shown as the red curve. The MC estimate shows qualitative agreement with the estimated threshold from the three-link simulations.

Lastly, we perform a direct analysis of the phase-density relationship of sinusoidal curves to exactly compute the compatibility packing threshold. We assume a group of sinusoidal curves with random, uniform phase distribution in the range $\phi_i \sim U(0,\ \phi_{max})$. We set $\Delta x = 0$ in Equation 4.5 and rearrange to the following

$$\frac{\Delta y}{2A} = \sin\left(\frac{\Delta\phi}{2}\right) \tag{4.6}$$

For a swimmer group with phases drawn at random from the uniform distribution $\phi_i \sim U(0,\ \phi_{max})$ the expected swimmer separation in the y direction can be derived from Equation 4.6

$$\begin{aligned}\sum_{i=1}^{N} \frac{|\Delta y_i|}{2AN} &= \frac{1}{N}\sum_{i=1}^{N}\left|\sin\left(\frac{\Delta\phi_i}{2}\right)\right| \\ &= \int_{-\phi_{max}}^{\phi_{max}} \left|\sin\left(\frac{s}{2}\right)\right| f_{pdf}(s)\, ds\end{aligned} \tag{4.7}$$

where $s = \Delta\phi$ and $f_{pdf}(s)$ is the probability distribution of the phase difference. Since $\phi_i \sim U(0,\ \phi_{max})$, $\Delta\phi$ follows a triangle distribution between $[-\phi_{max},\ \phi_{max}]$ which is symmetric about

the y axis.

$$\begin{aligned}\frac{\tilde{y}}{2A} &= \int_{-\phi_{max}}^{\phi_{max}} \left|\sin\left(\frac{s}{2}\right)\right| f_{pdf}(s)\, ds \\ &= 2\int_{0}^{\phi_{max}} \left|\sin\left(\frac{s}{2}\right)\right| \left(\frac{1}{\phi_{max}} - \frac{1}{\phi_{max}^2}s\right) ds \\ &= \frac{4}{\phi_{max}} - \frac{8\sin\left(\frac{\phi_{max}}{2}\right)}{\phi_{max}^2} \\ &= \frac{4}{\phi_{max}^2}\left(\phi_{max} - 2\sin\left(\frac{\phi_{max}}{2}\right)\right) \end{aligned} \tag{4.8}$$

We now calculate the expected lateral distance (Y) required for a group of N swimmers, considering the swimmer body width w

$$\begin{aligned} Y &= N\tilde{y} + Nw \\ &= \frac{8AN}{\phi_{max}^2}\left(\phi_{max} - 2\sin\left(\frac{\phi_{max}}{2}\right)\right) + Nw \end{aligned} \tag{4.9}$$

Thus the expected lateral density with all swimmers in compatibility is $\rho = N/Y$ and the density normalized by the peak-to-peak oscillatory amplitude is given by $\tilde{\rho} = 2AN/Y$ which yields

$$\tilde{\rho} = \frac{\phi_{max}^2}{\frac{w}{2A}\phi_{max}^2 + 4\phi_{max} - 8\sin(\frac{\phi_{max}}{2})} \tag{4.10}$$

We see in Figure 4.7b, c that the expected value calculation agrees extremely well with the Monte-Carlo simulation. Furthermore, we can examine the extremes of the density variation and their effect on packing density. When $\phi_{max} = 0$ the non-normalized density becomes $\rho = \frac{1}{w}$ which corresponds to the maximum packing density of the swimmers in contact with each other. Overall we find that as the phase variation within a swimming group increases the required lateral density within the group must decrease or else swimmers will collide with each other. This relationship provides compelling motivation for animal and engineered swarms of swimming agents to synchronize their gaits to achieve higher density groups.

4.3.6 Compatible configurations have a broad basin of attraction

Swimmers in non-compatible configurations are pushed into compatibility through contact interactions. In the idealized situation in which swimmers are represented by sinusoidal body position the compatible configuration is a relative equilibrium where contact no longer occurs. In this section we study how the initial longitudinal separation, Δx, and phase detuning, $\Delta\phi$, influence the final state reached by the pair of undulatory swimmers. We study this for the case of close proximity with wall separation $d = 13$ cm where contact interactions are reinforced by the close proximity (i.e. swimmers cannot push each other away laterally).

In a first example we study the spatial evolution of five different initial conditions of longitudinal separation, Δx_0 (Fig. 4.8a). The phases are the same for these swimmers ($\Delta\phi = 0$) and so the compatible configuration is $\Delta x = 0$. Initial separation distances that are far away from the compatible separation ($|\Delta x_0| > 0.3$) are pushed away from the $\Delta x = 0$ compatible configuration as the swimmers repel each other along the longitudinal axis. However, when the initial separation distances are closer (approximately $|\Delta x_0| \leq 0.3$) the swimmers experience an effective attractive interaction force in the longitudinal direction and ultimately end in the compatible state for their phase difference.

We study the evolution of longitudinal separation across the full range of relevant initial separation and phase differences. From each initial condition we compute the total longitudinal position change, $\Delta x_f - \Delta x_0$ and plot the heatmap of this value (Fig. 4.8b). Non-zero values of longitudinal position change represent scenarios where interaction forces drive the swimmer pairs to compatibility conditions. Zero values represent the attraction regions. It is interesting to note that while the only interactions between the swimmers are through repulsive contact forces, the confinement and the traveling wave shape change results in regions of longitudinal attraction between the swimmers, effectively a cohesive force between swimmers. This attractive potential will be further studied in the next section.

From the position change map we can clearly see why the three-link swimmer exper-

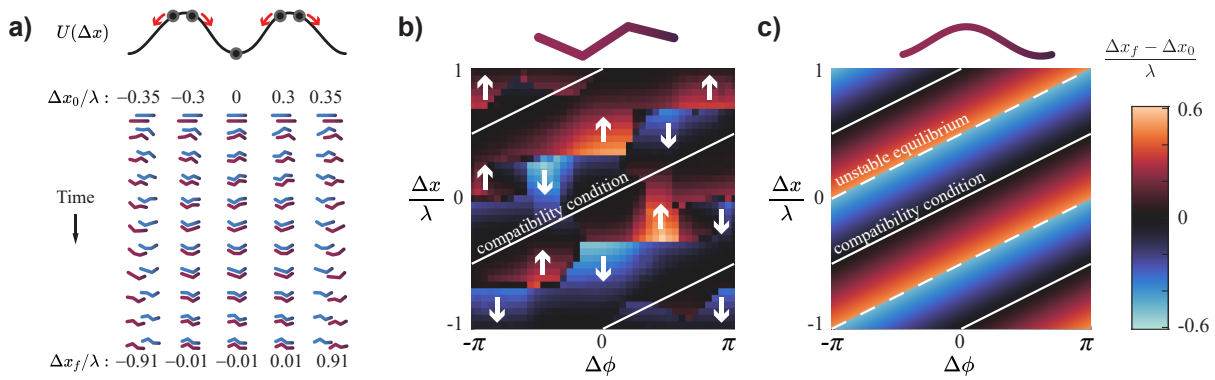

Figure 4.8. Compatible configurations minimize the contact between swimmers. a) We envision that longitudinal dynamics are governed by a potential energy landscape dependent on the phase difference between swimmers. Swimmers initialized with $\Delta\phi = 0$ and different longitudinal positions ($\Delta x_0/\lambda$) evolve to one of three compatible configurations dependent on initial position. All initial positions $|\Delta x_0/\lambda| \leq 0.3$ evolve to $\Delta x_f/\lambda = 0$ b) Heatmap represents the distance traveled from initial condition to compatibility, $\Delta x_f - \Delta x_0$ for three-link swimmers. c) Heatmap represents the distance traveled from initial condition to compatibility, $\Delta x_f - \Delta x_0$ for sinusoidal swimmers. The solid lines are the compatibility lines. The dashed lines separate regions of attraction between the middle and outer compatibility lines.

iment exhibited the clustering along the Δx axis (Fig. 4.3b, and Fig. 4.5a). The minimum of the interaction "potential" does not follow the compatibility prediction from the sinusoidal calculation, and instead follows a stair-stepped shape along the Δx vs. $\Delta\phi$ parameter space (Fig. 4.8b). To determine how the three-link swimmer position change map differs from the sinusoidal prediction we compute the longitudinal position change required for two sinusoidal curves to come in to compatibility when $\Delta y = 0$. For two sinusoidal curves, the longitudinal displacement required to reach compatibility is the minimum Δx_f that results in the compatibility condition ($y_1 - y_2 = 0$; from Equations 4.3 and 4.4). In Figure 4.8c we show the displacement required to reach compatibility for two sinusoidal curves. The basins of attraction for the different compatibility lines are shown as solid lines of the same slope in Figure 4.8b. Along the dashed lines we observe that the minimum distance for compatibility undergoes a discrete change in sign. An initial condition slightly below the upper dashed line will evolve to the central compatibility line while an initial condition slightly above the upper dashed line will evolve to the upper compatibility line.

4.3.7 Potential energy modeling of compatible configurations in simulation

To gain insight into the forces two swimmers experience when not in compatibility we performed simulations. In a first set of simulations we constrained the mid-point position (but not orientation) of two three-link swimmer's middle link so that swimmers could interact through contact forces but could not move their central position laterally or longitudinally. We arranged swimmers with lateral separation, $\Delta y = 3$ cm and longitudinal separation $\Delta x = 0$. In this arrangement $\Delta\phi = 0$ is the compatible configuration. In a sweep of simulations we varied $\Delta\phi$ conditions and measured the time-averaged contact forces between swimmers over five periods. The compatibility condition coincided with a minimum in the contact forces (Fig. 4.9a) while detuning phase resulted in an increase in contact force. This observation indicates two important points: 1) as expected contact interactions drive the spatial dynamics in this system, and 2) the system evolves to a state which minimizes the contact interactions among these active undulatory swimmers.

We hypothesize that the time-averaged contact dynamics between swimmers can be considered as an effective interaction potential with a minimum at compatibility. To measure the effective potential of the compatibility configurations in simulation we allowed two swimmers with $\Delta\phi = 0$ to reach compatibility and then we applied a constant longitudinal separating force, δF, to each swimmer in opposing directions (Fig. 4.9b). The separating force, δF, was applied to each swimmer by applying a force of $\delta F/3$ to the center of mass of each link on the simulated swimmers. We observed that the swimmers separated by a longitudinal distance δx in the presence of this force and for small δF this position was sustained until the force was removed (Fig. 4.9b). Thus, through the force perturbation we can probe the potential energy basin of the compatible configuration for $\Delta\phi = 0$.

In simulation we varied δF and measured δx over a range of confinement wall distances to observe the cohesive interaction. We observed a linear relationship between the applied

force and the steady state separation suggesting that compatible configurations act like a simple harmonic potential (Fig. 4.9c). We fit the "stiffness" of the compatible state as $\delta F = k(\delta x - \delta x_0)$ where k is the interaction potential and δx_0 is an offset. The offset δx_0 represents the ability for systems with large enough lateral spacing to be found over a range of longitudinal separation distances (Δx) when in compatibility. As we continue to increase the separating force, δF, the average interaction force between the swimmers is no longer able to hold them together and they will separate longitudinally. In this case the swimmer pairs eventually separate and decouple from each other.

We measured the time it takes for swimmers to separate by a center to center distance of L under different forces and confinement distance. The separation time increases with decreasing δF (Fig. 4.9d). When there is no lateral constraint, the escape time was estimated and shown as the black line which is linear (slope = -0.99) on log scale as shown in the inserted plot. We can provide rationale for this inverse behavior between applied force, δF, and separation time. In the absence of contact forces the separation time can be estimated through the relationship between applied force, $\pm\delta F$, and viscous force through the following quasi-steady relationship $\delta F = \eta_{avg}\frac{\Delta x}{\Delta T}$. This can be reformulated into the time to separate as $\Delta T = \eta_{avg}\frac{L}{2\delta F}$ which displays the inverse relationship between separation time and force. In this equation η_{avg} represents the period-averaged projected drag coefficient on the swimmers along the direction of motion, and $\Delta x = \frac{L}{2}$ since both swimmers separate by $\pm\frac{L}{2}$ to achieve a total separation of one body length, L.

We found that the cohesion stiffness, k, of the compatible state decreases with increasing wall width and becomes increasingly large as the confining wall spacing decreases (Fig. 4.9e). Furthermore, the range of displacements with zero interaction force ($\delta x_0 > 0$) qualitatively follows the compatibility condition (Eqn. 4.5) which is shown in the dashed line of Figure 4.9f. These simulations indicate that compatible states are neutrally stable configurations and a linear interaction force drives swimmers into compatibility. The boundary of the neutral region, δx_0, likely lies below the prediction from the compatibility model due to the three-link geometry of the swimmers. This is similar to the comparison of the sinusoidal and three-link compatibility

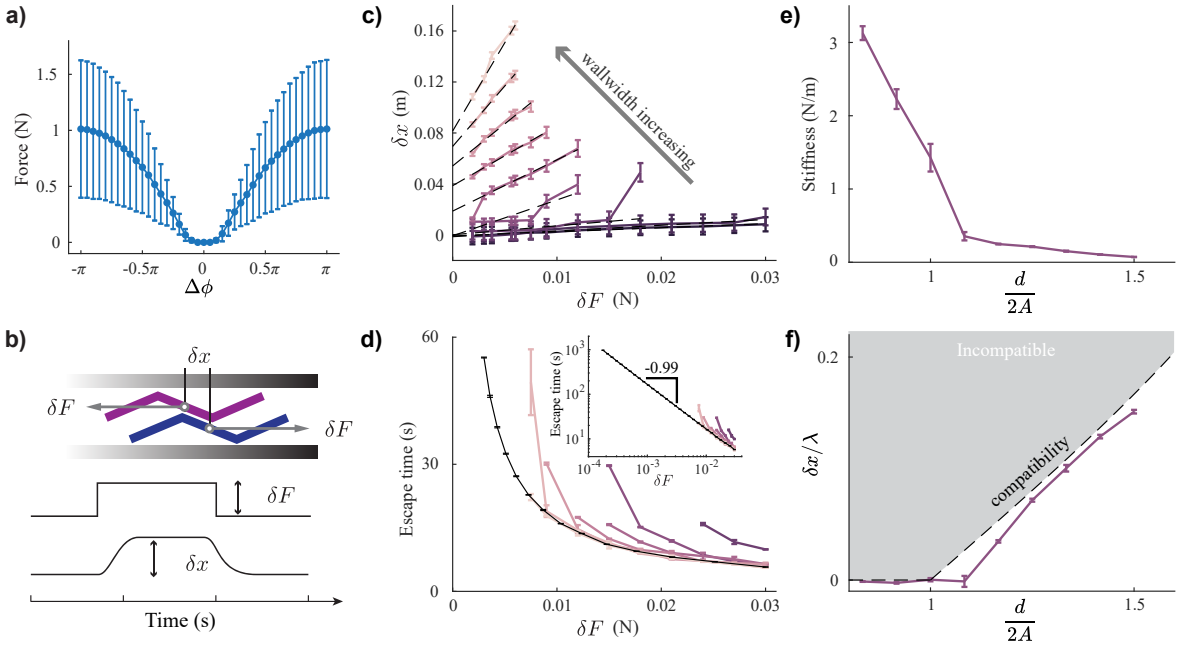

Figure 4.9. Cohesive longitudinal interactions depend on confinement. a) Magnitude of contact force between two swimmers during five periods of oscillation, with initial conditions $\Delta x = 0$ and $\Delta\phi$ varied from $-\pi$ to π. The contact interaction force grows with compatibility detuning. Dots represent mean contact force and error bars are standard deviation. b) The cohesive magnitude of the compatible configuration was measured by applying equal and opposite perturbation forces, δF. The separation distance from compatibility, δx, is measured. c) Force-displacement relationship for nine confinement distances of wall widths (0.10 m to 0.18 m in 0.01 m increments). Error bars represent the standard deviation of δx at applied δF. d) Escape time for wall widths (0.12 m to 0.18 m in 0.01 m increments). The black curve represents the escape time without walls. Error bars represent the standard deviation of escape time. e) Effective interaction spring constant as a function of wall width. Error bars represent estimated spring stiffness with 95% confidence bounds. f) Offset distance (δx_0) as a function of wall width. Error bars represent estimated δx_0 intersection with 95% confidence bounds.

basins in which effects of the discrete link geometry cause the observations to deviate from theory.

4.4 Summary and conclusions

In this chapter, we studied the role of contact interactions between undulatory swimmers in experiment and simulation. We found that contact interactions among confined swimmers drive them to stable spatial configurations called compatible gaits (originally introduced in [182]).

The compatibility criteria is determined by the lateral spacing and phase difference between swimmers. We found considerable agreement between the compatibility model prediction and the experiment and simulation results. Compatible gaits are relative equilibrium configurations with time-averaged interactions that have a linear force-displacement relationship along the longitudinal axis and are approximated as a harmonic potential well.

Similar cohesive interactions have been observed to occur in other active, collective systems. However, such interactions are often mediated through a fluid and thus the interaction forces on the bodies can be exerted over long distances and smoothly decay as separation increases. For example recent work has found that the spatial arrangements of undulatory swimmers inspired from fish schools are cohesive, with a strength of interaction that is dependent on the actuation dynamics and spatial positioning [199, 200]. Linear perturbations of these simple swimmers yielded linear interaction forces that were approximated as harmonic potentials [199, 200]. Experiments with tandem undulating foils also demonstrate stable spatial configurations of the foils mediated through fluid mechanics [26] and stable but discrete swimming speeds [27]. A fundamental difference in contact-coupled systems is that once out of reach, interactions can no longer occur. In theory long-slender swimmers in gait compatibility could be infinitesimally close and yet not have any physical interactions because they do not make contact.

This work was inspired in part by the observations of small undulatory worms and their collective swimming behaviors when in close proximity. Pairs of the nematode *C. elegans* were studied in a confined channel (much like in the experiments reported here) and were observed to adjust their undulatory gait to match their neighbor's gait [182]. The authors in that work argue that the nematodes are too large for hydrodynamics to be important and thus it must be contact that is driving the gait dynamics. We acknowledge there are competing theories for why such synchronization occurs in these worms [201], and that close-range fluid interactions may be important, however, these counterpoints do not contradict the work we have presented here. Similar collective undulatory gaits have been observed in the vinegar eels (*Tubatrix aceti*) [184] in which case the authors present a modified Kuramoto model that emulates the effect of steric

interactions to describe the gait adjustment. In this work we do not allow for phase modulation of the swimmers, and only spatial rearrangement. However, this scenario is quite similar to the studies of infinitely long oscillating sheets that do not change undulatory phase but can re-align spatially and which are commonly referred to as "synchronized" in the literature [198].

In this work we focused on planar motion because the systems we are inspired by (*C. elegans*, undulatory robots, etc) typically move in a planar fashion. However, for example the sidewinding motion of snakes and snake-robots [63] occurs in 3D and there might be interesting collective states associated with the interactions of the "corkscrew" shape of the sidewinders. Similarly, we focused on relatively high-density and aligned states of undulatory swimmers, a kind of "undulatory nematic state". However, at lower densities the rotational orientations of the swimmers will become important and may lead to other interesting collective states.

This work is inspired from the broad areas of active matter systems, granular materials, and robotics. The convergence of these themes has been of significant interest in recent years because the stochastic behaviors of interacting robotics systems can be exploited for robust, redundant, and resilient robots. Recent studies of robotic active matter such as smarticles [202] and stochastic particles [203] have highlighted how emergent collective behaviors can be designed and tuned through local contact interaction rules. The role of contact interactions among shape-changing active matter systems may have applications in designing collective robot swarms that operate in close proximity. Building large functional systems from many constituent parts is not new in robotics and has gone under the titles of modular, reconfigurable, and swarm robotics over the years (See [204] and [205] for reviews). However, recent connections drawn between these robotic collectives and active matter physics [206, 207] suggest novel and fruitful intersections between these fields in the years to come.

4.5 Acknowledgement

Chapter 4, in full, is a reprint of the material as it appears in Zhou, W., Peralta, J.D., Hao, Z. and Gravish, N., 2022. Lateral contact yields longitudinal cohesion in active undulatory systems. *Physical Review E*, 105(5), p.054604. The dissertation author was the primary researcher and the first author of this paper.

Chapter 5

Collective synchronization of undulatory movement through contact

Many biological systems synchronize their movement through physical interactions. By far, the most-well studied examples concern physical interactions through a fluid: Beating cilia, swimming sperm and worms, and flapping wings all display synchronization behavior through fluid mechanical interactions. However, as the density of a collective increases, individuals may also interact with each other through physical contact. In the field of "active matter" systems, it is well known that inelastic contact between individuals can produce long-range correlations in position, orientation, and velocity. In this work we demonstrate that contact interactions between undulating robots yield novel phase dynamics such as synchronized motions. We consider undulatory systems in which rhythmic motion emerges from time-independent oscillators that sense and respond to an undulatory bending angle and speed. In pair experiments, we demonstrate that robot joints will synchronize to in-phase and antiphase oscillations through collisions, and a phase-oscillator model describes the stability of these modes. To understand how contact interactions influence the phase dynamics of larger groups, we perform simulations and experiments of simple three-link undulatory robots that interact only through contact. Collectives synchronize their movements through contact as predicted by the theory, and when the robots can adjust their position in response to contact, we no longer observe antiphase synchronization. Lastly we demonstrate that synchronization dramatically reduces the interaction forces within confined

groups of undulatory robots, indicating significant energetic and safety benefits from group synchronization. The theory and experiments in this study illustrate how contact interactions in undulatory active matter can lead to novel collective motion and synchronization.

5.1 Introduction

The study of oscillations in biological systems have lead to fundamental understanding of the dynamics of coupled oscillators [208, 209]. Biological locomotion typically arises from oscillatory movements, and groups of living systems can exhibit coupled movement oscillations when interacting. For example, recent studies have demonstrated that fluid forces acting between pairs of flagella [33, 34, 35], arrays of cilia [36, 37, 38], and even flapping wings [26, 27, 39] can lead to phase and frequency synchronization of oscillatory body movements. However, many animal and robot groups operate in close proximity where movements may result in collisions, leading to collective jamming [42, 41], disorder-to-order transitions in traffic flow [16, 210], and synchronization of oscillatory swimming gaits [182]. In this work we study the phase dynamics of oscillators that are coupled only through intermittent mechanical contact. We provide experimental and theoretical evidence that inelastic mechanical collisions between independent oscillators produce a rich array of phase dynamics in contact-coupled systems.

Synchronization in biological systems can be observed across all scales—from genetic oscillators within cells [211, 212] to collective animal groups within habitats [213, 214, 45]. While synchronization is observed across a wide variety of different systems ultimately it requires two fundamental properties [54]: (1) perturbations to the phase of each oscillator neither grow or decay, and (2) oscillator interactions can influence phase. Many mechanical systems possess both such properties, for example the original pendulum clocks of Huygens [215] exhibit (1) autonomous oscillations that (2) interact through structural motion. In the context of undulatory locomotion there are two main archetypes for autonomous oscillations [216]: central pattern generators that provide an adaptive global “clock”, and reflexive oscillators that

generate spontaneous oscillations through local feedback. Critically both modalities incorporate environmental and proprioceptive feedback. Many abstractions of these circuits exist [5, 6, 7] and one common model is the phase-oscillator which oscillates at a constant frequency ω and can be augmented with sensory feedback.

Collectives that interact through contact have been extensively studied in the soft-matter fields, such as active matter and granular materials. Inert systems that interact through contact such as granular materials exhibit novel nonlinear phenomena such as inelastic collapse [217, 218], jamming [219], and transitions between fluid and solid states [220]. However, granular materials require external driving forces to stay in motion. In contrast active matter systems generate spontaneous movement through internal energy reservoirs and external interactions with the group [152]. Studies of self-propelled "dry" active matter have demonstrated that inelastic collisions are responsible for the collective motion and long-range order in dynamical states such as flocking, jamming, and phase separation (see [221] for a review). Recent experiments and simulation of undulatory active matter systems such as swimming sperm [32, 186], and reciprocating robots [202, 222], have demonstrated that contact interactions can lead to novel spatial ordering. However, the explicit ability for these mobile systems to adapt phase and synchronize through contact is unknown. In this manuscript we study an active matter system of undulatory robots and demonstrate that inelastic mechanical collisions produce a rich dynamics of collective behavior through contact-coupling alone.

As a first example of contact-coupled synchronization we introduce the Newton's cradle toy (Fig. 5.1). Newton's cradle is a series of metal balls mounted on wires so that they each undergo pendular motion. When one ball is allowed to fall under pendular motion and collide with the group, energy is transferred through collisions (with some energy loss) and the ball on the other end will rotate upwards. A less appreciated aspect of this process is that as time evolves energy is lost due to collisions and eventually the system settles into a state where all of the pendulums are oscillating in phase and in continuous contact. This is a simple example of a contact-coupled dynamical system in which the pendulum are initially out of phase, but through

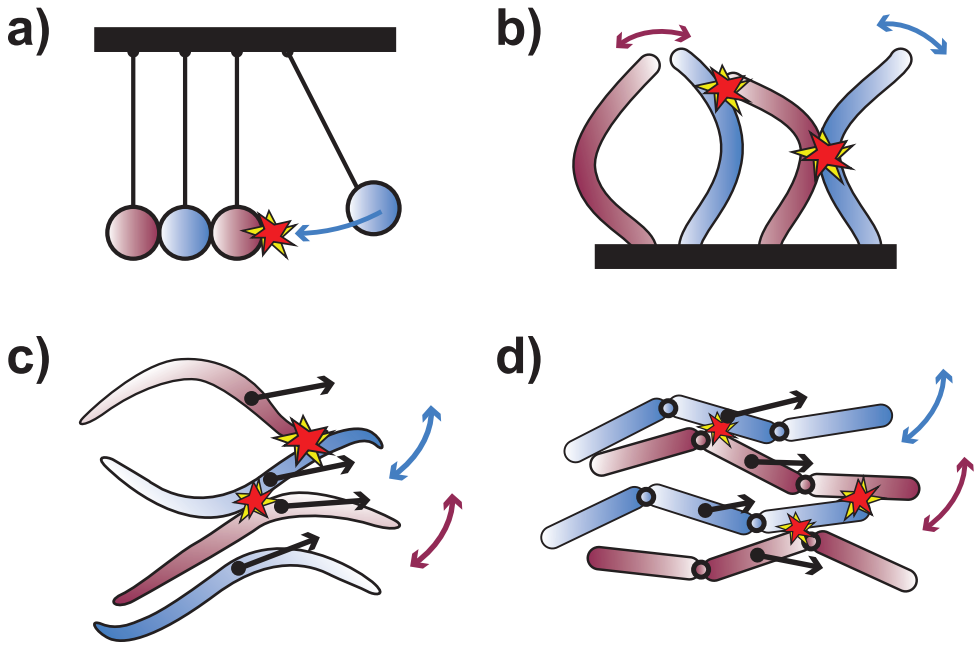

Figure 5.1. Examples of oscillators that interact through contact. a) The balls of the Newton's cradle toy collide and synchronize to in-phase oscillations. b) Arrays of flapping cilia in close proximity can be driven to synchrony through contact [40]. c) The undulatory gait of swimming worms (*C. elegans*) synchronize through contact interactions [182]. d) Simple three-link "Purcell-swimmer" robots similarly synchronize their gaits through contact as demonstrated in this work.

repeated collisions and energy loss the system is driven to a synchronous oscillating state.

In active oscillating systems energy loss through dissipation or collisions can be compensated for by energy input, thus exhibiting limit-cycle oscillations [45]. The oscillatory movements of some biological systems can be considered as limit-cycle oscillators [5, 223] prompting our interest in the phase dynamics of active oscillatory systems that interact through contact (Fig. 5.1). We consider simplified representations of biological systems that move through undulation: our experimental robots use rotary joints and have rigid links. To allow the robots to evolve in undulatory phase we use a simple autonomous nonlinear oscillator to drive sinusoidal motions of the robots.

In the following sections we study how oscillatory systems can achieve synchronization when they interact through contact. In section 5.2 we present a simple theoretical model of contact synchronization and we analyze the steady-state modes and their stability through a

contact-to-contact iterated map. In section 5.3 we introduce a simple experiment to examine how two robot joints can synchronize through mechanical contact and we compare with the theoretical model. To understand how contact interactions may apply to larger groups we perform simulations of 1D lattices and study their dynamics in section 5.4. In the next two sections we perform experiments and simulations on simple three-link robots that interact through collisions. We demonstrate that the in-phase synchronization predicted by our phase model, and observed in our first experiments, is observed in robot groups (section 5.5). To find out why synchronization is beneficial in mobile groups we measure contact forces between robots and compare between the synchronous and asynchronous states (section 5.6). When robot joint oscillation is driven through time-dependent sinusoidal control the contact forces are orders of magnitude larger than when the robots are allowed to synchronize.

5.2 A model of synchronization through contact

We begin by studying a simple model of two phase oscillators that represent body-bending elements, or the joints of undulatory robots (Fig. 5.2a). We consider that undulatory motion is generated according to the phase oscillator equation, $\dot{\phi} = 1$. The oscillator phase governs the lateral position of the undulating body-element, such that $x_i = A\cos(\phi_i)$ is the lateral distance from the body center-line, and $\dot{x}_i = -A\sin(\phi_i)$ is the lateral speed (Fig. 5.2b). When two body elements are in close proximity they will come into contact when the following condition is met $A\cos(\phi_1) - A\cos(\phi_2) = d$, where d is the separation distance of the central axis of the two agents. We introduce the normalized separation distance, $\tilde{d} = \frac{d}{2A}$, such that only when the condition $\tilde{d} \leq 1$ will oscillators be able to contact.

The contact condition thus becomes

$$\cos(\phi_2) - \cos(\phi_1) = 2\tilde{d} \tag{5.1}$$

When the oscillator pair collides they each have a velocity of $\dot{x}_i^- = -A\sin(\phi_i^-)$ where superscripts

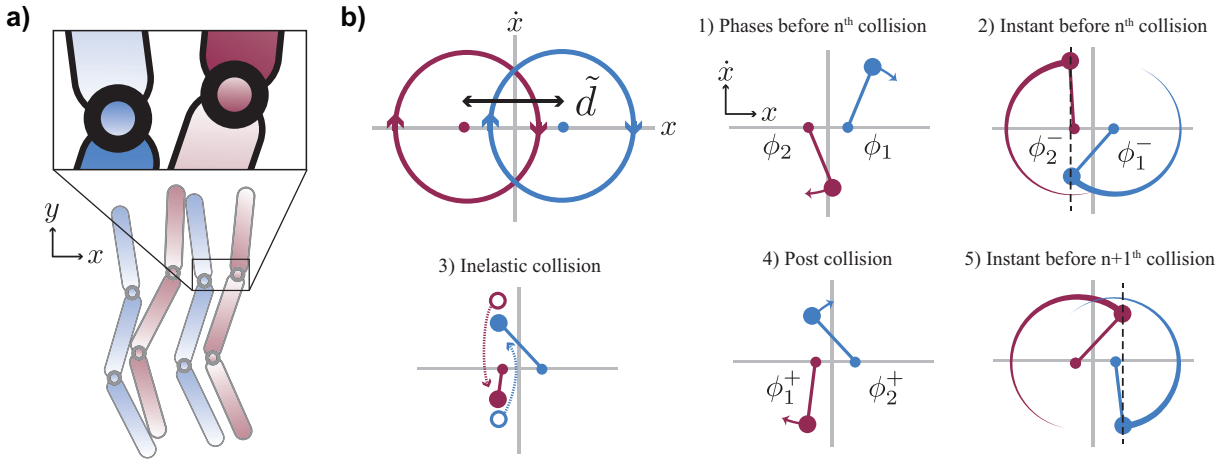

Figure 5.2. A phase oscillator model for contact mediated synchronization of undulatory gaits. a) Undulatory motion is generated through periodic bending of body elements at joints. b) We envision that the motion of the body in the lateral direction (x) is governed by a phase oscillator that produces harmonic motion. The evolution of the collision model is shown in steps 1-5. 1) Oscillators are initially at phase difference $\Delta = \phi_2 - \phi_1$. 2) Oscillators will collide when $x_1 = x_2$. 3) During a collision the velocities are instantaneously updated according to an inelastic collision law and the phase difference changes. 4) Immediately post-collision the oscillators continue evolving until 5) they collide again resulting in a new post-collision phase difference.

$\pm$ denote before ($-$) and after ($+$) collision variables (Fig. 5.2b). We model the collision as an inelastic process with coefficient of restitution r such that $\dot{x}_1^+ - \dot{x}_2^+ = -r\left(\dot{x}_1^- - \dot{x}_2^-\right)$. Combining the inelastic collision model with conservation of momentum, $\dot{x}_1^+ + \dot{x}_2^+ = \dot{x}_1^- + \dot{x}_2^-$, yields the following post-collision velocities (we assume equal masses)

$$\dot{x}_1^+ = \frac{1}{2}\left[(1-r)\dot{x}_1^- + (1+r)\dot{x}_2^-\right] \tag{5.2}$$

$$\dot{x}_2^+ = \frac{1}{2}\left[(1-r)\dot{x}_2^- + (1+r)\dot{x}_1^-\right] \tag{5.3}$$

When the oscillators collide they instantaneously change their phase due to the velocity change (Fig. 5.2b). The oscillator phase is represented in the phase-plane as the clockwise angle from the positive x axis to the instantaneous coordinate $(x,\dot{x})$. Thus, the phases before and after

a collision can be represented by the following equation

$$\phi_i^{\pm} = \text{atan}\left[-\frac{\dot{x}_i^{\pm}}{x_i^{\pm}}\right] \tag{5.4}$$

The negative sign accounts for the fact that the rotation direction is in the clockwise direction.

We seek to understand the asymptotic behavior of the phase difference, $\Delta = \phi_2 - \phi_1$. In systems with continuous coupling this often amounts to demonstrating that $\dot{\Delta} = 0$ [54]. However, since this system consists of repetitive collision events the phase difference, Δ, is constant in between collisions and changes instantaneously during a collision. Thus, we will derive the iterated map that takes the pre-collision phase difference of the $(n)^{\text{th}}$ collision to the pre-collision phase difference of the $(n+1)^{\text{th}}$ collision, $\Delta^{(n+1)} = f\left(\Delta^{(n)}\right)$. We represent the phase difference of the n^{th} collision as $\Delta^{(n)}$ where we have dropped the superscript $+$ for notation convenience. To derive $f\left(\Delta^{(n)}\right)$ we take the following steps: 1) solve for ϕ_1 and ϕ_2 at collision which gives $\Delta^{(n,-)}$, 2) apply the velocity update rule for the inelastic collision, 3) determine the post-collision phases for the oscillators. Since ω is the same between each oscillator the n^{th} post-collision phase difference is exactly the same as the $n+1^{\text{th}}$ pre-collision phase difference and thus $\Delta^{(n,+)} = \Delta^{(n+1,-)}$. We have now determined the function that generates $\Delta^{(n+1,-)}$ from $\Delta^{(n,-)}$ and we can drop the $\pm$ superscripts yielding $\Delta^{(n+1)} = f\left(\Delta^{(n)}\right)$. This results in the collision-to-collision return map

$$\Delta^{(n+1)} = \text{atan}\left[\frac{\sin(\kappa)\cos(\frac{\Delta^{(n)}}{2}) - r\cos(\kappa)\sin(\frac{\Delta^{(n)}}{2})}{\cos(\kappa)\cos(\frac{\Delta^{(n)}}{2}) - \sin(\kappa)\sin(\frac{\Delta^{(n)}}{2})}\right] - \text{atan}\left[\frac{\sin(\kappa)\cos(\frac{\Delta^{(n)}}{2}) + r\cos(\kappa)\sin(\frac{\Delta^{(n)}}{2})}{\cos(\kappa)\cos(\frac{\Delta^{(n)}}{2}) + \sin(\kappa)\sin(\frac{\Delta^{(n)}}{2})}\right] \tag{5.5}$$

where we have defined $\kappa = \text{asin}\left(\tilde{d}\csc\left(\frac{\Delta}{2}\right)\right)$.

The collision-to-collision return map allows us to examine the asymptotic behavior and dynamics of synchronization for contact coupled oscillators. We first examine the fixed points of

the map, $\Delta^* = f(\Delta^*)$. The return map for $0 < r \leq 1$ exhibits three fixed points as a function of separation. Two of the fixed points exist independent of the coefficient of restitution

$$\Delta^* = 2\,\mathrm{asin}(\tilde{d}) \tag{5.6}$$

$$\Delta^* = \pi \tag{5.7}$$

while the third fixed point depends on r and must be solved numerically. We define the first fixed point (Eqn. 5.6) as the compatibility curve, because it defines the maximum phase difference between two oscillators separated by $\tilde{d}$ before they will collide (see inset Fig. 5.3a). When oscillators are at the compatibility fixed point they will repeatedly make grazing contact with each other. The compatibility curve actually determines the boundary of an entire set of fixed points for these oscillators, since if the phase difference, $|\Delta^*| < 2\,\mathrm{asin}(\tilde{d})$, the oscillators will never contact each other and thus Δ will never change. The second fixed point (Eqn. 5.7) is an antiphase oscillation. We show the fixed points in Figure 5.3a for $r = 0.67$ where the lower branch is the compatibility fixed point, and the upper branch is the antiphase fixed point.

When the separation distance is zero ($\tilde{d} = 0$) the compatibility fixed point corresponds to perfect in-phase synchronization, $\Delta^* = 0$ and the return map dramatically simplifies to $\Delta^{(n+1)} = -2\,\mathrm{atan}\left(r\tan\left(\frac{1}{2}\Delta^{(n)}\right)\right)$. This equation can be solved recursively to generate the phase difference of the n^{th} collision as a function of any initial condition ($\Delta^{(0)}$)

$$\Delta^{(n)} = -2\,\mathrm{atan}\left((-r)^n \tan\left(\frac{1}{2}\Delta^{(0)}\right)\right) \tag{5.8}$$

and we clearly see that for large n the phase difference converges to $\Delta^* = 0$.

Equation 5.8 highlights the importance of inelastic collisions in the synchronization process for contact coupled oscillators. The coefficient of restitution, r, governs the rate of convergence to the synchronization fixed point for $\tilde{d}$. The linear stability of fixed points in the collision-to-collision map are determined by the condition $|f'(0)| < 1$ where prime denotes

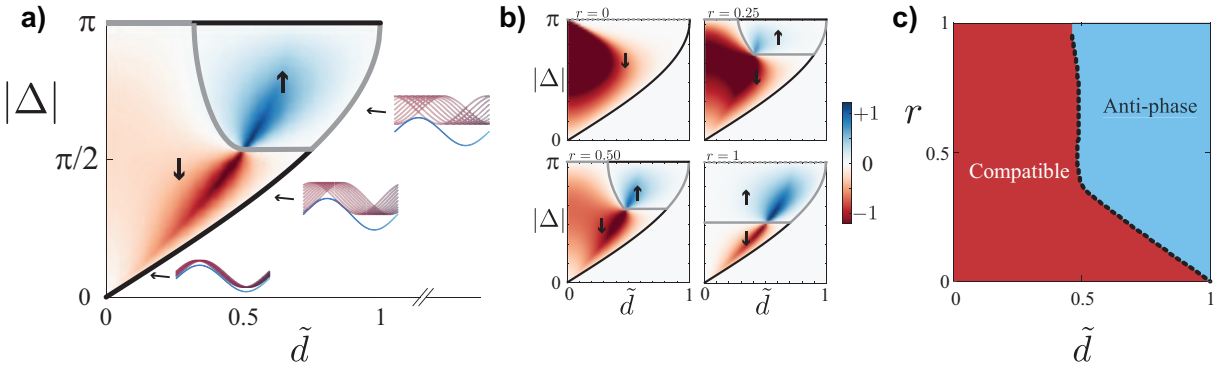

Figure 5.3. The evolution of the phase difference is captured by the phase oscillator model. a) For an initial phase difference, Δ, and separation distance, $\tilde{d}$, a collision will induce a change in Δ. The heatmap shows the collision to collision phase difference, $|\Delta^{(n+1)}| - |\Delta^{(n)}|$ at each $(\tilde{d}, \Delta)$ location (Eqn. 5.5). States in the red region result in a decrease in the absolute phase difference, while states in the blue region increase in phase difference. Black lines are stable fixed points, solid gray lines are unstable, and dashed gray lines are marginally stable. The lower black curve is the compatibility fixed point (Eqn. 5.6). The coefficient of restitution is $r = 0.67$. The inset shows three different separation distances and the range of "compatible" phase differences that can exist without collision. b) Collision to collision phase change behavior at four different restitution coefficients. The black lines are stable fixed points, the gray lines are unstable fixed points, and dashed gray lines are neutrally stable. c) The average steady-state from random initial phases as a function of separation distance and restitution coefficient.

the derivative with respect to $\Delta^{(n)}$. For the $\Delta^* = 0$ fixed point the stability is $f'(0) = -r$ again highlighting the importance of inelasticity in the synchronization process. Thus, because inelastic interactions always generate energy loss ($0 < r < 1$) the system is guaranteed to reach phase synchronization when $\tilde{d} = 0$.

To analyze the time evolution of the system when $0 < \tilde{d} < 1$ we will construct the basins of attraction for the fixed points by calculating the phase change behavior after a single collision event, $g(|\Delta^{(n)}|) = |\Delta^{(n+1)}| - |\Delta^{(n)}|$. In Figure 5.3a-b we plot $g(|\Delta^{(n)}|)$ and denote with arrows and color the flow direction of the compatible (down arrow, red) and antiphase (up arrow, blue) basins. We observe that for each r there is a critical $\tilde{d}_c$ below which all initial phase differences are attracted to the compatible state. However, for larger $\tilde{d}$ the antiphase basin causes states that start with large $|\Delta|$ to evolve to antiphase synchronization (blue regions in Fig. 5.3a,b).

To analyze the behavior of the antiphase fixed point (Eqn. 5.7) we similarly construct

the basin of attraction and linear stability. Since the return map at $\Delta^* = \pi$ has a continuous first derivative we can compute the linear stability of this point. Evaluating the derivative we find

$$f'(\pi) = -\frac{r\left(d^2-1\right)+d^2}{r^2\left(d^2-1\right)-d^2} \tag{5.9}$$

which yields the critical separation distance, $\tilde{d}_c = \sqrt{\frac{r(r-1)}{r^2-r-2}}$. When $\tilde{d} > \tilde{d}_c$ antiphase oscillations switch from unstable to stable. However as $r \to 0$ the range of $\tilde{d}$ where $|f'(\pi)| < 1$ becomes vanishingly small as $f'(\pi)$ converges to $f'(\pi) = 1$ for infinitesimal $\tilde{d}$. The overall influence of r and $\tilde{d}$ can be understood by averaging the collision-to-collision phase change across all initial phases, highlighting that for modest $r \approx 0.5$ and above the average steady-state behavior is evenly divided between the antiphase and compatible states (Fig. 5.3c).

In this section we have proven that a simple model of phase oscillators interacting through intermittent inelastic collisions can produce a rich range of dynamical behavior. We observe in-phase synchronization for small separation distances, and antiphase synchronization for larger distances. Furthermore, this system admits a continuum of "fixed points" when the phase difference is below the compatibility line, in which case the oscillators are completely uncoupled and do not contact. In the next sections we will demonstrate in experiment and simulation that the pair-wise interactions of contact-coupled oscillators leads to rich collective behaviors.

5.3 Synchronization of robot joints in experiment

To validate the model introduced in the previous section we performed experiments with two oscillating motors that interact through collisions (Fig. 5.4a). Each brushless DC motor (Quanum 5250) represents the joint of a robot and is actuated under closed-loop torque control. Rigid 9 cm long aluminum links and viscoelastic bumpers were attached to both motors (Fig. 5.4a). We measured the experimental coefficient of restitution of the system to be $r = 0.67$ (SI Fig. 5). A capacitive encoder attached to the motor shafts provided angular position measurements at a resolution of 8192 counts per revolution, which is 0.044° (AMT102, CUI

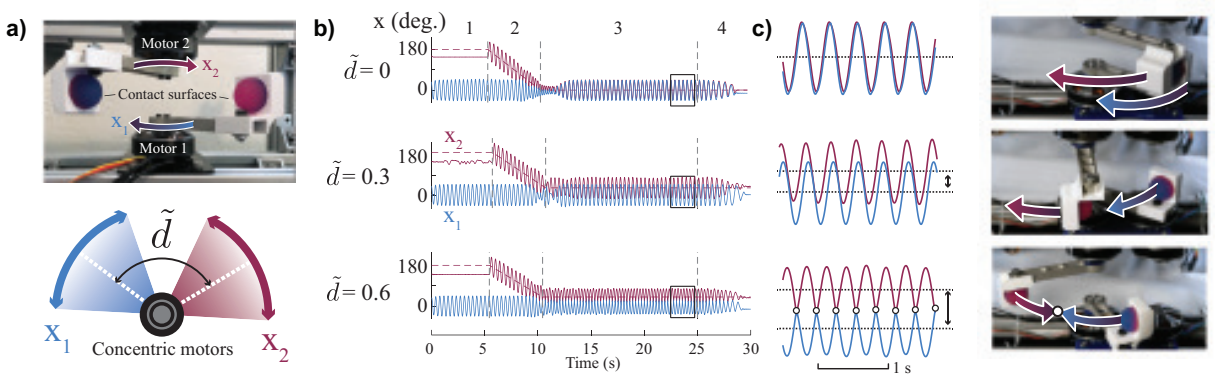

Figure 5.4. Experimental validation of synchronization between undulatory robot joints. a) Two motors mounted on a concentric axis are actuated as phase oscillators. The oscillators interact through inelastic collisions when their rotation angle is equal. b) Data from three separation distances. Robot joints are initially oscillated out of contact to achieve steady-state behavior (Phases 1 and 2) and are slowly brought into contact (Phase 2) to their final fixed distance, $\tilde{d}$ (Phase 3), until the experiment is over (Phase 4). c) At low $\tilde{d}$ joints synchronize, at intermediate $\tilde{d}$ joints oscillate with compatible phases and don't contact, and at large $\tilde{d}$ joints collide in antiphase synchronization. Images are from SI Video 1.

Devices). An ODrive brushless DC motor controller (ODrive robotics) provides closed loop torque control for both motors individually.

We consider the joint rotation angle and rotational velocity as the position and velocity variables of our phase oscillator, $(x, \dot{x})$. In order to actuate these motors as phase oscillators we controlled the motor torque (at a rate of 300 Hz) using the following equation

$$\tau_i = -kx_i + \left(c - \mu x_i^2\right)\dot{x}_i \tag{5.10}$$

where x_i is the relative angular displacement from the neutral angle and i refers to the oscillator. We assume the motor internal damping and friction are small and the systems inertia (I) is the same for both motors, such that $I\ddot{x}_i = \tau_i$. Note there is no coupling between the motors in equation 5.10, the only interactions are through inelastic collisions.

The motor actuation Equation 5.10 represents a generic form of the Van der Pol oscillator which generates sinusoidal oscillations with constant phase speed ($\dot{\phi}$) for weak nonlinearity [45]. Thus, this choice of actuation enables the robot joints to oscillate sinusoidally with constant

phase velocity consistent with our phase oscillator model in the previous section. The position and velocity feedback terms in Equation 5.10 enable the actuator to instantaneously respond to collision-induced velocity changes also consistent with our model assumptions. The actuation parameters of Equation 5.10 were chosen such that the oscillators had natural frequencies of $\omega_1 = 2.61 \pm 0.04$ Hz, and $\omega_2 = 2.63 \pm 0.03$ Hz and amplitudes of $A_1 = 44.4 \pm 0.9$ degrees, and $A_2 = 44.3 \pm 1.6$ degrees. For the purposes of analysis and variable definitions we assume equal amplitudes between the oscillators.

To study the phase dynamics between the two colliding oscillators we set up steady limit-cycle oscillations with the systems initially separated by a large neutral position, $\tilde{d} = 2$. The lower link was allowed to oscillate and after a random time in the range of 5-7 seconds the upper link was perturbed to limit cycle oscillations. This random wait time set a random initial phase difference between the two oscillators. Once both links were oscillating at steady-state we slowly moved the neutral position of the second oscillator to the prescribed separation $\tilde{d}$ for that experiment. Once the oscillators were at the appropriate $\tilde{d}$ we continued the experiment for 15 seconds until reducing the amplitude and stopping. We measured the oscillator positions and velocities throughout the experiment (Fig. 5.4b) and computed collisional information including the phase difference before each collision, $\Delta^{(n)}$. In total we performed 1312 experiments over a range of separation distances where collisions were possible, $\tilde{d} \in [0,1]$, and a control separation distance $\tilde{d} = 2$ to rule out any coupling through the structure. In Figure 5.4b-c and supplementary video 1 we show experiments from three $\tilde{d}$ showing in-phase synchronization ($\tilde{d} = 0$), compatibility ($\tilde{d} = 0.3$), and antiphase synchronization ($\tilde{d} = 0.6$).

We first compare the model predictions and experiment for the $\tilde{d} = 0$ return map (Eqn. 5.8). In experiment the oscillators synchronized phases through repeated collision events eventually reaching a final synchronized state where the oscillators moved together in or near contact (Fig. 5.4b-c). The experimental collision-to-collision return map showed consistent in-phase synchronization as predicted by Eqn. 5.8 from all initial conditions (Fig. 5.5a). To rule out the effect of slowly bringing the oscillators together (Phase 2 in Fig. 5.4b) we performed a

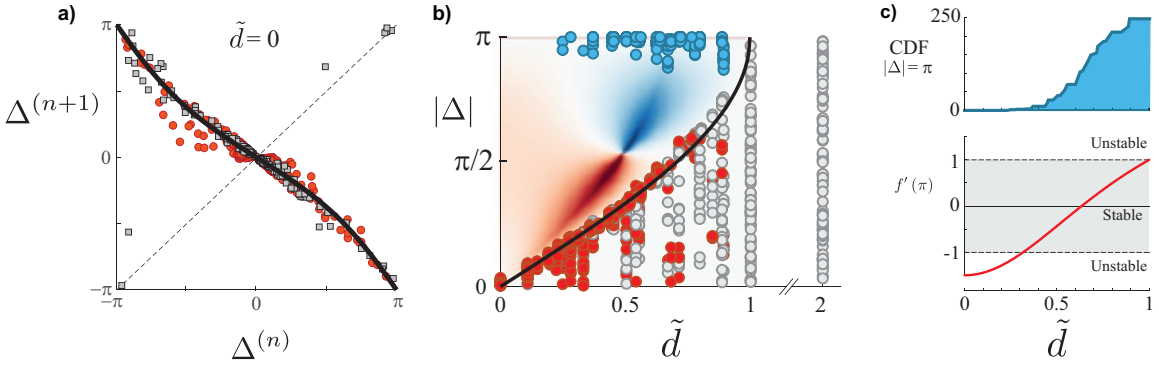

Figure 5.5. Experiment results. a) Collision return map from two separate experiment methods (over 100 experiments for each). Squares are from experiments in which limit cycles are slowly moved together to $\tilde{d}=0$, circles are experiments in which oscillators are initialized with $\tilde{d}=0$. b) Steady-state phase difference (Δ) versus separation distance ($\tilde{d}$) from 1312 experiments. The black line represents the compatibility curve (Eqn. 5.6). Gray and red circles are points that reached a steady-state configuration in which they no longer collide. Red circles started with $|\Delta|$ above the compatibility curve and evolved downwards to the compatible state, while gray circles represent initial conditions below the compatibility line. Blue points are states that evolved to stable antiphase oscillations in which the oscillators repeatedly collide head-on. Heatmap is the model prediction from the collision-to-collision return map for $r=0.67$ (Eqn. 5.5). Far right points at $\tilde{d}=2$ are control experiments. c) Experimental observation of antiphase oscillations coincide with onset of antiphase stability in model. Top is the cumulative distribution of observations of antiphase oscillations versus $\tilde{d}$. Bottom is the stability eigenvalue of antiphase behavior for $r=0.67$ (Eqn. 5.9).

second set of experiments in which both oscillators began at $\tilde{d}=0$ and random initial phase. We observed good agreement in the collision-to-collision return map between both experimental methods. The model and experimental return map exhibited excellent agreement indicating that the phase-oscillator model is able to capture relevant phase dynamics of this system (Eqn. 5.8; black curve in Fig. 5.5a). It is important to note here that their are no fitting parameters in the model. Since the phase dynamics are evaluated from collision-to-collision we do not need to match frequencies or amplitude between experiment and model. The prediction only requires knowledge of one parameter, the coefficient of restitution r which can easily be measured.

We next compare the steady-state Δ across the full experimental range of $\tilde{d}$ (Fig 5.5b). Comparison of the theoretical compatibility curve (Fig. 5.5b, solid line) and the experimental data indicates good agreement between the phase oscillator model and observation. We observe that

initial phases that start in the compatible state will continue to stay there (gray circles, Fig. 5.5b), and initial phases that start outside of the compatible state may either evolve to antiphase oscillations or compatibility depending on initial conditions. The red circles in Figure 5.5b show initial conditions that began above the compatibility line and evolved to the compatible state. Blue circles represent initial conditions that began above the compatibility line and evolved to the antiphase state (Fig. 5.5b).

The antiphase state consisted of the two oscillators repeatedly colliding with each other (see supplementary video 1) in a rather violent manner which lead to broken components on more than one occasion. The antiphase state observed in experiment was found to be remarkably stable and able to resist manual perturbations consistent with the stability calculations in Section 5.2. In one experiment we observed the two oscillators remain in the antiphase state for over 12 hours until we eventually halted the experiment. The return map allows us to predict when antiphase oscillations become stable (Eqn. 5.9). In Fig. 5.5c we compare the cumulative observations of antiphase oscillations and the linear stability calculation (Eqn. 5.9). Once again we find exceptional agreement between the model and experiment: as the antiphase fixed point in our model becomes stable we begin observing antiphase oscillations in experiment.

5.4 Collective behavior of mobile and stationary oscillator groups

We next seek to understand whether contact interactions among larger groups can yield similar synchronization and phase dynamics as the robot-pair experiments. We consider the lateral dynamics of arrays of mobile cilia and groups of swimming worms as a one-dimensional lattice where nearest-neighbor collisional interactions occur along the direction of body undulations (Fig. 5.6a). To simulate the dynamics of mobile and fixed systems we allow the neutral position of each oscillator to move in response to a collision. Immediately after a collision we update the neutral positions of the colliding oscillators according to the equation $\delta_i = \beta\left(\dot{x}_j - \dot{x}_i\right)$

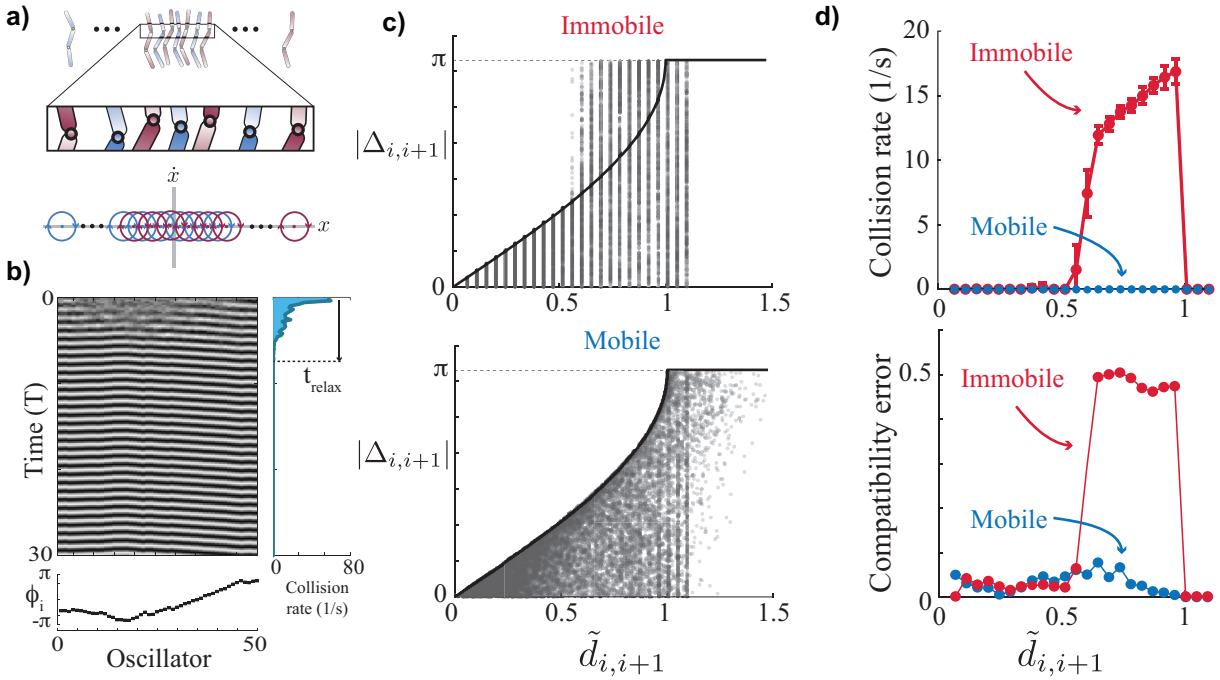

Figure 5.6. Phase dynamics for oscillator lattices. a) Phase dynamics of undulatory robots are modeled as a one-dimensional lattice with interactions occurring along the lateral direction. Body undulations between neighboring robots can lead to contact. b) The spatio-temporal evolution of phase for an oscillator group (50 oscillators, $\tilde{d} = 0.14$, $\beta = 0$). Bottom plot shows final phases. Right plot shows the rate of collisions and the relaxation time, t_{relax} after which no collisions occur. c) Final phase difference and separation distance between adjacent oscillators. Top shows phase behavior for oscillators with an immobile base ($\beta = 0$). Bottom shows results for mobile oscillators ($\beta = 0.1$) in which the equilibrium position moves as a result of collisions. d) The collision rate and compatibility error versus $\tilde{d}$. Mobile oscillators always evolve to states with no collisions (top) and good agreement with the compatibility equation (bottom).

where δ_i is the neutral position change of the i^{th} oscillator and β is the magnitude of collision-induced change. When $\beta = 0$ the system base is immobile (as in arrays of cilia) while non-zero β allows for oscillators to repel each other through collisions. To confine the oscillator group to a fixed linear distance we set $\beta = 0$ for the left ($i = 0$) and right ($i = N$) oscillators in the N-oscillator lattice. We perform numerical simulations of the one-dimensional oscillator lattice over varied initial neutral positions spanning $\tilde{d}_{i,i+1} \in [0.06, 1.2]$. We simulated 50 oscillators initialized at random phases and observe the phase dynamics, collision rate, and neutral position of the group over time.

When the oscillator lattice is initiated in close proximity (small $\tilde{d}_{i,i+1}$) the oscillators

rapidly converge to a compatible state through collisions (Fig. 5.6b) in both the immobile and mobile cases. Collisions between oscillators initially occurred due to the random incompatible phases and over time the collision rate decreased ultimately halting after a time, t_{relax}, for small $\tilde{d}_{i,i+1} < 0.5$. Once all oscillators are in the compatible state they will stay there indefinitely unless perturbed.

To quantitatively compare the oscillator lattice results with the theoretical model and experiments from the previous section we measured the nearest-neighbor phase difference, $|\Delta_{i,i+1}|$, and nearest-neighbor separation distance of the neutral position, $\tilde{d}_{i,i+1}$. Examining the relationship between phase difference and spatial separation reveals a fundamental difference between mobile and immobile systems (Fig. 5.6c). Immobile oscillator lattices show good agreement between the theoretical predictions and simulation for $\tilde{d}_{i,i+1} < 0.5$. However when separation distance was large ($\tilde{d}_{i,i+1} > 0.5$) the collisions never stopped and the oscillator groups never entirely reached the compatible state (Fig. 5.6d; top). We measured the collision rate over the last ≈ 70 periods of oscillation and observe a sharp rise in non-zero steady-state collisions when $\tilde{d}_{i,i+1} > 0.5$ for the immobile system. This is supplemented by the large cluster of points above the compatibility curve in Figure 5.6b for the immobile case. To characterize this deviation from model prediction we calculated the fraction of nearest-neighbor pairs that were above the compatibility curve and plot this compatibility error in Figure 5.6d. The immobile base simulations exhibited a large compatibility error and persistent colliding among the group when $\tilde{d} > 0.5$.

The immobile system's deviation from the compatibility curve is easily understood from the pair-wise dynamics of oscillators modeled and studied in the previous sections. At larger separation distances the collision-to-collision phase change causes oscillator pairs to increase in phase difference. This phase repulsion is what leads to the stable antiphase mode in the pair experiment. However, in larger groups the interior oscillators have a left and right neighbor and thus experience phase repulsion from both of these neighbors which is not able to relax in simulation. These results are in agreement with observations from lattices of locally-coupled

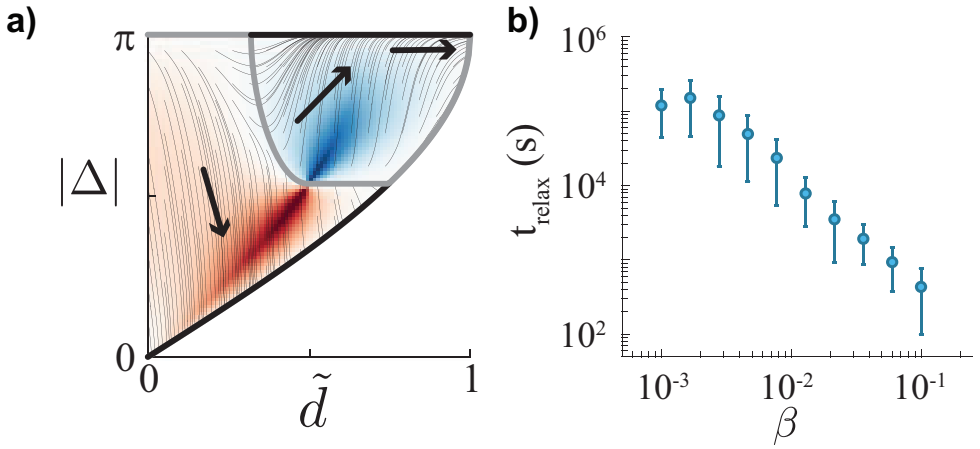

Figure 5.7. Collision induced mobility allows groups to reach compatibility. a) Phase and spatial evolution of mobile oscillator groups. Collisions result in an increase in separation distance and thus the system evolution tends towards larger $\tilde{d}$ and there is no longer a stable antiphase state. b) The system relaxation time versus mobility coefficient, β, for $\tilde{d} = 0.78$. As β decreases relaxation time increases. $\beta = 0$ coincides with the immobile simulation in which case the system evolves to stable antiphase behavior.

Kuramoto oscillators in which repulsive phase interactions have been demonstrated to generate asynchronous collective states [224].

In contrast to the immobile system, oscillators that were able to move in response to collisions always relaxed to the compatible state. The phase and spatial values clustered at or below the compatibility curve (Fig. 5.6c) and exhibited low numbers of collisions and low compatibility error in steady-state (Fig. 5.6d). The small but non-zero compatibility error for the mobile system is likely due to the assumptions of pure sinusoidal motion in the theory, compared to the slight deviation in sinusoidal behavior that Equation 5.10 generates. The deviation from compatibility in the mobile system was still small and clustered on or just above the compatibility line.

The ability for mobile systems to always achieve compatibility can be understood by examining the phase and space dynamics from our theoretical model. In the fixed base system the only free degree of freedom is Δ and thus oscillator pairs can only increase or decrease in phase difference (the state evolution in Fig. 5.3 is only vertical). However, when the base is allowed to move in response to collisions the oscillator pairs have a second degree of freedom

and the system can evolve through phase change or separation change. Because the spatial change between oscillator pairs is only repulsive this emerges as a lateral drift towards larger $\tilde{d}$ in the collision-to-collision state evolution (Fig. 5.7a). antiphase oscillations are no longer a stable fixed point because the high-impact collisions will drive the oscillators apart until they will settle at the point $(\tilde{d} = 1, \Delta = \pi)$.

To demonstrate that spatial movement inhibits antiphase oscillation we examined the long time dynamics of an oscillator lattice initialized at a separation distance that leads to antiphase oscillation in pairs and repetitive collisions in groups ($\tilde{d} = 0.78$). We varied the the magnitude of collision-induced spatial change, β, over two orders of magnitude and observed a nearly three order of magnitude increase in the relaxation time (Fig. 5.6b). This power law behavior matches previous simulations and intuition from our model: immobile systems will never relax to collisionless compatibility since $t_{relax} \to \infty$ as $\beta \to 0$. Thus we see a fundamental difference between mobile and fixed-base systems that undulate and interact through collisions, and these results suggest that mobile robots and organisms will always evolve to compatible, collisionless states through contact.

5.5 Robots synchronize gaits through collisions

Lastly we examine how groups of mobile undulatory robots synchronize their gaits through contact. We performed both experiments and simulations with simple three-link robots that have two active servomotors (Dynamixel AX-12, Robotis) controlling joint angles α_1, α_2, and three rigid links of length 18.65 cm (Fig. 5.8a). Such a three-link system is often referred to as "Purcell's swimmer" and was originally introduced by E.M. Purcell as a minimal model of low Reynolds swimming [170]. The three-link robot has been studied extensively in the context of locomotion through fluids [175, 225], on frictional surfaces [172, 173], and within granular media [174]. In addition three-link robots have been recently used to study the collective behavior of robot groups that exhibit time-dependent oscillatory motion and push each other

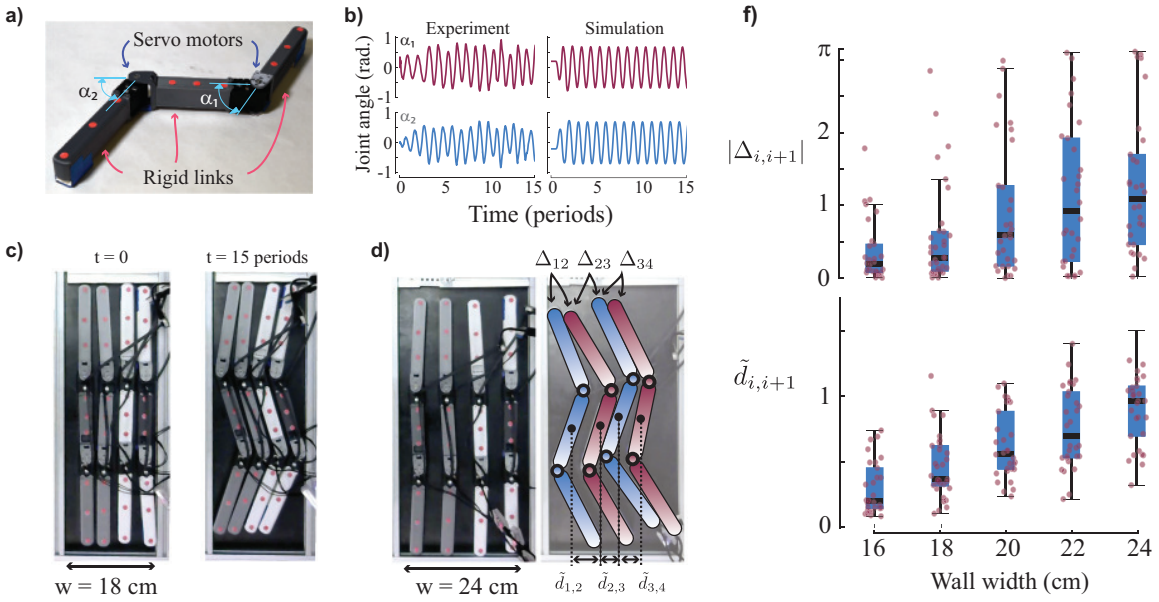

Figure 5.8. Three-link robot experiments demonstrating synchronization through collisions. a) A simple robot with three rigid links and two servo motors generates undulatory motion. b) The motion of the joints when controlled as a phase oscillator are shown for the experimental system (left) and a simulation (right). c) Experiments with four robots in a controlled width channel demonstrate synchronization of movement over time. d) We measured the phase difference, $\Delta_{i,i+1}$, and lateral separation, $\tilde{d}_{i,i+1}$, between neighboring robots. f) Phase difference and separation distance between robots after 15 periods of oscillation from five different wall width experiments (10 trials each). Boxplots show 25-75% confidence intervals (blue box) and median (horizontal black line). All observations are plotted as red circles.

through contact [192, 202, 222].

In experiment the robot actuators are controlled by continuously sending position commands for the joint angle at a rate of 100 Hz. To actuate the robot joints according to the phase-oscillator model using position controlled servos we numerically integrated the oscillator equation used in the motor pair experiments (Eqn. 5.10) solving for the next joint angle at each timestep. Critically this actuation method required measuring the instantaneous joint angle and joint velocity from the servos and thus incorporates proprioceptive feedback to generate autonomous oscillations, consistent with the direct-drive motors of the previous experiment.

We simulated the three-link robots using the Project Chrono multibody physics simulation engine [193]. In simulation we directly controlled the torque of the rotational joints consistent

with the previous two motor experiment (Eqn. 5.10). Contact interactions in the simulation were modeled through short-range repulsive viscoelastic interactions, and we added stokes-drag fluid forces to the robot links according to the method in [226] to mimic the damping from friction in experiment. In both the experiment and simulation we incorporated methods to enforce a constant phase difference between joints ($\alpha_1 - \alpha_2 \approx \frac{2}{3}\pi$) to produce traveling wave body undulations. We modified slightly the actuation equation by adding a coupling term (λ) between joints α_1, α_2

$$\tau_{i,j} = -k\left(x_{i,j} + \lambda_j x_{i,\bar{j}}\right) + \left(c - \mu x_{i,j}^2\right)\dot{x}_{i,j} \tag{5.11}$$

in which subscripts $i = 1,2,3,...$ represents the number of robots and $j = 1,2$ represents the two joints of robot i. The coupling constants for the two joints were $\lambda_1 = 1.5$ and $\lambda_2 = -0.5$, and the position $x_{i,\bar{j}}$ refers to the opposite joint of the robot. The position and torque control methods of the experiment and simulation produced body undulations of the robot with a constant frequency and phase difference (Fig. 5.8b). In experiment the frictional interactions between the robot links and ground caused perturbations to the robot joint motion, however this did not affect the synchronization behavior of the robots.

To observe whether multiple undulatory robots will synchronize their gaits through contact we put groups of four robots within a confined rectangular channel (Fig. 5.8c; supplementary video 2). In experiments we only tested configurations where the robots were aligned longitudinally but we tested the effect of longitudinal misalignment in simulation. The rectangular channel was 55 cm long and we tested five different widths, $w \in [16, 18, 20, 22, 24]$ cm with 10 trials at each width. The experiment began with the robots evenly spaced in the lateral direction and at random initial phases. After 30 s (approximately 15 periods of oscillation) we stopped the experiment and measured the final phase difference, $\Delta_{i,i+1}$, and spatial distance, $\tilde{d}_{i,i+1}$, between neighboring robot pairs (Fig. 5.8d). Increasing the wall width caused both $\Delta_{i,i+1}$ and $\tilde{d}_{i,i+1}$ to increase (Fig. 5.8e).

We performed similar three-link robot synchronization experiments in simulation. In

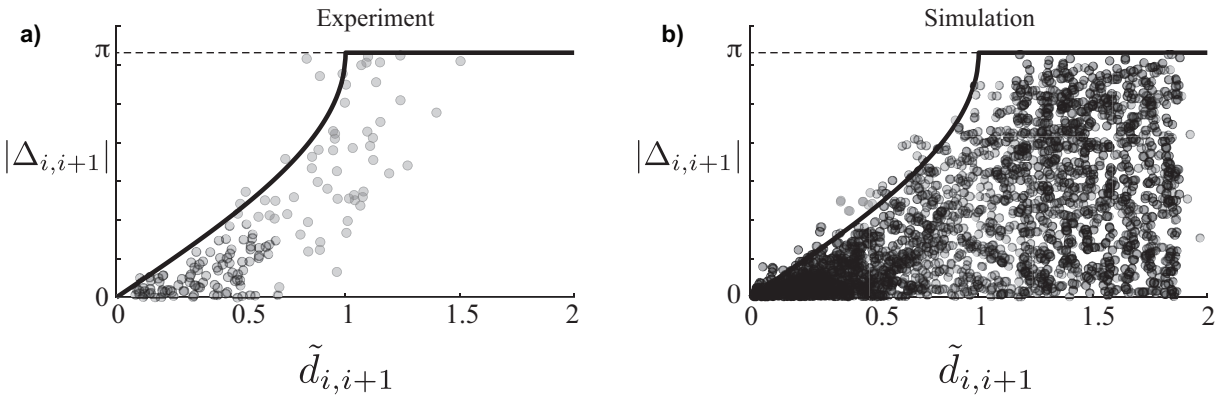

Figure 5.9. Robots adjust their undulatory phase and lateral distance according to the theoretical model (black curve; Eqn. 5.6). Results from simulation (n = 210) and experiments (n = 50) at random initial conditions.

addition to simulating the experiments performed with physical robots, we also increased the number of robots and increased the confinement arena size to represent two-dimensional simulations in which robots occupied a rectangular region. Qualitatively the one-dimensional and two-dimensional arenas exhibited similar spatial and phase effects, with nearby robots influencing each other in undulatory phase and reaching compatibility.

In all experiments (n = 50) and simulations (n = 210) the three-link robots adjusted their undulatory phase through collisions and the final states were well characterized by the theoretical model of Section 5.2. When we examine the nearest neighbor phase difference versus lateral separation we see that all robot-robot interactions lead to phase and distance states that are near, or below the compatibility condition (Eqn. 5.6; black line in Fig. 5.9). Critically we never observed antiphase synchronization as we did in the earlier two-joint experiments from section 5.3 or the immobile lattice simulations from Section 5.4. The lack of antiphase behavior is understandable from the mobile simulations in Section 5.4, when robots collide they push each other away and this spatial repulsion drives them out of contact before they will synchronize to antiphase.

The extremely good agreement we observe from both the simulation and experiment with the compatibility model indicates that contact interactions have an important role in collective

phase dynamics. Initial states outside of compatibility evolved to synchronized movement when spacing was small, and compatible phases at larger spacing. It is important to note that the mobile robots in simulation and experiment can displace and rotate with respect to each other thus indicating that the phase dynamics model of Section 5.2 is robust to misalignment and natural variation. However, it remains to be demonstrated what benefits gait synchronization would have for undulatory collectives. In the last section we compare time-dependent actuation in asynchronous group versus undulatory generation through autonomous oscillators that enables synchronization.

5.6 Synchronization minimizes contact forces in undulatory groups

In this last section we seek to determine what is the potential benefit of gait synchronization for collectives. There are likely many metrics that could be influenced by synchronization: locomotion energetics and collective sensing for example. Here we focus on the interaction forces between robots that occur when in high-density spatial arrangements.

We conducted simulations with groups of ten three-link robots in a confined rectangular volume (Fig. 5.10a). Initially the robot joints were actuated through a time-dependent position control signal with fixed frequency and amplitude

$$\bar{\alpha}_{i,j} = A \sin\left(\phi_i + \frac{2\pi}{3}(j-1) - 2\pi f t\right) \tag{5.12}$$

in which subscripts $i = 1,2,3,...$ represents the number of robots and $j = 1,2$ represents the two joints of robot i. The position command was converted to a control torque through a proportional control law $\tau_{i,j} = -k\ (\alpha_{i,j} - \bar{\alpha}_{i,j})$ where $\alpha_{i,j}$ is the actual joint angle. The proportionality constant k determines how much torque the actuators exert when the position deviates from the time-dependent sinusoidal commands and can be considered as a controller "stiffness". We performed simulations across $k \in [0.015, 0.135]\ \frac{\text{Nm}}{\text{rad.}}$. For each control stiffness we performed

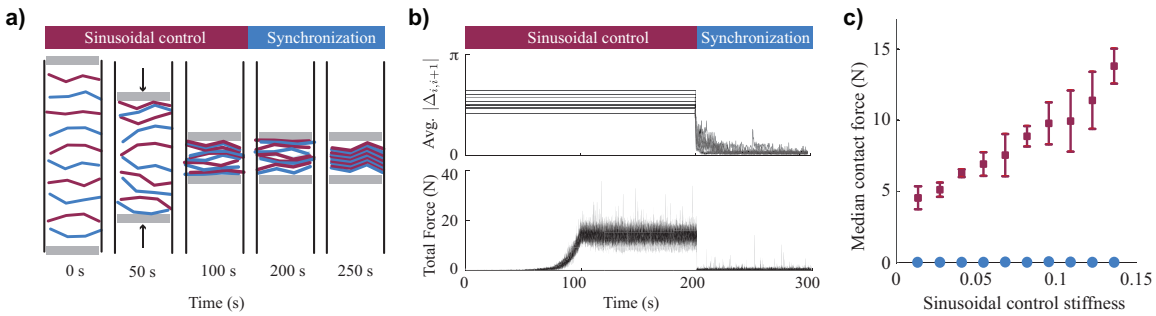

Figure 5.10. Interaction forces in undulatory groups decrease when robots synchronize gait. a) Ten robots in a rectangular arena oscillate through time-dependent sinusoidal control. The top and bottom walls are slowly brought together resulting in persistent collisions. After 200 s the joint control is switched from time-dependent to phase-oscillator actuation and the robots synchronize. b) The phase difference and contact forces are plotted versus time. During time-dependent sinusoidal control the robot phase differences are maintained and contact forces are large. When phase-oscillator control is switched on the robots synchronize causing the phase difference and contact forces to decrease. Ten replicate experiments are overlaid and force is filtered with a running average of 0.1 s. c) The median contact forces during steady-state for time-dependent sinusoidal control (purple squares, calculated from 100-200 s) and limit-cycle control (blue circles, calculated from 200-300 s). The forces during time-dependent sinusoidal control linearly increased with the proportional control constant (the effective "stiffness").

ten simulations at random initial phases ($\phi_i \in [-\pi,\ \pi]$ in Eqn. 5.12). The frequency (0.8 Hz.) and amplitude (0.8 rad.) were chosen to match the oscillation kinematics when the robots are under limit-cycle control (Eqn. 5.11).

To enforce contact and collisions we slowly moved the top and bottom walls inwards towards the arena center. the rectangular region had a constant width of 0.6 m and at the beginning of the simulation the lateral walls were a distance of 2.0 m apart. The width of the lateral walls was decreased at constant velocity from 10 s to 100 s while the robots oscillated, stopping at a lateral width of 0.3 m for the rest of the simulation (Fig. 5.10a). The robots were controlled through time-dependent sinusoidal actuation during the first 200 s and switched to phase-oscillator control from 200-300 s.

We recorded the oscillatory phase, and the contact forces acting on all robot links during each time step. The mean force between robots under the phase-fixed control was significantly larger than that under the phase-oscillator control mode in which synchronization occurred

(Fig. 5.10b). The interaction forces between the robots in the high-density environment were large because the oscillation phases were incompatible resulting in collisions. These collisions persisted and repeated because the phase differences were fixed, leading to a fluctuating mean force with constant time-averaged behavior (Fig. 5.10b) However, when robots were switched to the phase-oscillator control mode, the collisions between robots quickly drove the robot group to synchronization. The median contact force was less than 0.1 N during the phase-oscillator control mode indicating a large reduction in contact forces.

This section demonstrates that robots with undulatory phase differences can experience large contact forces as they push against each other. However when synchronized to the same undulatory phase the collisions reduce to a small and negligible magnitude. Contact forces between robots can be a significant problem and lead to rapid wear and failure. Similar negative consequences are likely to occur in biological collectives where repeated high-force contact can lead to higher energy expenditure and potential injury.

5.7 Discussion

Our results have demonstrated that inelastic collisions between undulatory robots can produce novel phase dynamics such as in-phase and antiphase synchronization, and compatible oscillations that persist without contact. The behavior of larger robot groups tends towards phase compatibility and once achieved the group is effectively decoupled because collisions will no longer occur unless perturbed. The compatible state is similar to the "cohesive" state originally introduced for the Kuramoto system [227] in which cohesive oscillators remain within a bounded phase difference for all time. Compatibility is a beneficial property for undulatory groups because it minimizes the contact forces between individuals and thus likely reduces energetics, fatigue, and damage. Critically this beneficial collective behavior emerges naturally from the physics of inelastic contact and simply requires that undulatory motion be generated through an autonomous oscillator so that phases between robots can "slip" through interactions.

In additional simulations and experiments we have demonstrated that this behavior is insensitive to the particular control law that generates undulation.

The coefficient of restitution from inelastic collisions between robots is the lone governing parameter for phase dynamics among these contact-coupled groups. Inelastic contact interactions generate a wide array of collective behaviors in driven or active nonlinear systems, such as pattern formation [228, 229], particle aggregation [218, 230], and swarming [160, 231]. However, the ability of repulsive contact interactions to drive attractive phase dynamics in oscillators has not been observed. Our phase model is able to explain how phase attraction and repulsion emerges from inelastic collisions. When undulatory systems are in close proximity the collisional interactions between their limit-cycles drive their phase difference to be smaller. However, when the separation distance is large collisions drive the phase difference to grow and generates a stable antiphase mode. Extending these interactions to an oscillator lattice we have shown that phase repulsion can destroy long range order when the oscillators base is immobilized, while mobile undulatory systems always reach compatibility.

Our inspiration for this study comes from collective movement in worm groups in which body and appendage oscillations may occur in close proximity. Recent work has demonstrated that collisional interactions in arrays of cilia can generate synchronization, metachronal wave propagation, and jammed states, dependent on separation [40]. Similarly, recent observations of small worms that swim by laterally oscillating their bodies have illustrated that groups of worms tend to synchronize their oscillatory phase when in close proximity [182, 183, 184]. Genetic manipulations of these worms illustrated that external sensory responses (exteroception) were not necessary for synchronization, and instead the authors argued that collisional ("steric") interactions could produce synchronization [182]. Our results provide a potential explanation for the observed gait synchronization: body oscillations that are governed by internal proprioceptive neural feedback can exhibit emergent synchronization through collisional body interactions alone.

The system explored in this experiment had appreciable inertial dynamics and momentum

transfer through collision. However, in the systems we take inspiration from such as small oscillatory organisms in fluids, inertial dynamics are likely not relevant. Thus, it is important to consider how these results may apply across inertial and non-inertial active matter systems. We propose that contact-coupled oscillators in both the inertial and non-inertial regimes are captured by the coefficient of restitution in our phase model. When $r = 0$, the oscillators do not rebound but instead "stick" together which models the non-inertial behavior of oscillators such as cilia and worms in overdamped viscous environments. However, for $r > 0$ systems exhibit significant rebounding as they collide which captures the behavior of inertial oscillatory systems and can lead to antiphase synchronization (Fig. 5.3b). The reduction of contact-coupled oscillators to a simple model in which r is the only governing parameter allows us to explore these systems across inertial to non-inertial regimes. This will be of interest in future studies and comparisons between model predictions and observations from active matter and swarm robot systems in experiment.

This work has relevance to the field of swarm, and collective robotics where a critical goal is to design distributed control laws that lead to desired, beneficial, emergent behaviors of the group [1]. Recent work in swarm robotics have embraced contact and collisional interactions as a means of coordinating robot group behaviors [232, 233, 234, 235, 236, 237, 238, 239, 240] and other recent work has leveraged collisions [241, 242, 243, 244] for maneuvering individual robots. Our work demonstrates that designing appropriate limit-cycles to actuate the rhythmic motion of robots can lead to emergent synchronization and drastically reduce the contact forces. Thus, the desired collective behaviors of the group are encoded within the gait generation algorithm of the individuals. Future capabilities can thus build on to the collective behaviors studied here. For example, subsets of informed individuals could "herd" the group through contact interactions controlling collective motion.

The coupling of oscillatory dynamics with mobility is an exciting future direction for active matter systems such as biological or robotics swarms. Previous work on mobile phase oscillators in which the phase differences can influence motion of the mobile systems have

demonstrated novel collective flocking and pattern formation behaviors [245, 246, 247]. However, there has been little work to consider how the mechanical collisions between oscillating moving individuals drives collective synchrony or motion patterns. In recent experiments, three-link "smarticle" robots have demonstrated how stochastic interactions among neighboring oscillating robots can drive emergent and controlled collective behavior [202]. However, currently smarticle systems do not have oscillatory phase dynamics and thus synchronization has not been explored. In our work the oscillator phase is intrinsically tied to the undulatory motion of the robotic joint. Thus, phase and motion are explicitly coupled. Future swarm systems that take advantage of the phase dynamics from inelastic collisions may enable emergent synchronization of mobile undulatory robots purely through contact, thus simplifying swarm robot motion control.

5.8 Acknowledgement

We acknowledge helpful discussion from Dan Goldman and Paul Umbanhowar. We thank the UCSD department of Mechanical & Aerospace Engineering for funding support.

Chapter 5, in full, is a reprint of the material as it appears in Zhou, W., Hao, Z. and Gravish, N., 2021. Collective synchronization of undulatory movement through contact. *Physical Review X*, 11(3), p.031051. The dissertation author was the primary researcher and the first author of this paper.

Chapter 6

Conclusions

This dissertation addresses specific problems in oscillatory locomotion of bioinspired robots. In the first chapter, we propose different methods to generate oscillatory motions for robots which are used in the following projects.

In the second chapter, we presented the design of a millimeter-scale inch-worm inspired robot that can push and pull against the ground with simple "feet" to propel itself. The robot is able to operate at frequencies substantially higher than its biological counterparts, which lead to the discovery of different velocity-frequency results when compared to the theoretical predictions of deterministic push-pull locomotion. We showed how basic feedforward oscillatory actuation of the "feet" leads to non-trivial locomotion dynamics through foot slipping and stochastic foot-ground contact mechanics.

In the third chapter, we demonstrated enhanced capabilities of this robot such as turning, that was achieved through incorporation of soft materials in the design process. By combining smart-composite-manufacturing fabrication processes used for rigid robots, with a micro-machining and casting method employed for soft robotics, we integrated soft robotic components into millimeter scale robots. Critically, this work focused on the steering capability of the micro robot by introducing phase difference into the driving PZT actuators, which generates a propagating wave through the soft transmission, enabling the turning movement of the claws.

In the forth chapter, we studied the collective behavior of simple three-link "swimming"

robots that are controlled through feedforward oscillatory actuation. We analyzed the role of contact interactions between undulatory swimmers in experiment and simulation. Oscillatory phase differences between neighboring robots lead to intermittent collisions that drive the group into a stable spatial configuration by lateral and longitudinal movement. Compatible gaits are relative equilibrium configurations with time-averaged interactions that have a linear force-displacement relationship along the longitudinal axis and are approximated as a harmonic potential well. We derive conditions for group spacing and density based on phase variation, examine the effective interaction potential between neighboring robots, and identify a compatibility condition for robots to safely swim in close proximity without collisions.

In the fifth chapter, we enables the oscillatory motion of robot's in a collective to be generated through nonlinear, limit-cycle dynamics. We find that intermittent contact between robots leads to overall group synchronization of oscillatory swimming gaits which reduces contact forces between robots and enables high density configurations. Critically this beneficial collective behavior emerges naturally from the physics of inelastic contact and simply requires that undulatory motion be generated through an autonomous oscillator so that phases between robots can "slip" through interactions. A phase oscillator model of this process is developed and we derive the theoretical conditions for group synchronization, observing good agreement between experiments and the theoretical model. When undulatory systems are in close proximity the collisional interactions between their limit-cycles drive their phase difference to be smaller. However, when the separation distance is large collisions drive the phase difference to grow and generates a stable antiphase mode. This work enables us to demonstrate in experiment the swimming synchronization of four three-link robots that do not communicate with each other, but instead leverage the nonlinear dynamics of the nonlinear oscillator control system. Ultimately, the work we present in this thesis leads to new understanding of how oscillatory motion is influenced by intermittent, nonlinear, interactions with the environment and between robots.

Appendices

A Appendix

A.1 SCM Method

The smart-composite manufacturing (SCM) method was developed to build robotic systems at the millimeter and centimeter scales, with features sizes down to tens of microns [123, 124]. SCM bridges the gap between traditional machining (meter to centimeter) and MEMS (micron to nanometer) fabrication. The SCM method uses multiple laminate layers that are all laser cut and laminated into a single composite sheet (Fig. A.1). Layers are aligned and then cured in a heated platen press and then released to achieve desired micro structures by choice of design pattern and material properties (Fig. A.1). SCM enables the integration of mechanical parts, such as links and joints, and electronic devices, such as PZT actuators, sensors, and wiring, into a complex microrobotic system [123].

Assembly accuracy is a significant challenge in microrobotics and specifically SCM based robots which require folding or manual bonding to achieve three-dimensional structure. Typical SCM laminates have five layers, two structural (carbon fiber), one flexural (Kapton), and two adhesive (DuPont Pyralux) (Fig. A.2). Yet a robot component may be built from many of these five-layer laminates manually bonded together. In an effort to reduce the number of folds required to build our transmission we designed it using a single laminate consisting of 25 layers as a single monolithic structure (Fig. 2.5). Individual material layers are cut into 25 $\times$ 25 mm squares by a DPSS laser, containing complex in-plane features as small as 10 microns which is the resolution of the laser. Out-of-plane 3D mechanical structures are achieved by stacking

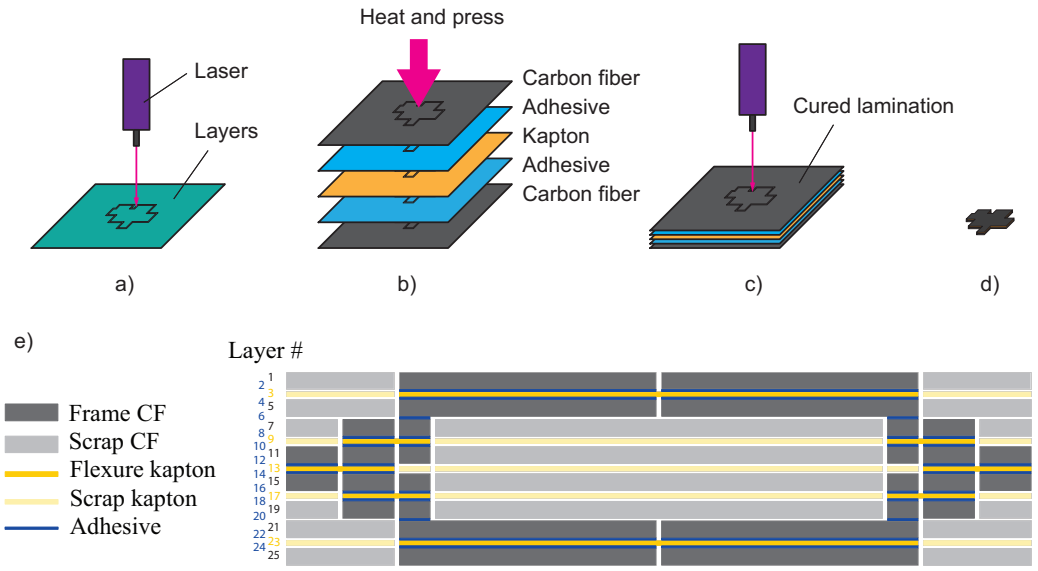

Figure A.1. SCM method. a) Laser cut individual layers. b) A typical SCM laminate consists 5 layers in sequence (Carbon fiber - Adhesive - Kapton - Adhesive - Carbon fiber). Use heated platen press to form cured SCM laminate. c) Laser cut to release the functional parts. d) An example of released micro structure. e) A detailed cross-section of the 25 layers used for the prismatic transmission.

carbon fiber structural layers, Kapton flexure layers, and adhesive layers along precision dowel pins which provide persistent lateral alignment. In the final transmission most material around the in-plane functional features are removed, however for proper support during bonding we need to retain much of this scrap material for structural support. In the stacked multilayer laminate shown in Fig. A.1e, light gray parts of carbon fiber layers and light yellow parts of Kapton layers remain in-plane to provide out of plane support to the surrounding material during the press and cure process. After the transmission is laminated a final laser release cut is performed and the scrap material is removed leaving only the dark gray parts of the carbon fiber layers, dark yellow parts of the Kapton layers, and interleaved adhesive layers are retained. Carbon fiber forms the

links of the linear transmission with $L = 5$ mm. The 0.1 mm Kapton gaps create revolute joints for the linear transmission.

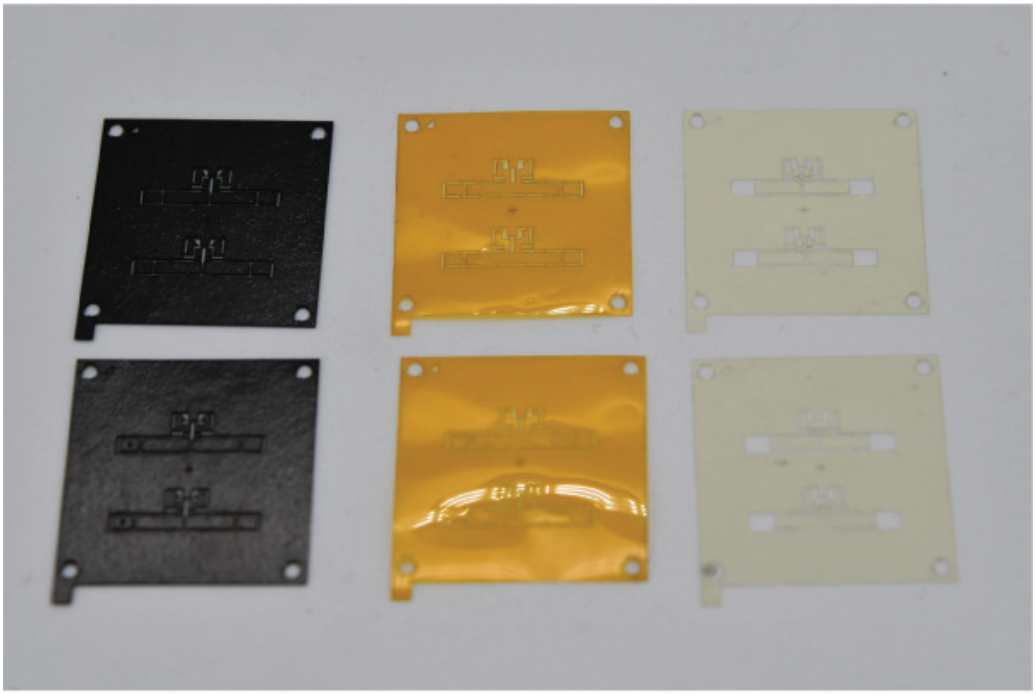

Figure A.2. Selected examples of laser-cut individual layer. The black layers are structural carbon-fiber, the yellow layers are flexural Kapton, and the white layers are adhesive Pyralux.

A.2 Transmission dynamic response

To determine whether the dynamics of the transmission system influenced the locomotion speed-frequency behavior we sought to determine if the claws exhibited a resonance across the rang of tested frequencies. We tracked the output displacement of the transmission during the free-run experiments at all frequencies (Fig. A.3). The result shows the amplitude of transmission does not change significantly across the frequencies we tested. Thus, we assumed the internal dynamic of the PZT actuator and transmission system can be ignored when analyze the robot locomotion dynamic.

A.3 Locomotion testing details

We performed locomotion experiments using two experimental setups (Fig. A.4). The first set of experiments were performed with the robot confined to move within a narrow channel. At the time of this work we had not integrated steering into robot and thus used

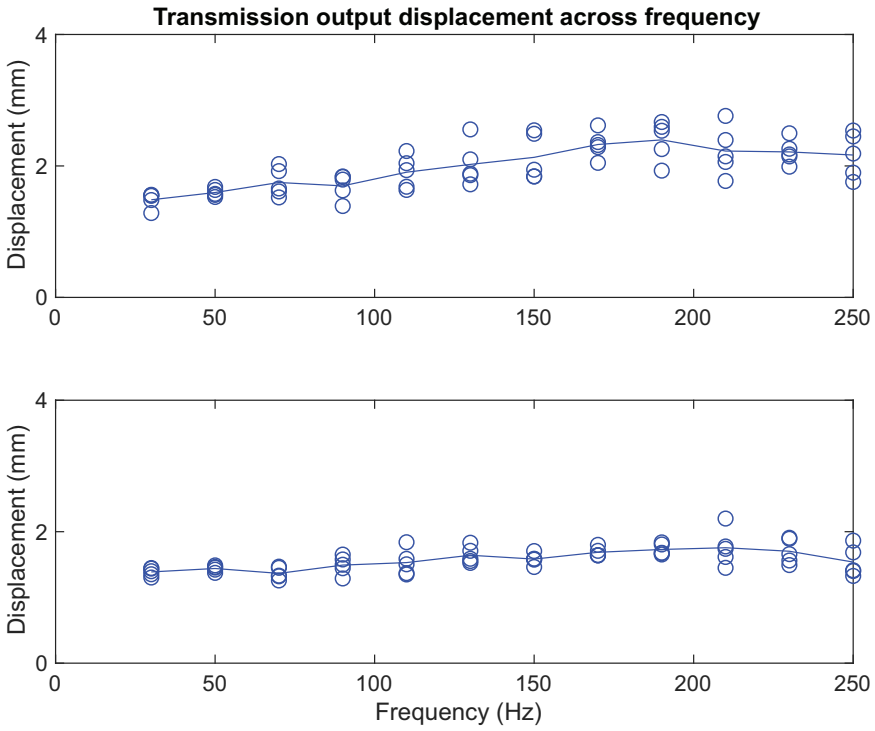

Figure A.3. Dynamic response of transmission. Amplitude of transmission output of the upper claw (above) and lower claw (bottom) across different frequencies. The transmission performance remained consistent across frequency of interest.

the walls to enforce straight motion. The walls were made of transparent acrylic to enable high-speed camera viewing from the side. Figure A.4 shows a view from the high-speed camera in the walled experiment. Free-run experiments were also performed and similar views are shown for the free run experiments. Two high-speed cameras were synchronized and used for all video data collection. Calibration enabled 3D reconstruction of the robot motion.

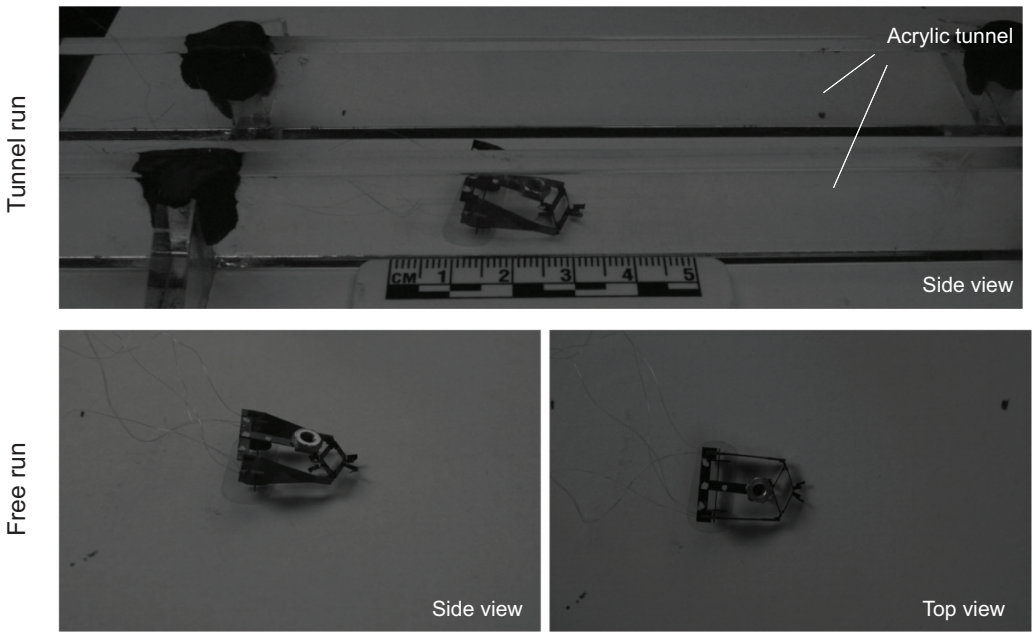

Figure A.4. Robot experiment setup in tunnel run and free run.

B Appendix

B.1 Simulation details

We simulated the multi-swimmer numerical experiments in Project Chrono (referred to as Chrono). Chrono is a multi-physics dynamics engine that handles rigid body dynamics and contact. The source code is freely available [1] and Chrono simulations have been validated against several experiments and comparisons with other numerical solvers for accuracy [193]. Our simulations took place in Chrono version 5.0.0.

A multi-body physics solver is used to model the rigid body dynamics of multi-body systems coupled together through kinematic constraints. Chrono treats the generalized position $\mathbf{q}$ and velocity vectors $\dot{\mathbf{q}}$ of rigid bodies from a Cartesian approach, where the generalized position is the location of each body's center of mass in the absolute coordinate system. The multibody

[1] Code can be found on the Project Chrono github page (https://github.com/projectchrono/chrono)

dynamics in the absence of friction are described by the following set of equations

$$\mathbf{g}(\mathbf{q},t) = \mathbf{0}$$
$$\mathbf{M}(\mathbf{q})\dot{\mathbf{v}} = \mathbf{f}(t,\mathbf{q},\mathbf{v}) + \mathbf{G}(\mathbf{q},t)\hat{\lambda}$$

The first equation represents constraints between bodies, in the case of this manuscript revolute joints, which are contained in the constraint equations $\mathbf{g}(\mathbf{q},t) = \mathbf{0}$. The second equation defines the dynamics where $\mathbf{M}$ is the mass matrix, $\mathbf{f}$ are internal (i.e. Coriolis forces, joint torques) and applied forces, and $\mathbf{G}(\mathbf{q},t)\hat{\lambda}$ represents the constraint reaction forces.

The forces applied to the bodies may also include contact forces that "appear" and "dissapear" when contact between bodies are made or broken. In the implementation in this work, contact is handled through the discrete element method using a complementarity approach (DEM-C). The complementarity approach models contact interactions as "rigid" contacts which cannot penetrate each other. This is in contrast to penalty DEM methods that model contact through elasticity and small body overlap (with elastic repulsive force). These approaches have been compared in the literature [194]. The complementarity approach poses and solves a complementarity optimization at each time-step. The complementarity problem specifies that between every body, either a nonzero gap distance exists, or a nonzero contact force exists. The details of how this complementarity problem is posed and solved are described in Heyn et. al. [195], and Tasora et. al. [193].

The time stepper (time integrator) used in our simulation is the linear implicit Euler method. The step size of this integrator is 0.005 s. A solver is used to compute the unknown accelerations and reaction forces at each time step of the simulation. We are using the default *PSOR*, an iterative solver based on projective fixed-point method, with over relaxation and immediate variable update as in successive over-relaxation (SOR) methods.

We implemented viscous drag forces acting on each link of the simulated swimmers. The viscous drag forces were applied to the center of mass of each link. The drag equations are those

provided in Hatton et. al. [174]

$$F_{i,x} = \int_{-L}^{L} \frac{1}{2} c_d \xi_{i,x} d\ell = c_d L \xi_{i,x}$$
$$F_{i,y} = \int_{-L}^{L} c_d \xi_{i,y} d\ell = 2 c_d L \xi_{i,y}$$
$$M_i = \int_{-L}^{L} c_d \ell (\ell \xi_{i,\theta}) d\ell = \frac{2}{3} c_d L^3 \xi_{i,\theta}$$

where $F_{i,x}$ and $F_{i,y}$ are respectively the longitudinal and lateral forces, M_i is the moment, c_d is the differential viscous drag constant, and $\xi_i = [\xi_{i,x}, \xi_{i,y}, \xi_{i,\theta}]^T$ is the body velocity of the center of the ith link with respect to the stationary fluid [196].

Details of simulation parameters are listed in Table B.1.

Table B.1. Simulation parameters

Name	Variable	Value
Body length	l	162 mm
Body width	w	15 mm
Body height	h	30 mm
Body mass	m	73 g
Control P gain	K_P	0.15 Nm/rad
Torque saturation	T_s	1.5 Nm
Joint amplitude	β_0	40°
Joint frequency	f	0.5 Hz
Drag coefficient	c_d	1

C Appendix

C.1 Derivation of contact map

In this section we derive the collision-to-collision phase map presented in section 5.2. To derive this map we have to first consider how to represent the pre-collision phases, ϕ_i^-, in terms of only the phase difference, $\Delta = \phi_2 - \phi_1$. We seek to solve for the collision phases using only the phase difference between oscillators, Δ. We begin by introducing an intermediate variable κ such that

$$\phi_1 = \kappa - \frac{\Delta}{2} \tag{1}$$

$$\phi_2 = \kappa + \frac{\Delta}{2} \tag{2}$$

The collision condition (Eqn. 5.1 in main text) is

$$2\tilde{d} = \cos(\phi_2) - \cos(\phi_1) \tag{3}$$

and we expand this into the form

$$2\tilde{d} = \cos(\phi_1) - \cos(\phi_2) \tag{4}$$

$$= \cos\left(\kappa - \frac{\Delta}{2}\right) - \cos\left(\kappa + \frac{\Delta}{2}\right) \tag{5}$$

$$= -2\sin(\kappa)\sin\left(-\frac{\Delta}{2}\right) \tag{6}$$

$$\tag{7}$$

which yields the relationship

$$\kappa = \arcsin\left(\tilde{d}\csc\left(\frac{\Delta}{2}\right)\right) \tag{8}$$

This equation allows us to determine for a given initial Δ what the individual phases of the oscillators are at collision by substituting κ into Equations 1 & 2.

Our goal here is to solve for the return map between collisions as a function of Δ. To do this, we take the following steps: 1) solve for ϕ_1 and ϕ_2 at collision from Equations 8, 1, & 2 and, 2) apply the velocity update rule for inelastic collisions from Equations 5.2 & 5.3, 3) determine the post-collision phases for the oscillators from Equation 5.4. Since ω is the same between each oscillator, and they evolve independently until colliding, the post-collision phase difference $\Delta^{(n,+)}$, is exactly the same phase difference of the next collision $\Delta^{(n+1,-)}$. We have introduced the superscript notation where the first value indexes the collision, and the $\pm$ denotes whether the value is before $(-)$ or after $(+)$ the indexed collision.

$$\Delta^{(n,+)} = \phi_2^{(n,+)} - \phi_1^{(n,+)} \tag{9}$$

$$= \text{atan}\left[-\frac{\dot{x}_2^{(n,+)}}{x_2^{(n,+)}}\right] - \text{atan}\left[-\frac{\dot{x}_1^{(n,+)}}{x_1^{(n,+)}}\right] \tag{10}$$

$$= \text{atan}\left[\frac{(1-r)\dot{x}_1^{(n,-)} + (1+r)\dot{x}_2^{(n,-)}}{2x_1^{(n,-)}}\right] - \text{atan}\left[\frac{(1-r)\dot{x}_2^{(n,-)} + (1+r)\dot{x}_1^{(n,-)}}{2x_2^{(n,-)}}\right] \tag{11}$$

$$= \text{atan}\left[\frac{\dot{x}_1^{(n,-)} + \dot{x}_2^{(n,-)} - r\left(\dot{x}_1^{(n,-)} - \dot{x}_2^{(n,-)}\right)}{2x_1^{(n,-)}}\right] - \text{atan}\left[\frac{\dot{x}_1^{(n,-)} + \dot{x}_2^{(n,-)} + r\left(\dot{x}_1^{(n,-)} - \dot{x}_2^{(n,-)}\right)}{2x_2^{(n,-)}}\right] \tag{12}$$

$$= \text{atan}\left[\frac{(1-r)\sin(\kappa + \frac{\Delta^{(n,-)}}{2}) + (1+r)\sin(\kappa - \frac{\Delta^{(n,-)}}{2})}{2\cos(\kappa + \frac{\Delta^{(n,-)}}{2})}\right] \tag{13}$$

$$- \text{atan}\left[\frac{(1-r)\sin(\kappa - \frac{\Delta^{(n,-)}}{2}) + (1+r)\sin(\kappa + \frac{\Delta^{(n,-)}}{2})}{2\cos(\kappa - \frac{\Delta^{(n,-)}}{2})}\right]$$

$$= \text{atan}\left[\frac{\sin(\kappa)\cos(\frac{\Delta^{(n,-)}}{2}) - r\cos(\kappa)\sin(\frac{\Delta^{(n,-)}}{2})}{\cos(\kappa + \frac{\Delta^{(n,-)}}{2})}\right] - \text{atan}\left[\frac{\sin(\kappa)\cos(\frac{\Delta^{(n,-)}}{2}) + r\cos(\kappa)\sin(\frac{\Delta^{(n,-)}}{2})}{\cos(\kappa - \frac{\Delta^{(n,-)}}{2})}\right] \tag{14}$$

Since $\Delta^{(n,+)} = \Delta^{(n+1,-)}$ we have derived the mapping from the collision phase immediately after the n collision to the phase immediately after the $n+1$ collision. Thus we can drop the $\pm$ superscripts and we arrive at the final collision-to-collision return map

$$\Delta^{(n+1)} = \text{atan}\left[\frac{\sin(\kappa)\cos(\frac{\Delta^{(n)}}{2}) - r\cos(\kappa)\sin(\frac{\Delta^{(n)}}{2})}{\cos(\kappa)\cos(\frac{\Delta^{(n)}}{2}) - \sin(\kappa)\sin(\frac{\Delta^{(n)}}{2})}\right] - \text{atan}\left[\frac{\sin(\kappa)\cos(\frac{\Delta^{(n)}}{2}) + r\cos(\kappa)\sin(\frac{\Delta^{(n)}}{2})}{\cos(\kappa)\cos(\frac{\Delta^{(n)}}{2}) + \sin(\kappa)\sin(\frac{\Delta^{(n)}}{2})}\right] \tag{15}$$

C.2 Experiment details

Motor control and limit-cycle generation

Each motor was controlled by an ODrive brushless DC motor controller (ODrive robotics). The ODrive provides closed-loop current control for each motor and we set the maximum current limit to 30 A. The motor current control was performed on a computer in Python. At every update loop the motor current was computed using the following equation:

$$i = -k\theta + c\dot{\theta} - \mu\theta^2\dot{\theta} + \beta\,\text{sgn}(\dot{\theta}) \tag{16}$$

with the following parameters:

Table C.1. Experimental parameters

Variable	Motor 0	Motor 1
k	3.9 A/rad	3.3 A/rad
μ	0.24 A s/rad^3	0.24 A s/rad^3
c	0.009 A s/rad	0.009 A s/rad
β	0.25 A	0.25 A

The constants were selected so that each motor exhibited limit-cycle oscillations of approximately sinusoidal motion with equal amplitude ($A_1 = 44.4 \pm 0.9$ degrees, and $A_2 = 44.3 \pm 1.6$ degrees) and equal frequency ($\omega_1 = 2.61 \pm 0.04$ Hz, and $\omega_2 = 2.63 \pm 0.03$ Hz). The β term in the motor control equation helped overcome the frictional resistance of the motor

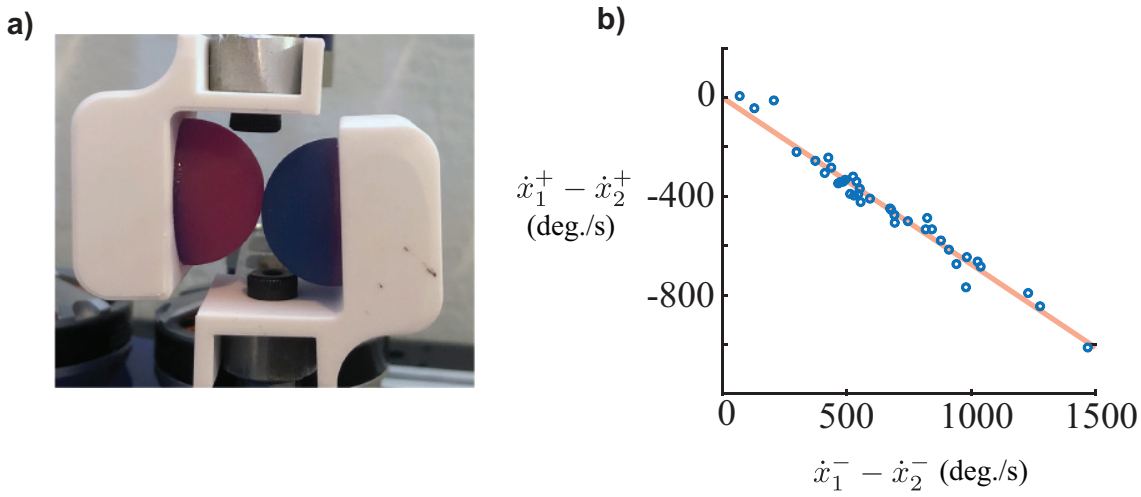

Figure C.1. Measurement of coefficient of restitution for experiment. a) Impacting surfaces. b) Coefficient of restitution measurement. Equation is given in text.

bearings. Without this term, the motor dynamics exhibited a stable fixed point at $(\theta, \dot{\theta}) = (0,0)$ with a small region of attraction around this point.

Collision dynamics

A rigid robot link of length 9 cm was attached to each motor. The link was waterjet cut from 9.5 mm thick aluminum and rigidly fastened to the motor. A 3D printed adapter was attached to the end of each link which provided an impact surface for the two links to interact with each other (Fig. C.1). The colliding surface was an elastic sphere, a bouncy ball, purchased from a commercial vendor.

To determine the coefficient of restitution of the impacting surfaces we performed a series of experiments. The links were accelerated towards each other at a constant motor current (selected at random between 0 - 2 A) for 200 ms after which the current was set to 0 and the motors and links glided towards each other impacting and rebounding. We measured the motor speed immediately prior to the collision and immediately after the collision and computed the coefficient of restitution using the equation, $\dot{x}_1^+ - \dot{x}_2^+ = -r\left(\dot{x}_1^- - \dot{x}_2^-\right)$. We found a coefficient of restitution of $r = 0.67 \pm 0.02$.

Simulation

We performed numerical simulations of colliding oscillator pairs and collectives. Simulations were performed in both Matlab and C++ using the library "odeint" and a variable time-step integrator with absolute and relative tolerances of 1×10^{-6}. An event detection scheme was used in both simulation environment to detect oscillator collisions. At each collision the numerical integration was halted, the inelastic collision model was implemented, and the integration was re-initialized with the new post-collision state. In the simulations with more than two oscillators simultaneous collisions between more than one oscillator pair were not observed.

Bibliography

[1] Guang-Zhong Yang, Jim Bellingham, Pierre E Dupont, Peer Fischer, Luciano Floridi, Robert Full, Neil Jacobstein, Vijay Kumar, Marcia McNutt, Robert Merrifield, Bradley J Nelson, Brian Scassellati, Mariarosaria Taddeo, Russell Taylor, Manuela Veloso, Zhong Lin Wang, and Robert Wood. The grand challenges of science robotics. *Science Robotics*, 3(14):eaar7650, January 2018.

[2] Dario Floreano, Ramon Pericet-Camara, Stephane Viollet, Franck Ruffier, Andreas Brueckner, Robert Leitel, Wolfgang Buss, Mohsine Menouni, Fabien Expert, Raphael Juston, Michal Karol Dobrzynski, Geraud L'Eplattenier, Fabian Recktenwald, Hanspeter A Mallot, and Nicolas Franceschini. Miniature curved artificial compound eyes. *Proc. Natl. Acad. Sci. U. S. A.*, 110(23):9267–9272, June 2013.

[3] Subin Kang, Jaehong Lee, Sanggeun Lee, Seulgee Kim, Jae-Kang Kim, Hassan Algadi, Saleh Al-Sayari, Dae-Eun Kim, Daeeun Kim, and Taeyoon Lee. Highly sensitive pressure sensor based on bioinspired porous structure for real-time tactile sensing. *Adv. Electron. Mater.*, 2(12):1600356, December 2016.

[4] John D W Madden, Nathan A Vandesteeg, Patrick A Anquetil, Peter G A Madden, Arash Takshi, Rachel Z Pytel, Serge R Lafontaine, Paul A Wieringa, and Ian W Hunter. Artificial muscle technology: physical principles and naval prospects. *IEEE J. Oceanic Eng.*, 29(3):706–728, 2004.

[5] Auke Jan Ijspeert. Central pattern generators for locomotion control in animals and robots: a review. *Neural Netw.*, 21(4):642–653, May 2008.

[6] Kiyotoshi Matsuoka. Sustained oscillations generated by mutually inhibiting neurons with adaptation. *Biol. Cybern.*, 52(6):367–376, October 1985.

[7] N Kopell and G B Ermentrout. Coupled oscillators and the design of central pattern generators. *Math. Biosci.*, 90(1):87–109, July 1988.

[8] Thomas Graham Brown. The intrinsic factors in the act of progression in the mammal. *Proceedings of the Royal Society of London. Series B, containing papers of a biological character*, 84(572):308–319, 1911.

[9] Ole Kiehn and Simon J.B Butt. Physiological, anatomical and genetic identification of cpg neurons in the developing mammalian spinal cord. *Progress in Neurobiology*, 70(4):347–361, 2003.

[10] Quan Wen, Michelle D Po, Elizabeth Hulme, Sway Chen, Xinyu Liu, Sen Wai Kwok, Marc Gershow, Andrew M Leifer, Victoria Butler, Christopher Fang-Yen, Taizo Kawano, William R Schafer, George Whitesides, Matthieu Wyart, Dmitri B Chklovskii, Mei Zhen, and Aravinthan D T Samuel. Proprioceptive coupling within motor neurons drives c. elegans forward locomotion. *Neuron*, 76(4):750–761, November 2012.

[11] Hongfei Ji, Anthony D Fouad, Shelly Teng, Alice Liu, Pilar Alvarez-Illera, Bowen Yao, Zihao Li, Mr, and Christopher Fang-Yen. Phase response analyses support a relaxation oscillator model of locomotor rhythm generation in caenorhabditis elegans. *Elife*, 10, September 2021.

[12] H P Zhang, Avraham Be'er, E-L Florin, and Harry L Swinney. Collective motion and density fluctuations in bacterial colonies. *Proc. Natl. Acad. Sci. U. S. A.*, 107(31):13626–13630, August 2010.

[13] Andrey Sokolov, Igor S. Aranson, John O. Kessler, and Raymond E. Goldstein. Concentration dependence of the collective dynamics of swimming bacteria. *Phys. Rev. Lett.*, 98:158102, Apr 2007.

[14] Thomas S. Deisboeck and Iain D. Couzin. Collective behavior in cancer cell populations. *BioEssays*, 31(2):190–197, 2009.

[15] Előd Méhes and Tamas Vicsek. Collective motion of cells: from experiments to models. *Integrative biology*, 6(9):831–854, 2014.

[16] J Buhl, D J T Sumpter, I D Couzin, J J Hale, E Despland, E R Miller, and S J Simpson. From disorder to order in marching locusts. *Science*, 312(5778):1402–1406, June 2006.

[17] Sepideh Bazazi, Jerome Buhl, Joseph J Hale, Michael L Anstey, Gregory A Sword, Stephen J Simpson, and Iain D Couzin. Collective motion and cannibalism in locust migratory bands. *Current biology*, 18(10):735–739, 2008.

[18] Gil Ariel and Amir Ayali. Locust collective motion and its modeling. *PLOS Computational Biology*, 11(12):e1004522, 2015.

[19] Yael Katz, Kolbjørn Tunstrøm, Christos C Ioannou, Cristián Huepe, and Iain D Couzin. Inferring the structure and dynamics of interactions in schooling fish. *Proc. Natl. Acad. Sci. U. S. A.*, 108(46):18720–18725, November 2011.

[20] Kolbjørn Tunstrøm, Yael Katz, Christos C Ioannou, Cristián Huepe, Matthew J Lutz, and Iain D Couzin. Collective states, multistability and transitional behavior in schooling fish. *PLoS Comput. Biol.*, 9(2):e1002915, February 2013.

[21] Michele Ballerini, Nicola Cabibbo, Raphael Candelier, Andrea Cavagna, Evaristo Cisbani, Irene Giardina, Alberto Orlandi, Giorgio Parisi, Andrea Procaccini, Massimiliano Viale, and Vladimir Zdravkovic. Empirical investigation of starling flocks: a benchmark study in collective animal behaviour. *Animal behaviour*, 76(1):201–215, 2008.

[22] M Ballerini, N Cabibbo, R Candelier, A Cavagna, E Cisbani, I Giardina, V Lecomte, A Orlandi, G Parisi, A Procaccini, M Viale, and V Zdravkovic. Interaction ruling animal collective behavior depends on topological rather than metric distance: evidence from a field study. *Proc. Natl. Acad. Sci. U. S. A.*, 105(4):1232–1237, January 2008.

[23] Máté Nagy, Zsuzsa Akos, Dora Biro, and Tamás Vicsek. Hierarchical group dynamics in pigeon flocks. *Nature*, 464(7290):890–893, April 2010.

[24] Jesse L Silverberg, Matthew Bierbaum, James P Sethna, and Itai Cohen. Collective motion of humans in mosh and circle pits at heavy metal concerts. *Physical review letters*, 110(22):228701, 2013.

[25] William H Warren. Collective motion in human crowds. *Current directions in psychological science*, 27(4):232–240, 2018.

[26] Joel W Newbolt, Jun Zhang, and Leif Ristroph. Flow interactions between uncoordinated flapping swimmers give rise to group cohesion. *Proc. Natl. Acad. Sci. U. S. A.*, 116(7):2419–2424, February 2019.

[27] Alexander D Becker, Hassan Masoud, Joel W Newbolt, Michael Shelley, and Leif Ristroph. Hydrodynamic schooling of flapping swimmers. *Nat. Commun.*, 6:8514, October 2015.

[28] Steven J Portugal, Tatjana Y Hubel, Johannes Fritz, Stefanie Heese, Daniela Trobe, Bernhard Voelkl, Stephen Hailes, Alan M Wilson, and James R Usherwood. Upwash exploitation and downwash avoidance by flap phasing in ibis formation flight. *Nature*, 505(7483):399–402, January 2014.

[29] Liang Li, Máté Nagy, Jacob M Graving, Joseph Bak-Coleman, Guangming Xie, and Iain D Couzin. Vortex phase matching as a strategy for schooling in robots and in fish. *Nat. Commun.*, 11(1):5408, October 2020.

[30] Harry Moore, Katerina Dvoráková, Nicholas Jenkins, and William Breed. Exceptional sperm cooperation in the wood mouse. *Nature*, 418(6894):174–177, July 2002.

[31] J Elgeti, R G Winkler, and G Gompper. Physics of microswimmers—single particle motion and collective behavior: a review. *Rep. Prog. Phys.*, 78(5):056601, April 2015.

[32] Yingzi Yang, Jens Elgeti, and Gerhard Gompper. Cooperation of sperm in two dimensions: synchronization, attraction, and aggregation through hydrodynamic interactions. *Phys. Rev. E Stat. Nonlin. Soft Matter Phys.*, 78(6 Pt 1):061903, December 2008.

[33] Douglas R Brumley, Kirsty Y Wan, Marco Polin, and Raymond E Goldstein. Flagellar synchronization through direct hydrodynamic interactions. *Elife*, 3:e02750, July 2014.

[34] Kirsty Y Wan and Raymond E Goldstein. Coordinated beating of algal flagella is mediated by basal coupling. *Proc. Natl. Acad. Sci. U. S. A.*, 113(20):E2784–93, May 2016.

[35] Veikko F Geyer, Frank Jülicher, Jonathon Howard, and Benjamin M Friedrich. Cell-body rocking is a dominant mechanism for flagellar synchronization in a swimming alga. *Proc. Natl. Acad. Sci. U. S. A.*, 110(45):18058–18063, November 2013.

[36] Douglas R Brumley, Marco Polin, Timothy J Pedley, and Raymond E Goldstein. Hydrodynamic synchronization and metachronal waves on the surface of the colonial alga volvox carteri. *Phys. Rev. Lett.*, 109(26):268102, December 2012.

[37] Jihun Han and Charles S Peskin. Spontaneous oscillation and fluid-structure interaction of cilia. *Proc. Natl. Acad. Sci. U. S. A.*, 115(17):4417–4422, April 2018.

[38] William Gilpin, Matthew Storm Bull, and Manu Prakash. The multiscale physics of cilia and flagella. *Nature Reviews Physics*, 2(2):74–88, February 2020.

[39] Anand U Oza, Leif Ristroph, and Michael J Shelley. Lattices of hydrodynamically interacting flapping swimmers. *Phys. Rev. X*, 9(4):041024, November 2019.

[40] Raghunath Chelakkot, Michael F Hagan, and Arvind Gopinath. Synchronized oscillations, traveling waves, and jammed clusters induced by steric interactions in active filament arrays. *Soft Matter*, December 2020.

[41] Nick Gravish, Gregory Gold, Andrew Zangwill, Michael A D Goodisman, and Daniel I Goldman. Glass-like dynamics in confined and congested ant traffic. *Soft Matter*, 11(33):6552–6561, September 2015.

[42] J Aguilar, D Monaenkova, V Linevich, W Savoie, B Dutta, H-S Kuan, M D Betterton, M A D Goodisman, and D I Goldman. Collective clog control: Optimizing traffic flow in confined biological and robophysical excavation. *Science*, 361(6403):672–677, August 2018.

[43] Auke Jan Ijspeert, Alessandro Crespi, Dimitri Ryczko, and Jean-Marie Cabelguen. From swimming to walking with a salamander robot driven by a spinal cord model. *Science*, 315(5817):1416–1420, 2007.

[44] Jonas Buchli, Ludovic Righetti, and Auke Jan Ijspeert. Engineering entrainment and adaptation in limit cycle systems. *Biological Cybernetics*, 95(6):645–664, 2006.

[45] Steven H Strogatz. *Nonlinear Dynamics and Chaos: With Applications to Physics, Biology, Chemistry and Engineering*. Westview Press, 2000.

[46] Ludovic Righetti, Jonas Buchli, and Auke Jan Ijspeert. Adaptive frequency oscillators and applications. *The Open Cybernetics & Systemics Journal*, 3(1), 2009.

[47] Steven Ceron, Marta An Kimmel, Alexandra Nilles, and Kirstin Hagelskjaer Petersen. Soft robotic oscillators with Strain-Based coordination. *IEEE Robotics and Automation Letters*, pages 1–1, 2021.

[48] Melanie Jouaiti and Patrick Hénaff. Comparative study of forced oscillators for the adaptive generation of rhythmic movements in robot controllers. *Biol. Cybern.*, 113(5-6):547–560, December 2019.

[49] Sourav Dutta, Abhinav Parihar, Abhishek Khanna, Jorge Gomez, Wriddhi Chakraborty, Matthew Jerry, Benjamin Grisafe, Arijit Raychowdhury, and Suman Datta. Programmable coupled oscillators for synchronized locomotion. *Nat. Commun.*, 10(1):3299, July 2019.

[50] M Garcia, A Chatterjee, A Ruina, and M Coleman. The simplest walking model: stability, complexity, and scaling. *J. Biomech. Eng.*, 120(2):281–288, April 1998.

[51] Fumihiko Asano. Efficiency and optimality of Two-Period limit cycle walking. *Adv. Robot.*, 26(1-2):155–176, January 2012.

[52] Joseph H Solomon, Martijn Wisse, and Mitra J Z Hartmann. Fully interconnected, linear control for limit cycle walking. *Adapt. Behav.*, 18(6):492–506, December 2010.

[53] Ludovic Righetti, Jonas Buchli, and Auke Jan Ijspeert. Dynamic hebbian learning in adaptive frequency oscillators. *Physica D: Nonlinear Phenomena*, 216(2):269–281, 2006.

[54] Arkady Pikovsky, Jurgen Kurths, Michael Rosenblum, and Jürgen Kurths. *Synchronization: A Universal Concept in Nonlinear Sciences*. Cambridge University Press, April 2003.

[55] Yoshiki Kuramoto. *Chemical Oscillations, Waves, and Turbulence*. Springer, Berlin, Heidelberg, 1984.

[56] J A Acebron, L L Bonilla, C J P Vicente, F Ritort, and R Spigler. The kuramoto model: A simple paradigm for synchronization phenomena. *Rev. Mod. Phys.*, 77(1):137–185, January 2005.

[57] R M N Alexander. *Principles of Animal Locomotion*. Princeton University Press, 2003.

[58] B Dadashzadeh, H R Vejdani, and J Hurst. From template to anchor: A novel control strategy for spring-mass running of bipedal robots. In *2014 IEEE/RSJ International Conference on Intelligent Robots and Systems*, pages 2566–2571, 2014.

[59] D Renjewski, A Spröwitz, A Peekema, M Jones, and J Hurst. Exciting engineered passive dynamics in a bipedal robot. *IEEE Trans. Rob.*, 31(5):1244–1251, October 2015.

[60] Kevin Y Ma, Pakpong Chirarattananon, Sawyer B Fuller, and Robert J Wood. Controlled flight of a biologically inspired, insect-scale robot. *Science*, 340(6132):603–607, May 2013.

[61] Eric Chang, Laura Y Matloff, Amanda K Stowers, and David Lentink. Soft biohybrid morphing wings with feathers underactuated by wrist and finger motion. *Science Robotics*, 5(38), January 2020.

[62] Matteo Di Luca, Stefano Mintchev, Yunxing Su, Eric Shaw, and Kenneth Breuer. A bioinspired separated flow wing provides turbulence resilience and aerodynamic efficiency for miniature drones. *Science Robotics*, 5(38), January 2020.

[63] Hamidreza Marvi, Chaohui Gong, Nick Gravish, Henry Astley, Matthew Travers, Ross L Hatton, Joseph R Mendelson, 3rd, Howie Choset, David L Hu, and Daniel I Goldman. Sidewinding with minimal slip: snake and robot ascent of sandy slopes. *Science*, 346(6206):224–229, October 2014.

[64] Henry C Astley, Chaohui Gong, Jin Dai, Matthew Travers, Miguel M Serrano, Patricio A Vela, Howie Choset, Joseph R Mendelson, 3rd, David L Hu, and Daniel I Goldman. Modulation of orthogonal body waves enables high maneuverability in sidewinding locomotion. *Proc. Natl. Acad. Sci. U. S. A.*, 112(19):6200–6205, May 2015.

[65] Benjamin Goldberg, Neel Doshi, Kaushik Jayaram, and Robert J Wood. Gait studies for a quadrupedal microrobot reveal contrasting running templates in two frequency regimes. *Bioinspir. Biomim.*, 12(4):046005, June 2017.

[66] John Brackenbury. Fast locomotion in caterpillars. *Journal of Insect Physiology*, 45(6):525–533, 1999.

[67] Kim J Quillin. Kinematic scaling of locomotion by hydrostatic animals: ontogeny of peristaltic crawling by the earthworm lumbricus terrestris. *Journal of Experimental Biology*, 202(6):661–674, 1999.

[68] Stephen T Tettelbach, James R Europe, Christian R H Tettelbach, Jason Havelin, Brooke S Rodgers, Bradley T Furman, and Marissa Velasquez. Hard clam walking: Active horizontal locomotion of adult mercenaria mercenaria at the sediment surface and behavioral suppression after extensive sampling. *PLoS One*, 12(3):e0173626, March 2017.

[69] O Ellers. Form and motion of donax variabilis in flow. *Biol. Bull.*, 189(2):138–147, October 1995.

[70] Bruce C Jayne. Kinematics of terrestrial snake locomotion. *Copeia*, pages 915–927, 1986.

[71] Byungkyu Kim, Moon Gu Lee, Young Pyo Lee, YongIn Kim, and GeunHo Lee. An earthworm-like micro robot using shape memory alloy actuator. *Sensors and Actuators A: Physical*, 125(2):429–437, 2006.

[72] Jinwan Lim, Hyunjun Park, Jaemin An, Yeh-Sun Hong, Byungkyu Kim, and Byung-Ju Yi. One pneumatic line based inchworm-like micro robot for half-inch pipe inspection. *Mechatronics*, 18(7):315–322, 2008.

[73] Je-Sung Koh and Kyu-Jin Cho. Omegabot: Crawling robot inspired by ascotis selenaria. In *2010 IEEE International Conference on Robotics and Automation*, pages 109–114. IEEE, 2010.

[74] Dongwoo Lee, Sinbae Kim, Yong-Lae Park, and Robert J Wood. Design of centimeter-scale inchworm robots with bidirectional claws. In *2011 IEEE International Conference on Robotics and Automation*, pages 3197–3204. IEEE, 2011.

[75] Mikołaj Rogóż, Hao Zeng, Chen Xuan, Diederik Sybolt Wiersma, and Piotr Wasylczyk. Light-driven soft robot mimics caterpillar locomotion in natural scale. *Advanced Optical Materials*, 4(11):1689–1694, 2016.

[76] K Zimmermann, I Zeidis, M Pivovarov, and K Abaza. Forced nonlinear oscillator with nonsymmetric dry friction. *Archive of Applied Mechanics*, 77(5):353–362, 2007.

[77] Gregory L Wagner and Eric Lauga. Crawling scallop: Friction-based locomotion with one degree of freedom. *Journal of theoretical biology*, 324:42–51, 2013.

[78] N Bolotnik, M Pivovarov, I Zeidis, and K Zimmermann. The motion of a two-body limbless locomotor along a straight line in a resistive medium. *ZAMM-Journal of Applied Mathematics and Mechanics/Zeitschrift für Angewandte Mathematik und Mechanik*, 96(4):429–452, 2016.

[79] Ziyou Wu, Dan Zhao, and Shai Revzen. Coulomb friction crawling model yields linear force–velocity profile. *Journal of Applied Mechanics*, 86(5):054501, 2019.

[80] T Umedachi and B A Trimmer. Design of a 3d-printed soft robot with posture and steering control. In *2014 IEEE International Conference on Robotics and Automation (ICRA)*, pages 2874–2879, May 2014.

[81] Raymond H Plaut. Mathematical model of inchworm locomotion. *Int. J. Non Linear Mech.*, 76:56–63, November 2015.

[82] Je-Sung Koh and Kyu-Jin Cho. Omega-Shaped Inchworm-Inspired crawling robot with Large-Index-and-Pitch (LIP) SMA spring actuators. *Ieee-Asme Transactions on Mechatronics*, 18(2):419–429, April 2013.

[83] P Gidoni, G Noselli, and A DeSimone. Crawling on directional surfaces. *Int. J. Non Linear Mech.*, 61:65–73, May 2014.

[84] Hamidreza Marvi, Gregory Meyers, Geoffrey Russell, and David L Hu. Scalybot: A Snake-Inspired robot with active control of friction. In *ASME 2011 Dynamic Systems and Control Conference and Bath/ASME Symposium on Fluid Power and Motion Control*, pages 443–450. American Society of Mechanical Engineers Digital Collection, May 2012.

[85] Ahmad Rafsanjani, Yuerou Zhang, Bangyuan Liu, Shmuel M Rubinstein, and Katia Bertoldi. Kirigami skins make a simple soft actuator crawl. *Science Robotics*, 3(15):eaar7555, February 2018.

[86] Yoshimi Tanaka, Kentaro Ito, Toshiyuki Nakagaki, and Ryo Kobayashi. Mechanics of peristaltic locomotion and role of anchoring. *J. R. Soc. Interface*, 9(67):222–233, February 2012.

[87] B Liu, Y Ozkan-Aydin, D I Goldman, and F L Hammond. Kirigami skin improves soft earthworm robot anchoring and locomotion under cohesive soil. In *2019 2nd IEEE International Conference on Soft Robotics (RoboSoft)*, pages 828–833, April 2019.

[88] D L Christensen, S A Suresh, K Hahm, and M R Cutkosky. Let's all pull together: Principles for sharing large loads in microrobot teams. *IEEE Robotics and Automation Letters*, 1(2):1089–1096, July 2016.

[89] David L Hu, Jasmine Nirody, Terri Scott, and Michael J Shelley. The mechanics of slithering locomotion. *Proc. Natl. Acad. Sci. U. S. A.*, 106(25):10081–10085, June 2009.

[90] Tadeusz Majewski, Dariusz Szwedowicz, and Maciej Majewski. Locomotion of a mini bristle robot with inertial excitation. *J. Mech. Robot.*, 9(6):061008, December 2017.

[91] Yuanfeng Han, H Marvi, and M Sitti. Fiberbot: A miniature crawling robot using a directional fibrillar pad. In *2015 IEEE International Conference on Robotics and Automation (ICRA)*, pages 3122–3127. ieeexplore.ieee.org, May 2015.

[92] Z Shen, Y Liu, J Zhao, X Tang, and W Chen. Design and experiment of a small legged robot operated by the resonant vibrations of cantilever beams. *IEEE Access*, 5:8451–8458, 2017.

[93] Zhouwei Du, Hongbin Fang, Xiong Zhan, and Jian Xu. Experiments on vibration-driven stick-slip locomotion: A sliding bifurcation perspective. *Mech. Syst. Signal Process.*, 105:261–275, May 2018.

[94] Joey Z Ge, Ariel A Calderón, Longlong Chang, and Néstor O Pérez-Arancibia. An earthworm-inspired friction-controlled soft robot capable of bidirectional locomotion. *Bioinspir. Biomim.*, 14(3):036004, February 2019.

[95] T Umedachi, V Vikas, and B A Trimmer. Softworms: the design and control of non-pneumatic, 3d-printed, deformable robots. *Bioinspir. Biomim.*, 11(2):025001, March 2016.

[96] T Umedachi, V Vikas, and B A Trimmer. Highly deformable 3-D printed soft robot generating inching and crawling locomotions with variable friction legs. In *2013 IEEE/RSJ International Conference on Intelligent Robots and Systems*, pages 4590–4595, November 2013.

[97] Robert F Shepherd, Filip Ilievski, Wonjae Choi, Stephen A Morin, Adam A Stokes, Aaron D Mazzeo, Xin Chen, Michael Wang, and George M Whitesides. Multigait soft robot. *Proc. Natl. Acad. Sci. U. S. A.*, 108(51):20400–20403, December 2011.

[98] Benny Gamus, Lior Salem, Amir D Gat, and Yizhar Or. Understanding inchworm crawling for Soft-Robotics. *Ieee Robotics and Automation Letters*, 5(2):1397–1404, 2020.

[99] Di Guo and Zhan Kang. Chamber layout design optimization of soft pneumatic robots. *Smart Mater. Struct.*, 29(2), 2020.

[100] Xiaonan Huang, Michael Ford, Zach J Patterson, Masoud Zarepoor, Chengfeng Pan, and Carmel Majidi. Shape memory materials for electrically-powered soft machines. *J. Mater. Chem. B Mater. Biol. Med.*, 8(21):4539–4551, June 2020.

[101] S Seok, C D Onal, R Wood, D Rus, and S Kim. Peristaltic locomotion with antagonistic actuators in soft robotics. In *2010 IEEE International Conference on Robotics and Automation*, pages 1228–1233, May 2010.

[102] Yuuta Sugiyama and Shinichi Hirai. Crawling and jumping by a deformable robot. *Int. J. Rob. Res.*, 25(5-6):603–620, 2006.

[103] M Duduta, F Berlinger, R Nagpal, D R Clarke, R J Wood, and F Z Temel. Tunable Multi-Modal locomotion in soft dielectric elastomer robots. *IEEE Robotics and Automation Letters*, 5(3):3868–3875, July 2020.

[104] Sascha Pfeil, Markus Henke, Konrad Katzer, Martina Zimmermann, and Gerald Gerlach. A Worm-Like biomimetic crawling robot based on cylindrical dielectric elastomer actuators. *Frontiers in Robotics and Ai*, 7, 2020.

[105] Jinhua Zhang, Tao Wang, Jin Wang, Baotong Li, Jun Hong, John X J Zhang, and Michael Yu Wang. Dynamic modeling and simulation of inchworm movement towards bio-inspired soft robot design. *Bioinspir. Biomim.*, 14(6):066012, September 2019.

[106] Daniela Rus and Michael T Tolley. Design, fabrication and control of soft robots. *Nature*, 521(7553):467, 2015.

[107] J P Whitney, P S Sreetharan, K Y Ma, and R J Wood. Pop-up book MEMS. *J. Micromech. Microeng.*, 21(11):115021, 2011.

[108] Noah T Jafferis, Michael J Smith, and Robert J Wood. Design and manufacturing rules for maximizing the performance of polycrystalline piezoelectric bending actuators. *Smart Mater. Struct.*, 24(6):065023, 2015.

[109] Andrew T Baisch, Onur Ozcan, Benjamin Goldberg, Daniel Ithier, and Robert J Wood. High speed locomotion for a quadrupedal microrobot. *Int. J. Rob. Res.*, 33(8):1063–1082, July 2014.

[110] N Doshi, B Goldberg, R Sahai, N Jafferis, D Aukes, R J Wood, and J A Paulson. Model driven design for flexure-based microrobots. In *Intelligent Robots and Systems (IROS), 2015 IEEE/RSJ International Conference on*, pages 4119–4126, 2015.

[111] B Goldberg, M Karpelson, O Ozcan, and R J Wood. Planar fabrication of a mesoscale voice coil actuator. In *2014 IEEE International Conference on Robotics and Automation (ICRA)*, pages 6319–6325, May 2014.

[112] P A York and R J Wood. A geometrically-amplified in-plane piezoelectric actuator for mesoscale robotic systems. In *2017 IEEE International Conference on Robotics and Automation (ICRA)*, pages 1263–1268, May 2017.

[113] Peter A York and Robert J Wood. A geometrically-amplified in-plane piezoelectric actuator for mesoscale robotic systems. In *2017 IEEE International Conference on Robotics and Automation (ICRA)*, pages 1263–1268. IEEE, 2017.

[114] RJ Wood, E Steltz, and RS Fearing. Optimal energy density piezoelectric bending actuators. *Sensors and Actuators A: Physical*, 119(2):476–488, 2005.

[115] Giovanni Noselli and Antonio DeSimone. A robotic crawler exploiting directional frictional interactions: experiments, numerics and derivation of a reduced model. *Proceedings of the Royal Society A: Mathematical, Physical and Engineering Sciences*, 470(2171):20140333, November 2014.

[116] Noah T Jafferis, Mario Lok, Nastasia Winey, Gu-Yeon Wei, and Robert J Wood. Multilayer laminated piezoelectric bending actuators: design and manufacturing for optimum power density and efficiency. *Smart Mater. Struct.*, 25(5):055033, 2016.

[117] Michael Karpelson, Gu-Yeon Wei, and Robert J Wood. Driving high voltage piezoelectric actuators in microrobotic applications. *Sens. Actuators A Phys.*, 176:78–89, April 2012.

[118] P A York, N T Jafferis, and R J Wood. Meso scale flextensional piezoelectric actuators. *Smart Mater. Struct.*, 2017.

[119] R Malka, A L Desbiens, Y Chen, and others. Principles of microscale flexure hinge design for enhanced endurance. *2014 IEEE/RSJ*, 2014.

[120] Nicolae Lobontiu and Ephrahim Garcia. Analytical model of displacement amplification and stiffness optimization for a class of flexure-based compliant mechanisms. *Computers & structures*, 81(32):2797–2810, 2003.

[121] Hong-Wen Ma, Shao-Ming Yao, Li-Quan Wang, and Zhi Zhong. Analysis of the displacement amplification ratio of bridge-type flexure hinge. *Sensors and Actuators A: Physical*, 132(2):730–736, 2006.

[122] Qingsong Xu and Yangmin Li. Analytical modeling, optimization and testing of a compound bridge-type compliant displacement amplifier. *Mechanism and machine theory*, 46(2):183–200, 2011.

[123] Robert J Wood, Srinath Avadhanula, Ranjana Sahai, Erik Steltz, and Ronald S Fearing. Microrobot design using fiber reinforced composites. *Journal of Mechanical Design*, 130(5):052304, 2008.

[124] Pratheev S Sreetharan, John P Whitney, Mark D Strauss, and Robert J Wood. Monolithic fabrication of millimeter-scale machines. *Journal of Micromechanics and Microengineering*, 22(5):055027, 2012.

[125] Alan T Asbeck, Sangbae Kim, Mark R Cutkosky, William R Provancher, and Michele Lanzetta. Scaling hard vertical surfaces with compliant microspine arrays. *The International Journal of Robotics Research*, 25(12):1165–1179, 2006.

[126] Tyson L Hedrick. Software techniques for two-and three-dimensional kinematic measurements of biological and biomimetic systems. *Bioinspiration & biomimetics*, 3(3):034001, 2008.

[127] Zhendong Dai, Stanislav N Gorb, and Uli Schwarz. Roughness-dependent friction force of the tarsal claw system in the beetle pachnoda marginata (coleoptera, scarabaeidae). *J. Exp. Biol.*, 205(Pt 16):2479–2488, August 2002.

[128] Matthew A Woodward and Metin Sitti. Morphological intelligence counters foot slipping in the desert locust and dynamic robots. *Proc. Natl. Acad. Sci. U. S. A.*, 115(36):E8358–E8367, September 2018.

[129] Dan Zhao and Shai Revzen. Multi-legged steering and slipping with low DoF hexapod robots. *Bioinspir. Biomim.*, March 2020.

[130] J Carius, R Ranftl, V Koltun, and M Hutter. Trajectory optimization for legged robots with slipping motions. *IEEE Robotics and Automation Letters*, 4(3):3013–3020, July 2019.

[131] Hongbin Fang and Jian Xu. Stick-Slip effect in a Vibration-Driven system with dry friction: Sliding bifurcations and optimization. *J. Appl. Mech.*, 81(5), May 2014.

[132] Yichuan Wu, Justin K Yim, Jiaming Liang, Zhichun Shao, Mingjing Qi, Junwen Zhong, Zihao Luo, Xiaojun Yan, Min Zhang, Xiaohao Wang, Ronald S Fearing, Robert J Full, and Liwei Lin. Insect-scale fast moving and ultrarobust soft robot. *Science Robotics*, 4(32), July 2019.

[133] Jake J Abbott, Zoltan Nagy, Felix Beyeler, and Bradley J Nelson. Robotics in the small, part i: microbotics. *IEEE Robotics & Automation Magazine*, 14(2):92–103, 2007.

[134] Samuel Felton, Michael Tolley, Erik Demaine, Daniela Rus, and Robert Wood. A method for building self-folding machines. *Science*, 345(6197):644–646, 2014.

[135] Jeremy M Morrey, Bram Lambrecht, Andrew D Horchler, Roy E Ritzmann, and Roger D Quinn. Highly mobile and robust small quadruped robots. In *Proceedings 2003 IEEE/RSJ International Conference on Intelligent Robots and Systems (IROS 2003)(Cat. No. 03CH37453)*, volume 1, pages 82–87. IEEE, 2003.

[136] Aaron M Hoover, Erik Steltz, and Ronald S Fearing. Roach: An autonomous 2.4 g crawling hexapod robot. In *2008 IEEE/RSJ International Conference on Intelligent Robots and Systems*, pages 26–33. IEEE, 2008.

[137] Andrew T Baisch, Christian Heimlich, Michael Karpelson, and Robert J Wood. Hamr3: An autonomous 1.7 g ambulatory robot. In *2011 IEEE/RSJ International Conference on Intelligent Robots and Systems*, pages 5073–5079. IEEE, 2011.

[138] Haojian Lu, Mei Zhang, Yuanyuan Yang, Qiang Huang, Toshio Fukuda, Zuankai Wang, and Yajing Shen. A bioinspired multilegged soft millirobot that functions in both dry and wet conditions. *Nature communications*, 9(1):1–7, 2018.

[139] Dominic R Frutiger, Karl Vollmers, Bradley E Kratochvil, and Bradley J Nelson. Small, fast, and under control: wireless resonant magnetic micro-agents. *The International Journal of Robotics Research*, 29(5):613–636, 2010.

[140] Hsi-Wen Tung, Massimo Maffioli, Dominic R Frutiger, Kartik M Sivaraman, Salvador Pané, and Bradley J Nelson. Polymer-based wireless resonant magnetic microrobots. *IEEE Transactions on Robotics*, 30(1):26–32, 2013.

[141] Ryan St Pierre, Noah Paul, and Sarah Bergbreiter. 3dflex: A rapid prototyping approach for multi-material compliant mechanisms in millirobots. In *2017 IEEE International Conference on Robotics and Automation (ICRA)*, pages 3068–3073. IEEE, 2017.

[142] Ryan St Pierre, Walker Gosrich, and Sarah Bergbreiter. A 3d-printed 1 mg legged microrobot running at 15 body lengths per second. 3, 2018.

[143] Robert J Wood. Design, fabrication, and analysis of a 3dof, 3cm flapping-wing mav. In *2007 IEEE/RSJ international conference on intelligent robots and systems*, pages 1576–1581. IEEE, 2007.

[144] Cagdas D Onal, Robert J Wood, and Daniela Rus. An origami-inspired approach to worm robots. *IEEE/ASME Transactions on Mechatronics*, 18(2):430–438, 2012.

[145] Shuhei Miyashita, Steven Guitron, Marvin Ludersdorfer, Cynthia R Sung, and Daniela Rus. An untethered miniature origami robot that self-folds, walks, swims, and degrades. In *2015 IEEE International Conference on Robotics and Automation (ICRA)*, pages 1490–1496. IEEE, 2015.

[146] Wenqi Hu, Guo Zhan Lum, Massimo Mastrangeli, and Metin Sitti. Small-scale soft-bodied robot with multimodal locomotion. *Nature*, 554(7690):81, 2018.

[147] Ernesto Altshuler, Jose Martin Pastor, Angel Garcimartín, Iker Zuriguel, and Diego Maza. Vibrot, a simple device for the conversion of vibration into rotation mediated by friction: preliminary evaluation. *PloS one*, 8(8), 2013.

[148] Felix Becker, Simon Boerner, Victor Lysenko, Igor Zeidis, and Klaus Zimmermann. On the mechanics of bristle-bots-modeling, simulation and experiments. In *ISR/Robotik 2014; 41st international symposium on robotics*, pages 1–6. VDE, 2014.

[149] Cecilia Laschi, Barbara Mazzolai, and Matteo Cianchetti. Soft robotics: Technologies and systems pushing the boundaries of robot abilities. *Sci. Robot*, 1(1):eaah3690, 2016.

[150] Mingxiang Ling, Junyi Cao, Minghua Zeng, Jing Lin, and Daniel J Inman. Enhanced mathematical modeling of the displacement amplification ratio for piezoelectric compliant mechanisms. *Smart Materials and Structures*, 25(7):075022, 2016.

[151] Tamás Vicsek and Anna Zafeiris. Collective motion. *Phys. Rep.*, 517(3–4):71–140, August 2012.

[152] Sriram Ramaswamy. The mechanics and statistics of active matter. *Annu. Rev. Condens. Matter Phys.*, 1(1):323–345, August 2010.

[153] Avraham Be'er and Gil Ariel. A statistical physics view of swarming bacteria. *Mov Ecol*, 7:9, March 2019.

[154] Douglas H Kelley and Nicholas T Ouellette. Emergent dynamics of laboratory insect swarms. *Sci. Rep.*, 3:1073, January 2013.

[155] Michele Castellana, William Bialek, Andrea Cavagna, and Irene Giardina. Entropic effects in a nonequilibrium system: Flocks of birds. *Phys Rev E*, 93(5):052416, May 2016.

[156] Andrea Cavagna, Alessio Cimarelli, Irene Giardina, Giorgio Parisi, Raffaele Santagati, Fabio Stefanini, and Massimiliano Viale. Scale-free correlations in starling flocks. *Proc. Natl. Acad. Sci. U. S. A.*, 107(26):11865–11870, June 2010.

[157] M Reza Shaebani, Adam Wysocki, Roland G Winkler, Gerhard Gompper, and Heiko Rieger. Computational models for active matter. *Nature Reviews Physics*, 2(4):181–199, April 2020.

[158] Julien Deseigne, Olivier Dauchot, and Hugues Chaté. Collective motion of vibrated polar disks. *Phys. Rev. Lett.*, 105(9):098001, August 2010.

[159] Igor S Aranson, Dmitri Volfson, and Lev S Tsimring. Swirling motion in a system of vibrated elongated particles. *Phys. Rev. E Stat. Nonlin. Soft Matter Phys.*, 75(5 Pt 1):051301, May 2007.

[160] Arshad Kudrolli, Geoffroy Lumay, Dmitri Volfson, and Lev S Tsimring. Swarming and swirling in self-propelled polar granular rods. *Phys. Rev. Lett.*, 100(5):058001, February 2008.

[161] Markus Bär, Robert Großmann, Sebastian Heidenreich, and Fernando Peruani. Self-Propelled rods: Insights and perspectives for active matter. *Annual Review of Condensed Matter Physics*, March 2020.

[162] Antoine Bricard, Jean-Baptiste Caussin, Nicolas Desreumaux, Olivier Dauchot, and Denis Bartolo. Emergence of macroscopic directed motion in populations of motile colloids. *Nature*, 503(7474):95–98, November 2013.

[163] Francesco Ginelli, Fernando Peruani, Markus Bär, and Hugues Chaté. Large-scale collective properties of self-propelled rods. *Phys. Rev. Lett.*, 104(18):184502, May 2010.

[164] Gao Wang, Trung V Phan, Shengkai Li, Michael Wombacher, Junle Qu, Yan Peng, Guo Chen, Daniel I Goldman, Simon A Levin, Robert H Austin, and Liyu Liu. Emergent Field-Driven robot swarm states. *Phys. Rev. Lett.*, 126(10):108002, March 2021.

[165] Alexandre Campo, Alvaro Gutiérrez, Shervin Nouyan, Carlo Pinciroli, Valentin Longchamp, Simon Garnier, and Marco Dorigo. Artificial pheromone for path selection by a foraging swarm of robots. *Biol. Cybern.*, 103(5):339–352, November 2010.

[166] T Vicsek, A Czirók, E Ben-Jacob, I Cohen, I, and O Shochet. Novel type of phase transition in a system of self-driven particles. *Phys. Rev. Lett.*, 75(6):1226–1229, August 1995.

[167] E A Gaffney, H Gadêlha, D J Smith, J R Blake, and J C Kirkman-Brown. Mammalian sperm motility: Observation and theory. *Annual Review of*, January 2011.

[168] J Gray and H W Lissmann. The kinetics of locomotion of the Grass-Snake. *J. Exp. Biol.*, 26(4):354–367, February 1950.

[169] Z V Guo and L Mahadevan. Limbless undulatory propulsion on land. *Proc. Natl. Acad. Sci. U. S. A.*, 105(9):3179–3184, March 2008.

[170] E M Purcell. Life at low reynolds number. *Am. J. Phys.*, 45(1):3–11, January 1977.

[171] L E Becker, S A Koehler, and H A Stone. On self-propulsion of micro-machines at low reynolds number: Purcell's three-link swimmer. *J. Fluid Mech.*, 490:15–35, September 2003.

[172] Fangxu Jing and Silas Alben. Optimization of two- and three-link snakelike locomotion. *Phys. Rev. E Stat. Nonlin. Soft Matter Phys.*, 87(2):022711, February 2013.

[173] Silas Alben. Efficient sliding locomotion of three-link bodies. *Phys. Rev. E*, 103(4):042414, April 2021.

[174] Ross L Hatton, Yang Ding, Howie Choset, and Daniel I Goldman. Geometric visualization of Self-Propulsion in a complex medium. *Phys. Rev. Lett.*, 110(7):078101, February 2013.

[175] Daniel Tam and A E Hosoi. Optimal stroke patterns for purcell's three-link swimmer. *Phys. Rev. Lett.*, 98(6):068105, February 2007.

[176] O Wiezel and Y Or. Optimization and small-amplitude analysis of purcell's three-link microswimmer model. *Proceedings of the Royal Society A: Mathematical, Physical and Engineering Sciences*, 472(2192):20160425, August 2016.

[177] Jennifer M Rieser, Chaohui Gong, Henry C Astley, Perrin E Schiebel, Ross L Hatton, Howie Choset, and Daniel I Goldman. Geometric phase and dimensionality reduction in locomoting living systems. *arXiv preprint arXiv:1906.11374*, June 2019.

[178] Jennifer M Rieser, Perrin E Schiebel, Arman Pazouki, Feifei Qian, Zachary Goddard, Kurt Wiesenfeld, Andrew Zangwill, Dan Negrut, and Daniel I Goldman. Dynamics of scattering in undulatory active collisions. *Phys Rev E*, 99(2-1):022606, February 2019.

[179] Vasily Kantsler, Jörn Dunkel, Marco Polin, and Raymond E Goldstein. Ciliary contact interactions dominate surface scattering of swimming eukaryotes. *Proc. Natl. Acad. Sci. U. S. A.*, 110(4):1187–1192, January 2013.

[180] G Juarez, K Lu, J Sznitman, and others. Motility of small nematodes in wet granular media. *EPL (Europhysics Letters*, 2010.

[181] Sungsu Park, Hyejin Hwang, Seong-Won Nam, Fernando Martinez, Robert H Austin, and William S Ryu. Enhanced caenorhabditis elegans locomotion in a structured microfluidic environment. *PLoS One*, 3(6):e2550, June 2008.

[182] Jinzhou Yuan, David M Raizen, and Haim H Bau. Gait synchronization in caenorhabditis elegans. *Proc. Natl. Acad. Sci. U. S. A.*, 111(19):6865–6870, May 2014.

[183] Anton Peshkov, Sonia McGaffigan, and Alice C Quillen. Wiggling droplets: metachronal waves in populations of turbatrix aceti. *preprint https://arxiv.org/abs/2104.10316*, April 2021.

[184] A. C. Quillen, A. Peshkov, Esteban Wright, and Sonia McGaffigan. Metachronal waves in concentrations of swimming turbatrix aceti nematodes and an oscillator chain model for their coordinated motions. *Phys. Rev. E*, 104:014412, Jul 2021.

[185] Simone Immler, Harry D M Moore, William G Breed, and Tim R Birkhead. By hook or by crook? morphometry, competition and cooperation in rodent sperm. *PLoS One*, 2(1):e170, January 2007.

[186] Yingzi Yang, Vincent Marceau, and Gerhard Gompper. Swarm behavior of self-propelled rods and swimming flagella. *Phys. Rev. E Stat. Nonlin. Soft Matter Phys.*, 82(3 Pt 1):031904, September 2010.

[187] Raymond E Goldstein, Marco Polin, and Idan Tuval. Noise and synchronization in pairs of beating eukaryotic flagella. *Phys. Rev. Lett.*, 103(16):168103, October 2009.

[188] Douglas R Brumley, Nicolas Bruot, Jurij Kotar, Raymond E Goldstein, Pietro Cicuta, and Marco Polin. Long-range interactions, wobbles, and phase defects in chains of model cilia. *Phys Rev Fluids*, 1:081201, December 2016.

[189] Hanliang Guo, Lisa Fauci, Michael Shelley, and Eva Kanso. Bistability in the synchronization of actuated microfilaments. *J. Fluid Mech.*, 836:304–323, February 2018.

[190] Jurij Kotar, Marco Leoni, Bruno Bassetti, Marco Cosentino Lagomarsino, and Pietro Cicuta. Hydrodynamic synchronization of colloidal oscillators. *Proc. Natl. Acad. Sci. U. S. A.*, 107(17):7669–7673, April 2010.

[191] Shang Yik Reigh, Roland G Winkler, and Gerhard Gompper. Synchronization and bundling of anchored bacterial flagella. *Soft Matter*, 8(16):4363–4372, March 2012.

[192] Yasemin Ozkan-Aydin, Daniel I Goldman, and M Saad Bhamla. Collective dynamics in entangled worm and robot blobs. *Proceedings of the National Academy of Sciences*, 118(6), 2021.

[193] Alessandro Tasora, Radu Serban, Hammad Mazhar, Arman Pazouki, Daniel Melanz, Jonathan Fleischmann, Michael Taylor, Hiroyuki Sugiyama, and Dan Negrut. Chrono: An open source multi-physics dynamics engine. In *High Performance Computing in Science and Engineering*, pages 19–49. Springer International Publishing, 2016.

[194] Arman Pazouki, Michał Kwarta, Kyle Williams, William Likos, Radu Serban, Paramsothy Jayakumar, and Dan Negrut. Compliant contact versus rigid contact: A comparison in the context of granular dynamics. *Phys Rev E*, 96(4-1):042905, October 2017.

[195] Toby Heyn, Dan Negrut, Mihai Anitescu, Alessandro Tasora, and David Lamb. On the numerical solution of Many-Body contact dynamics problems formulated as complementarity problems. In *ASME 2012 International Design Engineering Technical Conferences and Computers and Information in Engineering Conference*, pages 61–69. American Society of Mechanical Engineers Digital Collection, September 2013.

[196] Ross L. Hatton and Howie Choset. Geometric swimming at low and high reynolds numbers. *IEEE Transactions on Robotics*, 29(3):615–624, 2013.

[197] Vijay Narayan, Sriram Ramaswamy, and Narayanan Menon. Long-lived giant number fluctuations in a swarming granular nematic. *Science*, 317(5834):105–108, July 2007.

[198] Gwynn J Elfring and Eric Lauga. Hydrodynamic phase locking of swimming microorganisms. *Phys. Rev. Lett.*, 103(8):088101, August 2009.

[199] Sina Heydari and Eva Kanso. School cohesion, speed, and efficiency are modulated by the swimmers flapping motion. *Journal of Fluid Mechanics*, 922:A27, 2021.

[200] Sophie Ramananarivo, Fang Fang, Anand Oza, Jun Zhang, and Leif Ristroph. Flow interactions lead to orderly formations of flapping wings in forward flight. *Phys. Rev. Fluids*, 1(7):071201, November 2016.

[201] Tuhin Chakrabortty, Akash Suman, Anjali Gupta, Varsha Singh, and Manoj Varma. Null model exhibiting synchronized dynamics in uncoupled oscillators. *Phys Rev E*, 99(5-1):052410, May 2019.

[202] William Savoie, Thomas A Berrueta, Zachary Jackson, Ana Pervan, Ross Warkentin, Shengkai Li, Todd D Murphey, Kurt Wiesenfeld, and Daniel I Goldman. A robot made of robots: Emergent transport and control of a smarticle ensemble. *Science Robotics*, 4(34), September 2019.

[203] Shuguang Li, Richa Batra, David Brown, Hyun-Dong Chang, Nikhil Ranganathan, Chuck Hoberman, Daniela Rus, and Hod Lipson. Particle robotics based on statistical mechanics of loosely coupled components. *Nature*, 567(7748):361–365, March 2019.

[204] Jungwon Seo, Jamie Paik, and Mark Yim. Modular reconfigurable robotics. *Annual Review of Control, Robotics, and Autonomous Systems*, May 2019.

[205] Manuele Brambilla, Eliseo Ferrante, Mauro Birattari, and Marco Dorigo. Swarm robotics: a review from the swarm engineering perspective. *Swarm Intelligence*, 7(1):1–41, March 2013.

[206] Michel Fruchart, Ryo Hanai, Peter B Littlewood, and Vincenzo Vitelli. Non-reciprocal phase transitions. *Nature*, 592(7854):363–369, April 2021.

[207] Pavel Chvykov, Thomas A Berrueta, Akash Vardhan, William Savoie, Alexander Samland, Todd D Murphey, Kurt Wiesenfeld, Daniel I Goldman, and Jeremy L England. Low rattling: A predictive principle for self-organization in active collectives. *Science*, 371(6524):90–95, January 2021.

[208] Arthur T Winfree. *The Geometry of Biological Time*. Springer, New York, NY, 2001.

[209] A T Winfree. Biological rhythms and the behavior of populations of coupled oscillators. *J. Theor. Biol.*, 16(1):15–42, July 1967.

[210] Z Csahok and T Vicsek. Traffic models with disorder. *J. Phys. A Math. Gen.*, 27(16):L591, August 1994.

[211] Tal Danino, Octavio Mondragón-Palomino, Lev Tsimring, and Jeff Hasty. A synchronized quorum of genetic clocks. *Nature*, 463(7279):326–330, January 2010.

[212] Alexandra M Tayar, Eyal Karzbrun, Vincent Noireaux, and Roy H Bar-Ziv. Synchrony and pattern formation of coupled genetic oscillators on a chip of artificial cells. *Proc. Natl. Acad. Sci. U. S. A.*, 114(44):11609–11614, October 2017.

[213] Renato E Mirollo and Steven H Strogatz. Synchronization of Pulse-Coupled biological oscillators. *SIAM J. Appl. Math.*, 50(6):1645–1662, December 1990.

[214] Raphaël Sarfati, Julie C Hayes, Élie Sarfati, and Orit Peleg. Spatio-temporal reconstruction of emergent flash synchronization in firefly swarms via stereoscopic 360-degree cameras. *J. R. Soc. Interface*, 17(170):20200179, September 2020.

[215] Matthew Bennett, Michael F Schatz, Heidi Rockwood, and Kurt Wiesenfeld. Huygens's clocks. *Proceedings of the Royal Society of London. Series A: Mathematical, Physical and Engineering Sciences*, 458(2019):563–579, March 2002.

[216] E Marder and D Bucher. Central pattern generators and the control of rhythmic movements. *Curr. Biol.*, 11(23):R986–96, November 2001.

[217] Nikola Topic and Thorsten Pöschel. Inelastic collapse of perfectly inelastic particles. *Communications Physics*, 2(1):1–5, July 2019.

[218] S McNamara and W R Young. Inelastic collapse in two dimensions. *Phys. Rev. E Stat. Phys. Plasmas Fluids Relat. Interdiscip. Topics*, 50(1):R28–R31, July 1994.

[219] Robert P Behringer and Bulbul Chakraborty. The physics of jamming for granular materials: a review. *Rep. Prog. Phys.*, 82(1):012601, January 2019.

[220] H M Jaeger, S R Nagel, and R P Behringer. Granular solids, liquids, and gases. *Rev. Mod. Phys.*, 1996.

[221] M Reza Shaebani, Adam Wysocki, Roland G Winkler, Gerhard Gompper, and Heiko Rieger. Computational models for active matter. *Nature Reviews Physics*, 2(4):181–199, April 2020.

[222] Pavel Chvykov, Thomas A Berrueta, Akash Vardhan, William Savoie, Alexander Samland, Todd D Murphey, Kurt Wiesenfeld, Daniel I Goldman, and Jeremy L England. Low rattling: A predictive principle for self-organization in active collectives. *Science*, 371(6524):90–95, January 2021.

[223] Jonas Buchli, Ludovic Righetti, and Auke Jan Ijspeert. Engineering entrainment and adaptation in limit cycle systems : From biological inspiration to applications in robotics. *Biol. Cybern.*, 95(6):645–664, December 2006.

[224] L S Tsimring, N F Rulkov, M L Larsen, and M Gabbay. Repulsive synchronization in an array of phase oscillators. *Phys. Rev. Lett.*, 95(1):014101, July 2005.

[225] J E Avron and O Raz. A geometric theory of swimming: Purcell's swimmer and its symmetrized cousin. *New J. Phys.*, 10(6):063016, June 2008.

[226] Ross L Hatton and Howie Choset. Geometric swimming at low and high reynolds numbers. *IEEE Trans. Rob.*, 29(3):615–624, June 2013.

[227] Florian Dörfler and Francesco Bullo. On the critical coupling for kuramoto oscillators. *SIAM J. Appl. Dyn. Syst.*, 10(3):1070–1099, January 2011.

[228] Igor S Aranson and Lev S Tsimring. Pattern formation of microtubules and motors: inelastic interaction of polar rods. *Phys. Rev. E Stat. Nonlin. Soft Matter Phys.*, 71(5 Pt 1):050901, May 2005.

[229] Troy Shinbrot. Competition between randomizing impacts and inelastic collisions in granular pattern formation. *Nature*, 389(6651):574–576, October 1997.

[230] D Goldman, M D Shattuck, C Bizon, W D McCormick, J B Swift, and Harry L Swinney. Absence of inelastic collapse in a realistic three ball model. *Phys. Rev. E*, 57(4):4831–4833, April 1998.

[231] D Grossman, I S Aranson, and E Ben Jacob. Emergence of agent swarm migration and vortex formation through inelastic collisions. *New J. Phys.*, 10, February 2008.

[232] F Mondada, L M Gambardella, D Floreano, S Nolfi, J . Deneuborg, and M Dorigo. The cooperation of swarm-bots: physical interactions in collective robotics. *IEEE Robot. Autom. Mag.*, 12(2):21–28, June 2005.

[233] Markus P Nemitz, Edwin Olson, and Adam A Stokes. HoverBots: Embracing and detecting collisions using robots designed for manufacturability. In *ICRA 2018 Workshop: Swarms: From Biology to Robotics and Back*, May 2018.

[234] S Mayya, P Pierpaoli, G Nair, and M Egerstedt. Localization in densely packed swarms using interrobot collisions as a sensing modality. *IEEE Trans. Rob.*, 35(1):21–34, February 2019.

[235] Siddharth Mayya, Pietro Pierpaoli, Girish N Nair, and Magnus Egerstedt. Collisions as information sources in densely packed Multi-Robot systems under Mean-Field approximations. In *Robotics: Science and Systems*, volume 13, 2017.

[236] Siddharth Mayya, Sean Wilson, and Magnus Egerstedt. Closed-loop task allocation in robot swarms using inter-robot encounters. *Swarm Intelligence*, 13(2):115–143, June 2019.

[237] S Mayya, G Notomista, D Shell, S Hutchinson, and M Egerstedt. Non-Uniform robot densities in vibration driven swarms using phase separation theory. In *2019 IEEE/RSJ International Conference on Intelligent Robots and Systems (IROS)*, pages 4106–4112, November 2019.

[238] Thomas Schmickl, Ronald Thenius, Christoph Moeslinger, Gerald Radspieler, Serge Kernbach, Marc Szymanski, and Karl Crailsheim. Get in touch: cooperative decision making based on robot-to-robot collisions. *Auton. Agent. Multi. Agent. Syst.*, 18(1):133–155, February 2009.

[239] Christian Scholz, Michael Engel, and Thorsten Pöschel. Rotating robots move collectively and self-organize. *Nat. Commun.*, 9(1):931, March 2018.

[240] M A Karimi, V Alizadehyazdi, B Busque, H M Jaeger, and M Spenko. A Boundary-Constrained swarm robot with granular jamming. In *2020 3rd IEEE International Conference on Soft Robotics (RoboSoft)*, pages 291–296, May 2020.

[241] Y Mulgaonkar, A Makineni, L Guerrero-Bonilla, and V Kumar. Robust aerial robot swarms without collision avoidance. *IEEE Robotics and Automation Letters*, 3(1):596–603, January 2018.

[242] Zhouyu Lu, Zhichao Liu, Gustavo J Correa, and Konstantinos Karydis. Motion planning for collision-resilient mobile robots in obstacle-cluttered unknown environments with risk reward trade-offs. pages 7064–7070, 2020.

[243] Mark Mote, Magnus Egerstedt, Eric Feron, Andrew Bylard, and Marco Pavone. Collision-Inclusive trajectory optimization for Free-Flying spacecraft. *J. Guid. Control Dyn.*, 43(7):1247–1258, July 2020.

[244] Jiaming Zha and Mark W Mueller. Exploiting collisions for sampling-based multicopter motion planning. pages 7943–7949, 2021.

[245] Kevin P O'Keeffe, Hyunsuk Hong, and Steven H Strogatz. Oscillators that sync and swarm. *Nat. Commun.*, 8(1):1504, November 2017.

[246] Koichiro Uriu, Saúl Ares, Andrew C Oates, and Luis G Morelli. Dynamics of mobile coupled phase oscillators. *Phys. Rev. E*, 87(3):032911, March 2013.

[247] Mattia Frasca, Arturo Buscarino, Alessandro Rizzo, Luigi Fortuna, and Stefano Boccaletti. Synchronization of moving chaotic agents. *Phys. Rev. Lett.*, 100(4):044102, February 2008.